The Scattering of High Frequency Electromagnetic Radiation from Deterministic Targets on the Ocean Surface

By

©Michael Royle

A dissertation submitted to the School of Graduate Studies in partial fulfilment of the requirements for the degree of Doctor of Philosophy.

Faculty of Engineering and Applied Science

Memorial University of Newfoundland

May 2025

St. John's, Newfoundland

Abstract

An analysis of the electromagnetic scattering from deterministic targets embedded in time-varying random rough surfaces is presented. The approach combines and extends previous works addressing high frequency (HF) electromagnetic scattering from the ocean and stationary surface targets separately. The analysis begins with first- and second-order expressions for the normal component of the scattered electric field from a conducting surface that is small in height and slope and described by a time-varying Fourier series. A vertical pulsed-dipole transmitting source is assumed while the observation point of the scattered field remains general. These expressions are modified to introduce a finite, deterministic target with arbitrary motion via a Fourier transform of the surface target's profile. The Fourier integrals in the resulting expressions are evaluated through asymptotic methods.

The analysis produces two bistatic scattered field expressions involving the surface target. These are attributed to (1) first- and second-order scatters solely from the target and (2) a double scatter involving the target and nearby surrounding ocean. The two components are added to existing expressions for the first- and second-order scattered fields from the ocean surface to model the total scattered field from an ocean patch containing a surface target. It is shown that the HF Doppler cross section of the ocean patch and target may be found as the sum of the cross sections obtained in treating each field component independently. The target-only and target-ocean cross sections are formally evaluated, while the ocean-only components are obtained from existing models. The target-only component is shown to agree with existing monostatic, zero-velocity results when appropriate substitutions are made. The target-ocean

cross section represents a new expression not seen in previous work, but its general form is seen to agree with existing bistatic ocean cross section models. Both cross section components involving target scatter contain a motion-related Fourier factor similar to one that arises in ocean cross section models for a radar installed on a floating platform.

The HF Doppler cross sections are simplified for the case of a surface target moving with constant velocity. It is shown that the target-only cross section contains a Dirac delta function with an argument restricting the response to an impulse at the bistatic Doppler frequency shift predicted for uniform linear motion. The ocean-target component also contains a Dirac delta function with an argument containing the constant-velocity bistatic Doppler shift in addition to terms related to ocean dispersion and the change in target location between radar acquisitions. A system model of an HF radar suitable for predicting the received Doppler power spectral density from an ocean patch containing a surface target is presented. The system model is used to predict the received signal strength for a variety of target, environmental, and radar operating parameters. The results of the computations show, that under certain conditions, a constant velocity target whose first-order cross section is masked by ocean clutter may be detected through a secondary scatter from the ocean surface.

The models derived in this work enable the establishment of suitable design specifications and operating parameters when developing new or utilizing existing HF surface wave radar systems for the purposes of monitoring targets on the ocean surface. In addition, the physical interpretation of the scattering process and simple computation provided by the models should prove relevant in developing and testing novel signal processing techniques for both target identification and clutter rejection.

Acknowledgements

The completion of this doctoral dissertation would not have been possible without the support of numerous individuals and institutions. First and foremost, I would like to thank my supervisor, Dr. Eric W. Gill, for his invaluable guidance and constant encouragement. His support included affording me the academic freedom to work independently when needed, while always remaining available to review results and engage in conversations full of insightful observations and thoughtful advice. This balance greatly contributed to both the quality of this work and my growth as an independent researcher. I would also like to thank supervisory committee members Dr. Reza Shahidi and Dr. Pradeep Bobby for their valuable perspectives in reviewing this work. To the past and present members of the remote sensing group, I am grateful for the many opportunities to present and discuss this research throughout all its stages.

This work was financially supported by the Natural Sciences and Engineering Research Council of Canada (NSERC) and Memorial University's School of Graduate Studies. I would also like to express my gratitude to C-CORE for granting a leave of absence and a place to study.

To my friends and co-workers I am grateful for the support, social engagement, and for keeping me active. Sharing in positive, enthusiastic conversations and activities outside my research helped maintain the energy and motivation to see this work through.

Finally, I would like to acknowledge the incredible contributions of my family. Completing a doctoral degree while raising newborn twins —now toddlers —has re-

quired significant time and energy from many sources including parents, siblings, and in-laws. I am especially thankful for the unwavering support, patience, and encouragement of my wife, Jess, which were truly instrumental in the completion of this work.

Contents

List of Acronyms

EEZ	Exclusive Economic Zone
FDTD	Finite Difference Time Domain
FEM	Finite Element Method
FFT	Fast Fourier Transform
HF	High Frequency
HFSWR	High Frequency Surface Wave Radar
ITU	International Telecommunication Union
MoM	Method of Moments
PSD	Power Spectral Density
NSD	Noise Spectral Density
NEC	Numerical Electromagnetics Code
RCS	Radar Cross Section

List of Figures

Table of Symbols

A list of important symbols used in this work is provided here with the location of each symbol's first reference included in parenthesis. It is noted that this list is not exhaustive and there are a number of parameters that are repeated with slight variations through an analysis. In these cases, the original symbol is included in this list and the definitions of its variations may be understood from context.

σ : Radar Cross Section (p. 7).

f: Radar operating frequency in megahertz (p. 7).

D : Displacement of vessel (p. 7).

P_r : Power received by radar that has been scattered from a target with RCS, σ° (p. 7).

P_t : Transmitting power of radar (p. 7).

G_t : The transmit antenna gain (p. 7).

R : The range to the target (p. 7).

A_r : The effective aperture of the receiving antenna (p. 7).

$D(\ )$: Doppler spectrum expression used by Anderson based on Barrick's work (p. 11).

$\vec{k}_{inc}, \vec{k}_{scat}$: Incident and scattered electromagnetic wave vectors (p. 11).

ω_d : Angular Doppler frequency (p. 11).

$S(\vec{k})$: Directional ocean wave spectrum (p. 11).

F_1, F_2 : Doppler spectrum integral kernels (p. 11).

$\vec{k}_1, \vec{k}_2$: Ocean surface wave vectors (p. 11).

$z = \xi(x, y)$: Two-dimensionally rough surface (p. 13).

$h(\ )$: Heaviside function (p. 13).

$h_R(\ )$: Generalized Heaviside function introduced by Walsh and Gill to describe a space comprised of two media (p. 13).

σ : Electrical conductivity (p. 13).

σ_1 : Conductivity below the rough surface (p. 13).

ϵ_0, ϵ_1 : Electrical permittivity above and below the rough surface, respectively (p. 13).

ω : Angular frequency of electric field (p. 13).

∇ : $\hat{x}\frac{\partial}{\partial x} + \hat{y}\frac{\partial}{\partial y} + \hat{z}\frac{\partial}{\partial z}$ where the $\hat{x}$, $\hat{y}$, and $\hat{z}$, are the unit vectors in Cartesian co-ordinates (p. 13).

$\vec{E}$: Electric field vector (p. 13).

j : $\sqrt{-1}$ (p. 13).

$\vec{B}$: Magnetic flux density (p. 13).

$\vec{H}$: Magnetic field (p. 13).

$\vec{D}$: Electric flux density (p. 13).

$\vec{J}_c$: Conduction Current (p. 13).

$\vec{J}_s$: Source current (p. 13).

ρ_v : Charge density (p. 13).

k : Electromagnetic wavenumber (p. 14).

η_r : Refractive index of the lower medium (p. 14).

T_{sE} : Electrical source operator (p. 14).

E^+, E^- : Electric field evaluated just above (+) or below (-) the rough surface (pp. 14-15).

$\overset{xyz}{*}$: three-dimensional convolution symbol (p. 15).

G_0, G_1 : Electromagnetic Green's functions in free space and the lower medium, respectively (pp. 15-16).

E_{0n}^+ : Normal component of electric field evaluated just above a rough surface with small height (p. 17).

$\mathcal{T}_1, \mathcal{T}_2$: Electric field operators (p. 17).

E^s : The field propagated by the source without scatter from the surface (p. 17).

$\vec{n}$: Upward pointing normal from the rough surface (p. 17).

$\vec{\nabla}_{xy}$: $\hat{x}\frac{\partial}{\partial x} + \hat{y}\frac{\partial}{\partial y}$ (p. 17).

$F(\rho)$: Sommerfeld attenuation function with $\rho = \sqrt{x^2 + y^2}$ (p. 17).

$\mathcal{F}_{xy}, \mathcal{F}_{xy}^{-1}$: Two-dimensional spatial Fourier transform and its inverse (p. 17).

K_x, K_y : Transform variables for the two-dimensional spatial Fourier transform. Form the surface wave vector: $\vec{K} = K_x\hat{x} + K_y\hat{y}$ (p. 17).

u : $\sqrt{K_x^2 + K_y^2 - k^2}$ (p. 17).

$\vec{E}^{z-}(K_x, K_y)$: Two-dimensional Fourier transform of the source field in free-space evaluated for $z = z^- < \xi(x, y)$ (p. 17).

C_0 : Dipole constant (p. 23).

I : Dipole source current (p. 23).

Δl : Source dipole length(p. 23).

$\xi(x, y, t)$: Height of time varying rough surface at position (x, y) and time t (p. 24).

$P_{\vec{K}_{\vec{K},\omega}}$: Fourier series coefficient associated with the surface wave vector, $\vec{K}$, and angular frequency, ω (p. 24).

$< >$: Ensemble average (p. 24).

$S(\vec{K}, \omega)$: Power spectral density of the ocean surface (p. 24).

${}_1P_{\vec{K},\omega}, {}_2P_{\vec{K},\omega}$: First- and second-order ocean surface Fourier coefficients (p. 24).

${}_H\Gamma$: Hydrodynamic coupling coefficient (p. 25).

g : Acceleration due to gravity (p. 25).

$(E_{0n}^+)_1$: First order component of E_{0n}^+ with higher orders indicated in the subscript (p. 26).

ρ_s : $\frac{\rho_1+\rho_2}{2}$ as defined on Figure 1.2 (pp. 26-27).

t_0 : Time delay between a single transmission of a radar signal and its reception after being scattered from a rough surface (p. 27).

ω_0 : Operating frequency of radar in radians (p. 27).

Sa[ ] : Sampling function (p. 27).

τ_0 : Pulse width (p. 27).

c : Speed of light in free space (p. 27).

$\Delta\rho_s$: Bistatic patch width, $\frac{c\tau_0}{2}$ (p. 27).

ϕ : Bistatic angle (p. 27).

$\mathcal{R}(\tau)$: Autocorrelation function (p. 28)

η_0 : Intrinsic impedance of free space (p. 28)

σ_{11} : First-order ocean radar cross section (p. 28)

$\left(E_{0n}^{+}\right)_{2ep}$: Second-order electromagnetic patch scattered field (p. 32).

${}_E\Gamma_P(\vec{K}_1, \vec{K}_2)$: Electromagnetic coupling coefficient (p. 32).

Δ : Surface impedance of the ocean (p. 32).

$\left(E_{0n}^{+}\right)_{12}$: Electric field corresponding to a signal electromagnetic scatter from a second-order ocean wave (pp. 33).

Γ_P : Patch scatter coupling coefficient (p. 34).

σ_{2P} : Second-order RCS component for patch scatter (p. 34).

${}_S\Gamma_P$: Symmetric Patch scatter coupling coefficient (pp. 34).

ξ_t : Surface target height profile (p. 351).

Ξ_t : Two-dimensional Fourier transform of surface target height profile (p. 35).

Ξ_{t0} : Origin-shifted two-dimensional Fourier transform of surface target height profile (p. 36).

$\vec{\rho}_t$: Central location of the surface target. Used as the origin for Ξ_{t0} (p. 36).

$\mathcal{P}$: Factor of the monostatic target RCS derived by Walsh and Gill that depends on the Fourier transform of the target height profile, Ξ_t (pp. 37-38).

$\left(E_{0n}^{+}\right)_{1t}(t_0, t)$: First-order scattered field from moving surface target (p. 44).

$\vec{\rho}_{0t}$: Constant component of target location (p. 45)

$\vec{\rho}\,'_{0t}$: $\vec{\rho}_{0t}$ - $\frac{\vec{\rho}}{2}$ with magnitude, ρ_t, and angle, $\theta_{\theta_{\vec{\rho}_{0t}}}$ (p. 45).

$\vec{\delta\rho}_t(t)$: Time-varying component of target location (p. 45).

I_j : I is used to represent intermediate integrals throughout this work with various subscripts (p. 45).

$\delta(\ )$: Dirac delta function (p. 47).

ρ_{0c} : Radius of curvature (p. 48).

$\hat{N}$: Unit vector of the outward pointing normal (p. 48).

$\left(E_{0n}^{+}\right)_{2t}(t_0, t)$: Second-order scattered field from moving surface target (p. 49))

${}_{SE}\Gamma_P$: Symmetrized form of the electromagnetic coupling coefficient for patch scatter (p. 52).

$\mathcal{P}_0$: Function of the target Fourier transform and surface wave numbers that arises in the target RCS expression (p. 53).

$\left(E_{0n}^{+}\right)_{2to}(t_0, t)$: Second-order target-ocean patch scattered field (p. 55).

$\left(E_{0n}^{+}\right)_{2ot}(t_0, t)$: Second-order ocean-target patch scattered field (p. 58).

$\mathcal{P}_d$: Doppler power spectral density of an electric field (p. 66).

M_t : Motion related function for target-only scatter (p. 68).

M_{to} : Motion related function for target-ocean scatter (p. 70).

σ_t : Radar cross section component from target scatter only (p. 71).

σ_{to} : Radar cross section component from target-ocean scatter (p. 74).

$\vec{v}$: Constant surface target velocity (p. 78).

ξ_{t0} : Origin shifted surface target height model (p. 82).

$\vec{K}_l, \vec{K}_w$: Surface wave vectors corresponding to the length and width of ξ_{t0} (p. 82).

w : Window function used in defining ξ_{t0} (p. 82).

U : Wind speed (p. 86).

$\overline{\theta}$: Overall mean direction of wind (p. 86).

A_p : Radar cell patch area (p. 88).

θ_{BW} : Receiving antenna array beamwidth (p. 88).

G_r : Receiving antenna gain (p. 89).

T_L : Pulse repetition interval (p. 89).

$\mathcal{P}_N$: Noise power spectral density (p. 90).

F_{am} : Median external noise figure (p. 90).

θ_{3dB} : Half-power beamwidth of the receiving antenna (p. 91).

d : Receiving antenna array element spacing (p. 91).

Y : Equal to $\sqrt{K}$. Transformed integration variable (p. 93).

$G(Y)$: Argument of the Dirac delta function in the ocean-target cross section expressed as a function of the transform variable Y (p. 93).

Chapter 1

Introduction

1.1 Motivation

With the ever-growing importance of Canada's ocean economy comes a need to monitor marine vessels and other hard targets in real-time. This is of particular concern in the Exclusive Economic Zone (EEZ), a region established in 1982 that extends 200 nautical miles (nmi) beyond a nation's coast where it maintains sovereign rights over renewable and non-renewable resources [2]. The ability to locate, track, and uniquely identify surface targets in this region provides a significant benefit to a wide variety of Canadian interests. High Frequency (HF) radars are able to provide these capabilities, and unlike alternative sensors, can provide persistent long-range coverage. Observations from HF radars are valuable to commercial industries such as shipping, fisheries, and petroleum extraction, as well as security and defence for military and search and rescue operations.

HF radars operate in the 3-30 MHz band and exhibit a number of unique characteristics when compared to microwave radars due to their longer wavelengths and limited bandwidths. This includes the ability to utilize both skywave and surface wave modes of propagation to monitor ocean targets beyond the line-of-sight. Skywave radars exploit the reflection of HF radio waves from the Ionosphere to achieve detection ranges beyond the horizon. This work addresses the surface wave mode, where the radio wave is guided along the conducting ocean surface. Using this mode, detection ranges exceeding 220 nmi [3] have been achieved at the lower end of the HF band. The electromagnetic wavelength of HF radiation ranges from 10 to 100 m and is of the same order of magnitude as the dimensions of many practical targets such as marine vessels, icebergs, and aircraft. For these targets, HF radars are not well suited for observing detailed characteristics, but in many cases the scattered signals are proportional to the overall size and orientation of a target. When considering the size of a radar cell imposed by the radar's range resolution and receiving antenna's beamwidth, HF radars face considerable constraints due to practical limits of available bandwidths and antenna array lengths. As a result, radar cell resolutions are often limited to areas of hundreds of square meters to a few square kilometers.

Perhaps the most significant limitation to the monitoring of surface targets is the return from the ocean surface itself. For frequencies in the HF band, the electromagnetic wavelengths correspond to those of gravity waves, where most of the ocean's energy is carried. Furthermore, as the ocean is itself a moving target, the returning radar signal is Doppler-shifted. The radar returns from the surface can be significant, occluding targets of interest in both the range and Doppler domains. This phenomenon has been studied significantly in the past, with particular efforts focused on developing radar cross section (RCS) models for the ocean surface. In the context of HF radar, an ocean RCS is the ratio of the signal power reflected from the ocean relative to the transmitted signal power. It is frequently defined as a function of Doppler frequency and specified as a normalized per-unit-area quantity. The use of RCS models in developing methods to estimate ocean conditions from HF radar measurements has resulted in HF Surface Wave Radars (HFSWR) being primarily employed as oceanographic sensors, with target detection often treated as a secondary function.

Even with the advantages provided by the long-range and real-time updates of HF radars for observing targets, relatively little effort has been made in the past to study electromagnetic scattering from targets on the ocean surface when compared to the scattering from the ocean itself. Early works addressing scattering from surface targets favoured experimental measurements [4]. With the introduction of the EEZ, interest in monitoring ships increased along with a corresponding increase in model development. In one study, Pondsford [3] proposes extrapolating an empirical estimate originally developed by Skolnik [5] with marine radars to obtain the RCSs of ships in the HF band as a function of their displacement. In more recent work, numerical computer modelling has been used to simulate the RCSs of surface targets. This method can be expensive in time and computing resources and typically neglects the time-varying nature of the ocean surface [6–8].

A potentially significant contribution to the Doppler signature of a surface target is the result of a second-order effect where radiation scattered by the target is scattered a second time from the ocean surface (or vice-versa) before reaching a radar receiver. When the radiation from an HF radar is scattered by two moving targets, the re-radiated field will experience two or more Doppler shifts depending on the relative motion. In addition, the directional nature of both dominant surface waves and targets may lead to significant returns for specific geometries and radar look angles. With knowledge of the current ocean state able to be derived from the radar returns, it may be possible to determine unique information about surface targets in this second-order return. By developing mathematical expressions that model this scenario, the physical parameters that contribute to it can be better understood. These expressions may also aid in designing new or employing existing HF radar systems for monitoring surface targets. Furthermore, mathematical models can aid in the development of signal processing techniques, including clutter suppression and target tracking.

The overarching objective of this work is to analyze bistatic scattering from deterministic targets in motion on a rough, time-varying surface. In applying the work to HF radars monitoring the ocean surface, commonly used approximations will be employed to derive radar cross section models that may be easily computed. These cross sections can be incorporated in a full radar system model to predict the received signal for a given set of target and environmental parameters. This allows for a better understanding of existing systems in addition to providing insight into improving the target detection capabilities of future HF radars. It is primarily intended that the results aid in the future development of techniques for detecting, tracking, and classifying surface targets in the challenging ocean environment. The results may also find a secondary application in enhancing measurements from radars deployed for oceanographic remote sensing. In particular, an understanding of the scattering from both the target and its surroundings may enable the ability to separate the target and sea-scatter contributions. This would permit an estimate of the sea-scatter signature without the target present and a determination of the undisturbed ocean surface conditions.

1.2 Literature Review

The proposed research spans two mature topics in the field of electromagnetics, namely scattering from deterministic surface targets and the scattering from conducting, time-varying random rough surfaces. As this research aims to study the interaction between targets and rough surfaces, the following literature review will focus on electromagnetic scattering modelling methods that have successfully been applied to each topic. For a thorough introduction to HF Radar in the ocean environment, the reader is referred to Chapter 1 of [1], while a detailed review specific to rough surface scattering may be found in Gill's doctoral thesis [9].

The earliest published works studying HF radar scattering report experimental results from targets and rough surfaces. These include Crombie's well-known work recognizing the strong peaks in HF radar returns from the ocean as a form of Bragg scatter [10]. In the context of HF radar, Bragg scatter refers to significant reflected signals from ocean waves having a wavelength of half that of the central frequency of the transmitting waveform. Two notable approaches to approximate analytical RCS models of the ocean as applied to HF radars have been adopted by researchers, both of which have been adapted for surface target modelling. Barrick developed first- [11] and second-order [12] models based on the perturbation method used by Rice [13]. This method has been adapted by Anderson to model HF signatures of ship wakes, including their interaction with the ocean [14]. In the 1980's, Walsh and colleagues developed a technique using generalized functions to model propagation and scatter over conducting media [15] that is small in height and slope. This method was used by Srivastava to develop analytical approximations to the monostatic RCSs of an ocean patch [16] and extended by Gill to the bistatic case [17, 18]. The method was also used to model scattering from discontinuities as applied to ice-hazards including sea-ice and icebergs [19, 20]. Additionally, scattering from deterministic surface targets was treated by Walsh and Gill but only for the monostatic case [21].

Any contemporary study of electromagnetic scattering should consider the availability of numerical simulation software, such as Ansys HFSS [22] or CST Studio Suite [23]. With widespread access to significant computing power and commercial software able to model complex geometries, accurate scattering models can be implemented to produce detailed RCSs. Numerous methods exist; however, the general principle is the same. The target and its surroundings are discretized, allowing Maxwell's equations to be enforced on a point-by-point basis. The result is a system of equations that can be solved for the electric or magnetic fields or currents in a defined region for a given excitation or incident wave. The Numerical Electromagnetics Code (NEC) [24] is an implementation of the Method of Moments (MoM) that has frequently been used to model ships, including superstructures, as wire grids.

The following sections provide background for each of the methods introduced above. Significant details of the Walsh method and its applications are provided as they form the foundation of the proposed research.

1.2.1 Experimental Measurements

Experimental measurements at HF may be performed to characterize a scattering target for which an analytical model does not already exist or to validate a model that has already been developed based on theory. Additionally, more functional experiments may be performed to demonstrate an implemented system's capabilities. The first reported cross sections of marine vessels were determined by measurements using calibrated radars at X, S, and L bands [5]. The result is the empirical expression for the RCS, σ,

$$\sigma = 52 f^{1/2} D^{3/2} \tag{1.1}$$

where f is the operating frequency of the radar in megahertz and D is the displacement of the vessel in kilotons. This expression has been used by Pondsford for HF radar RCS estimates [3]. A subsequent experiment performed by the U.S. Naval Research Laboratory measured the RCS of small boats using a calibrated HF radar [4]. That work determined that the RCS of small boats is dominated by the grounded vertical superstructure acting as a monopole scatterer. A later experiment was performed by Khan et al, demonstrating the ability of an HF surface wave radar to detect ships, icebergs, and low flying aircraft [25].

In understanding how the RCS of targets may be determined by measurement, it is helpful to write the radar equation as

$$P_r = \frac{P_t G_t}{4\pi R^2} \frac{\sigma A_r}{4\pi R^2} \tag{1.2}$$

where the various quantities are

P_r: The power received by the radar

P_t: The power transmitted by the radar

G_t: The transmit antenna gain

R: The range to the target

A_r: The effective aperture of the receiving antenna .

In a calibrated radar used for RCS measurements, with the exception of the RCS itself, all the quantities on the right hand side are known. Thus the target's RCS may be determined from the received power.

Following Crombie's deduction [10] that the sea-echo observed by HF radars was a form of Bragg scattering, much of the experimental work focused on validating RCS models based on newly-developed theory. Additionally, rather than validate the absolute RCS predicted by the models, these experiments tended to use alternative sensors, e.g. wave buoys or current sensors, to ground truth the models' abilities to predict radar returns for specific ocean conditions. The ultimate objective of these experiments is to produce a means to invert the models, allowing ocean conditions to be determined from HF radar measurements [26].

1.2.2 Numerical Modelling

Perhaps the most widely used method of modelling electromagnetic scattering currently is through commercially-available software. A number of packages are available that use different numerical methods to determine the total electric field in a simulated environment for a specific excitation. Commonly-used methods include the Finite Element (FEM) and Finite-Difference Time-Domain (FDTD) methods, and the Method of Moments (MoM). FEM and FDTD discretize the entire simulated environment, generating a large system of linear equations where the unknowns are the electromagnetic field values in each discrete unit. In its simplest form, the MoM discretizes only the boundaries between conducting surfaces and surrounding free space. In this case, the unknowns are the electric and magnetic surface currents on the boundaries. In many cases, this results in a smaller system of equations to solve compared to FEM or FDTD.

Examples of the use of the Method of Moments in modelling the scattering from hard targets at HF are prevalent in the literature. It has been used in determining the RCS of ships [6–8] as well as studying the composite scattering from multiple ships and structures in close proximity [27]. In [28], hull shaping for HF radar cross section reduction was studied for skywave geometries using the MoM. In one example relevant to the application detailed in Chapter 4 of this work, a tumblehome hull, where the hull narrows as the height above ocean surface increases, was modelled. This shape has been used in some modern warships such as the Swedish *Visby*-class corvette [29] and the American *Zumwalt*-class Destroyer [30] to reduce microwave radar signatures; however it was noted that the RCS reduction was limited at HF. This can be attributed to the decametric wavelength of HF radiation having the same order of magnitude as the overall ship dimensions. While not as prevalent in studying HF radar sea-echo, one study by Demarty *et al.* [31] evaluated backscatter from a time-varying surface using the MoM. In this case, the surface was required to be simulated for a number of time steps to form the Doppler spectrum. Additionally, only a patch of the surface was modelled, thus potential scattering from locations remote from the patch would not be observed [15, 16].

1.2.3 Perturbation Theory

Perturbation Theory refers to methods used for finding analytical approximations to solutions of a problem using the exact solution of a simpler, related problem as a starting point. First presented by Lord Rayleigh [32] in the context of acoustical scattering from rough walls, it was adapted by Rice in studying electromagnetic scattering from a rough surface [13] that is small in height and slope. Using the method developed by Rice, Barrick derived expressions for the effective impedance of the surface to study the propagation of HF and VHF electromagnetic radiation at grazing incidence [33]. Subsequent work produced first- and second-order cross sections of the ocean surface by introducing a time-variation to the rough surface [11, 12]. A more general review of perturbation theory, as applied to the scattering from rough surfaces, is provided by Gill [9].

While not directly applied to scattering from hard targets, Barrick's Doppler spectral models have been adapted by Anderson to study first- and second-order scattering from the wakes of both ships and submarines [14]. That work also considered the composite scatter from both the ship wake and the nearby surrounding ocean.

1.2.3.1 Radar Cross Sections of an Ocean Patch

Following the work of Rice [13], Barrick [11] expressed the random surface height as a Fourier series but introduced time as an independent variable. The scattered electric fields were also expanded as a series of plane waves. The coefficients of the scattered electric field were then found by enforcing a Leontovich (or impedance boundary) condition on the surface and assuming the surface is small in both slope and height. The average scattered power was then determined from the Fourier transform of the autocorrelation of the scattered electric field. By introducing an ocean spectrum model, expressions for the first- and second-order RCS of a patch were obtained [11, 12, 34].

1.2.4 Ship Wake Radar Signatures

The possibility of monitoring small ships using HF radars to detect their wakes had long been recognized, but little analytical work had been completed until Anderson in 2019 [14]. Anderson recognized that the Doppler spectrum, $D(\vec{k}_{scat}, \vec{k}_{inc}; \omega_d)$, predicted by Barrick's work could be expressed in the form

$$D(\vec{k}_{scat}, \vec{k}_{inc}, \omega_d) = \int F_1(\vec{k}_{scat}, \vec{k}_{inc}, \vec{k_1}) S(\vec{k_1}) d\vec{k_1} + \int_{\vec{k_2}} \int_{\vec{k_1}} F_2(\vec{k}_{scat}, \vec{k}_{inc}, \vec{k_1}, \vec{k_2}) S(\vec{k_1}) S(\vec{k_2}) d\vec{k_1} d\vec{k_2} \quad (1.3)$$

where ω_d is the Doppler frequency, F_1, F_2 are integration kernels for first- and second-order scatter, $\vec{k}_{scat}, \vec{k}_{inc}$, are the scattered and incident electromagnetic wave vectors, and $S(\vec{k})$ is the directional wave spectrum. By expressing the total wave spectrum as the sum

$$S(\vec{k}) = S(\vec{k})_{wave} + S(\vec{k})_{wake} \quad (1.4)$$

and substituting it into the equation for the Doppler spectrum, an expression containing six terms results. This comprises two first-order terms corresponding to Bragg scattering and direct scattering from the wake, and four second-order terms containing all possible combinations of wave-wave, wave-wake, wake-wave, and wake-wake scattering. Anderson restricted the wake model to the ship's Kelvin wake, the V-shaped wake pattern first explained by Lord Kelvin [35] that trails a ship travelling with uniform linear motion. The Doppler signatures of different ships are compared with each other as well as with the signature of the ambient ocean. The analysis suggests that the Doppler signature of wake scattering may be detectable in Doppler regions away from the Bragg frequency. One key challenge noted by Anderson was efficiently computing the wake spectra to be able to use these models in real time applications.

1.2.5 Walsh's Method

In 1980, Walsh [15] proposed a technique for the analysis of electromagnetic scattering from rough surfaces using generalized functions. The method has been adapted for periodic surfaces [36] and discontinuities in mixed paths [37], and generalized for two-body scattering [38]. Further refinements to the method produced RCS models for conducting surface targets [21, 39]. The presentation of Walsh's method in this section includes refinements developed in a subsequent technical report written in 1990 [39]. As neither of the technical reports that develop the technique are publicly accessible, references in the following sections will be limited to equivalent work that subsequently appeared in academic journals. It should also be noted that the following sections have similarities inherent to the doctoral dissertations of both Gill [9] and Silva [40]. This can be expected as the proposed work shares a common starting point with the work of both authors.

The infinite two-dimensional surface depicted in Figure 1.1 forms a boundary between two media. Walsh and Gill [21] characterize the whole space using

$$h_R(x, y, z) = 1 - h[z - \xi((x, y)] \quad , \tag{1.5}$$

where $\xi(x, y)$ is the height of the surface, and h is the Heaviside function that is defined as

$$h(z) = \begin{cases} 1, & z \geq 0 \\ 0, & z < 0 \end{cases} \quad . \tag{1.6}$$

The medium above the surface is assumed to be free space with permittivity, permeability, and conductivity of ϵ_0, μ_0, and 0 respectively. For the medium below the surface, these values are ϵ_1, μ_0, and σ_1. Under these assumptions, the electrical properties of the entire space can be expressed using Equation (1.5) as

$$\sigma = h_R \sigma_1 \tag{1.7}$$

$$\epsilon = \epsilon_1 h_R + \epsilon_0 (1 - h_R) \quad . \tag{1.8}$$

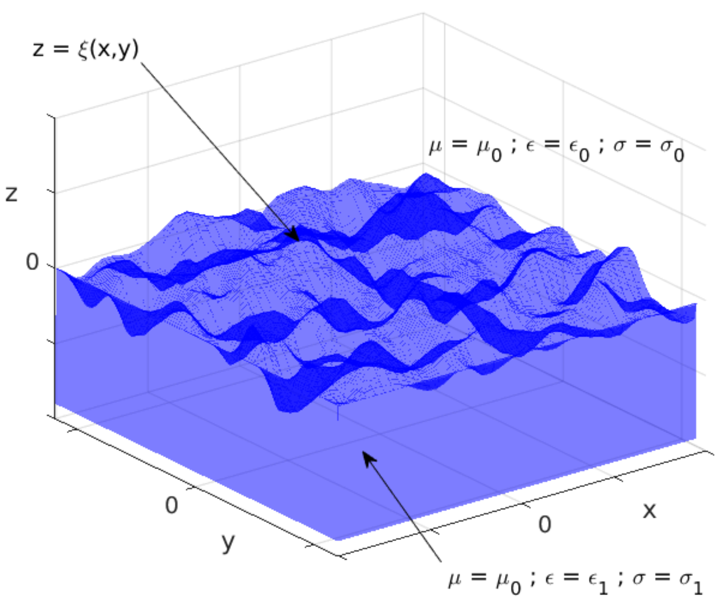

Figure 1.1: Rough surface from Chapter 1 of *Huang and Gill* [1].

Recalling Maxwell's equations in point form for $e^{j\omega t}$ time (t) dependence (i.e. for time-harmonic fields) with angular frequency, ω,

$$\nabla \times \vec{E} = -j\omega \vec{B} \tag{1.9}$$

$$\nabla \times \vec{H} = -j\omega \vec{D} + \vec{J}_c + \vec{J}_s \tag{1.10}$$

$$\nabla \cdot \vec{E} = \rho_v \tag{1.11}$$

$$\nabla \cdot \vec{B} = 0 \tag{1.12}$$

where $\vec{E}$ and $\vec{H}$ are the electric field and magnetic fields, $\vec{J}_c$ and $\vec{J}_s$ are the conduction and source currents, and ρ_v is the charge density. Using Equations (1.7) and (1.8), the constitutive relations become

$$\vec{D} = \left[\epsilon_1 h_R + \epsilon_0 (1 - h_R)\right] \vec{E} \tag{1.13}$$

$$\vec{B} = \mu_0 \vec{H} \tag{1.14}$$

$$\vec{J}_c = \sigma_1 h_R \vec{E} \quad . \tag{1.15}$$

Using the work of Walsh and Donnelly [38], the electric field for the entire space is found to satisfy

$$\nabla^2 \vec{E} + \left[\eta_r h_R + (1 - h_R)\right] k^2 \vec{E} = \frac{\eta_r^2 - 1}{\eta_r^2} \nabla \left[\vec{E}^+ \cdot \nabla h_R\right] - T_{sE}(\vec{J}_s) \tag{1.16}$$

where $k^2 = \omega^2 \mu_0 \epsilon_0$, η_r is the refractive index of the lower medium, the $\vec{E}^+$ is the electric field immediately above the boundary, and T_{sE} is an electrical source operator defined as

$$T_{sE}(\vec{J}_s) = \frac{1}{j\omega\epsilon_0} \left[\nabla(\nabla \cdot \vec{J}_s) + k^2 \vec{J}_s\right] \quad . \tag{1.17}$$

The electric field is then decomposed as

$$\vec{E} = (1 - h_R)\vec{E} + h_R\vec{E} \tag{1.18}$$

and its Laplacian is evaluated. The result is two differential equations describing the electric field in the media above and below the surface as well as an equation containing the boundary conditions. The field equations are converted to integral equations though convolution with the electromagnetic Green's function for the respective media. The resulting integral equations, presented in [21], dictating the electric field are written as

$$(1 - h_R)\vec{E} = \vec{E}_s + \left\{\nabla \cdot \left[\vec{E}^{+}\nabla h_R\right] + \left(\nabla\vec{E}\right)^{+} \cdot \nabla h_R\right\} \overset{xyz}{*} G_0 \tag{1.19}$$

$$h_R\vec{E} = -\left\{\nabla \cdot \left[\vec{E}^{-}\nabla h_R\right] + \left(\nabla\vec{E}\right)^{-} \cdot \nabla h_R\right\} \overset{xyz}{*} G_1 \tag{1.20}$$

where $\vec{E}_s \equiv T_{sE}(\vec{J}_s) \overset{xyz}{*} G_0$, and the boundary conditions naturally arise through the Laplacian evaluation as

$$\left[(\nabla\mathbf{E})^{+} - (\nabla\mathbf{E})^{-}\right] \cdot \nabla h_R + \nabla \cdot \left[(\mathbf{E}^{+} - \mathbf{E}^{-})\nabla h_R\right] = \frac{\eta_r^2 - 1}{\eta_r^2}\nabla(\mathbf{E}^{+}\nabla h_R) \quad . \tag{1.21}$$

The superscripts indicate whether the terms are evaluated just above (positive) or below (negative) the interface, and the $\overset{xyz}{*}$ operator indicates a three-dimensional convolution with the electromagnetic Green's functions, G_0 and G_1, for the different media which are defined as

$$G_0 = \frac{e^{-jkr}}{4\pi r} \quad , \quad G_1 = \frac{e^{-jk\eta_r r}}{4\pi r} \tag{1.22}$$

with $r = \sqrt{x^2 + y^2 + z^2}$. From the form of Equations (1.19) and (1.20), Walsh notes that contributions to a field in a region must produce zero field outside that region,

$$h_R \left\{ \vec{E}_s + \left[\nabla \cdot \left[\vec{E}^+ \nabla h_R \right] + \left(\nabla \vec{E} \right)^+ \cdot \nabla h_R \right] \overset{xyz}{*} G_0 \right\} = 0 \tag{1.23}$$

$$(1 - h_R) \left\{ \left[\nabla \cdot \left[\vec{E}^- \nabla h_R \right] + \left(\nabla \vec{E} \right)^- \cdot \nabla h_R \right] \overset{xyz}{*} G_1 \right\} = 0 \quad . \tag{1.24}$$

Equations (1.19) and (1.20) show that the scattered field in each region may be determined from the electric field and its derivatives on the boundary inside that region. The objective of Walsh's method is then to find a solution to these values. In the context of an HF radar operating in the surface-wave mode, attention can be limited to the normal component of the electric field just above the surface. This is justified at observation distances far removed from the source and points of scatter as the tangential electric field component decays more rapidly than the normal component. Walsh formally demonstrates this through Fourier analysis assuming the lower medium is a good conductor, and the surface, ξ, is electrically small in height (i.e. $k\xi << 1$). The resulting operator equation for the normal component of the surface electric field, $E_{0_n}^+$, is then given as

$$E_{0n}^+ - \mathcal{T}_1(E_{0n}^+) - \mathcal{T}_2(E_{0n}^+) = E^s \quad , \tag{1.25}$$

with

$$\mathcal{T}_1(E_{0n}^+) = \frac{1}{|\vec{n}|^3} \cdot \left\{ \frac{\nabla\xi}{|\vec{n}|^2} \cdot \nabla_{xy} \left[|\vec{n}|(E_{0n}^+) \right] \overset{xy}{*} F(\rho) \frac{e^{-jk\rho}}{2\pi\rho} \right\} \quad ,$$

$$\mathcal{T}_2(E_{0n}^+) = \frac{\nabla\xi}{|\vec{n}|^3} \cdot \left\{ \frac{\nabla\xi\nabla\xi}{|\vec{n}|^2} \cdot \nabla_{xy} \left[|\vec{n}|(E_{0n}^+) \right] \overset{xy}{*} F(\rho) \frac{e^{-jk\rho}}{2\pi\rho} \right\} \quad ,$$

$$E^s = \frac{\vec{n}}{|\vec{n}|^3} \cdot \left\{ \frac{\vec{n}\vec{n}}{|\vec{n}|^2} \cdot \mathcal{F}_{xy}^{-1} \left[2u\mathcal{F}_{xy} \left(\vec{E}_s^{z^-} \right) e^{-z^- u} \right] \overset{xy}{*} F(\rho) \frac{e^{-jk\rho}}{2\pi\rho} \right\} \quad .$$

In Equation (1.25), ∇_{xy} indicates a gradient operating on only the x- and y- dimensions, $\vec{n}$, is the upward-pointing normal to the surface, $F(\rho)$, is the Sommerfield attenuation function, and $\mathcal{F}_{xy}$ is a two-dimensional Fourier transform with transform variables K_x and K_y. Additionally, the $\overset{xy}{*}$ operator indicates a two-dimensional planar convolution. In the expression for E^s, the $z-$ superscript on the $\vec{E}_s^{z^-}$ term, indicates it should be evaluated on a plane $z- < 0 < \xi(x,y)$ and u is given as

$$u = \sqrt{K_x^2 + K_y^2 - k^2} \quad . \tag{1.26}$$

Equation (1.25) is greatly simplified by assuming $|\vec{\nabla}\xi| \ll 1$, also referred to as the small slope assumption, implying

$$|\vec{n}|^2 = 1 + |\nabla\xi|^2 \approx 1 \quad . \tag{1.27}$$

Under this assumption, Equation (1.25) reduces to

$$E_{0n}^+ - \mathcal{T}_1(E_{0n}^+) = E^s \tag{1.28}$$

or

$$E_{0n}^{+} - \nabla\xi \cdot \nabla_{xy}(E_{0n}^{+}) \overset{xy}{*} F(\rho)\frac{e^{-jk\rho}}{2\pi\rho} = E^{s} \quad , \tag{1.29}$$

when terms with gradients of order higher than one are omitted and $|\vec{n}| \approx 1$.

Obtaining solutions to Equations (1.25) and (1.29) has been the focus of numerous researchers since the introduction of Walsh's method; see for example, [9,16,41–43].

1.3 Analysis Method Selection Rationale

The preceding literature review identified several analysis techniques that have been applied to both HF scattering from the ocean and surface targets. When compared to methods employing analytical approximations, experimental measurements and numerical solutions to Maxwell's equations may be considered more direct, yielding the desired measured or calculated metric for a set of operating conditions. The implementation of these techniques requires significant capital or computational costs, limiting their application to specific use cases. More significantly, expressions derived through analytical approximations can provide physical insight in to the scattering process that is not possible with measurements or numerical simulation. As the primary objective of the research completed in this work is to develop RCS expressions that aid in the design and deployment of HF radar systems, particular attention was directed towards the consideration of the perturbation and Walsh methods.

In evaluating the perturbation and Walsh methods as applied to HF radar scatter, it is important to recognize that both techniques seek to form analytical approximations to Maxwell's equations by employing relevant simplifying assumptions and constraints. In effect, both methods share a common starting point and it should be expected that results obtained from either method for the same set of constraints are consistent. This is demonstrated in the work of Srivastava [16] and Gill [9] when comparing their results with the monostatic [33] and bistatic [34] perturbation analyses performed by Barrick.

A key difference in the use of the perturbation and Walsh methods is how each method employs the simplifying assumptions and the order in which they are applied. In following the work of Rice [13] and expanding the incident and scattered fields as a series of plane waves, Barrick [33] implicitly assumes a continuous wave or infinite duration transmitting waveform. Barrick's subsequent application of the perturbation approach to determine the scattered fields at the boundary immediately and concurrently assumes that the surface is small in slope and height, and that it may be considered a good conductor at the frequency of interest. As noted by Silva [43], this second consideration is fundamental to the use of perturbation theory and prevents the removal of any one of the assumptions.

The Walsh method begins with Maxwell's equations and uses generalized functions to model the region of interest and associated boundaries. Solutions to the scattered field from a rough surface are found through sequential application of simplifying assumptions. As constraints are imposed at different stages of the derivations, it is possible to re-evaluate the analysis to relax some constraints or include additional considerations. This fact has been exploited by numerous researchers as evident by the example applications listed in Section 1.4 and is the primary motivation for its use in this work. While the final form of many of the expressions derived in this work employ the same assumptions used by Barrick [33], the use of the Walsh method provides opportunity to further generalize the results in subsequent research endeavors.

1.4 Applications of Walsh's Method

The easily adaptable nature of using generalized functions to model electromagnetic scattering has led to Walsh's method being employed in a variety of applications. Gill [9], provides a detailed history of the development of first- and and second-order RCS models of the ocean surface, while developing new expressions for bistatic cross sections for a pulsed-dipole transmitting source. More recent work has produced RCS models for radars installed on moving platforms [42,44], ionosphere clutter [41,45,46], and surfaces with electrically large heights [43]. Shahidi, Silva, and Gill have also proposed a number of novel methods using a change-of-variables in the electric field [47] and RCS integrals [48–50] to extract ocean parameters from measured HF radar in both the time- and frequency- domains respectively.

In addition to the fundamental scattering analyses, rough surface RCS models developed using the Walsh method have found use in both industry and the scientific community. Notably, Northern Radar Inc. was established to develop HFSWR systems and ocean remote sensing software based on the results of Walsh' work. The benefits provided by the contributions of Northern Radar in partnership with Memorial University were recognized by the Canadian government resulting in significant funding to further develop the analysis software [51]. More recently, the cross section models for ship-borne radars have been adapted by the scientific community in studying and suppressing ocean returns for various radar configurations with some examples found in [52–54].

While the majority of work employing Walsh's method is directed toward rough surface scattering, there have been some applications to hard target scattering. The earliest work modelled backscatter from sea-ice represented as a discontinuous mixed path, [19, 55]. This work was further developed to model scattering from finite discontinuities, producing RCS models of icebergs [20, 56]. In a separate development, Walsh and Gill [21] presented a solution to Equation (1.29) for scattering to third-order from deterministic targets protruding from a conducting surface. The results were used to approximate the RCS of a sphere and an exponential boss. In the case of a sphere, the estimated RCS was found to be approximately 20% of the accepted value, but the expression was proportional to the fourth power of the sphere's radius as predicted by accepted theory. The discrepancy was attributed to the sphere's profile violating the small-slope assumption.

As the rough surface scattering analysis is the starting point for the deterministic target RCS, the details will be given here. The general process outlined in Gill's doctoral thesis [9] will be followed, with a few modifications for brevity and to include some refinements from more recent works. Subsequently, the process used by Walsh and Gill in developing RCS models for stationary deterministic targets will be detailed. These two analyses form the basis for the research carried out in this work.

1.4.1 Radar Cross Section Models of an Ocean 'Patch'

In the previous works deriving RCS models of the ocean surface from solutions to (1.29), a formulaic method has been established. It begins with solving (1.29) using the Neumann series method. The surface is then defined using a Fourier series before the electric field components are simplified using asymptotic approximations. A source waveform is then specified and time-domain field expressions are found using a temporal inverse Fourier transform. After introducing a time-variation to the surface definition, the power spectral density (PSD) of a received radar signal for each component is found as the Fourier transform of their autocorrelation functions. Normalized per-unit-area RCSs are found by comparing the PSD with the standard radar equation. An ocean patch may be defined from the cell resulting from the range and angular resolutions of the radar and its RCS found as the product of the cell's area with the normalized RCS of the ocean.

An iterative (or Neumann Series) solution for the electric field scattered from a rough surface may be found by writing Equation (1.29) as

$$\begin{aligned} E_{0n}^{+} &= E^{s} + \mathcal{T}_1(E_{0n}^{+}) \\ &= E^{s} + \mathcal{T}_1(E^{s} + \mathcal{T}_1(E_{0n}^{+})) \\ &= E^{s} + \mathcal{T}_1(E^{s}) + \mathcal{T}_1^2(E_{0n}^{+}) \\ &= E^{s} + \mathcal{T}_1(E^{s}) + \mathcal{T}_1^2(E^{s}) + \mathcal{T}_1^3(E_{0n}^{+}) \\ &= \ldots \end{aligned} \tag{1.30}$$

or

$$E_{0n}^{+} = \sum_{m=0}^{\infty} \mathcal{T}_1^{m}(E^{s}) \tag{1.31}$$

For a vertical dipole transmitter located at the origin, the zero-order solution to

(1.31), $(E_{0n}^{+}) = \mathcal{T}_1^0(E^s) = E^s$, is shown to reduce to

$$E^s = C_0 F(\rho) \frac{e^{jk\rho}}{2\pi\rho} \quad , \tag{1.32}$$

where C_0 is defined as

$$C_0 = \frac{I \Delta l k^2}{j\omega\epsilon_0} \quad , \tag{1.33}$$

where I is the frequency-domain current on the dipole of length Δl with radian frequency ω. This solution may be recognized as the field propagated over a planar surface impedance. Higher order terms may be derived by successive application of the $\mathcal{T}_1$ operator, with each application of $\mathcal{T}_1$ corresponding to an individual scatter from the rough surface. It may be noted that in Walsh's original analysis [39], it is established that the monostatic Doppler spectrum agrees with measured results and the predictions of Barrick's [34] when limiting the analysis to second-order. For this reason, subsequent researchers employing the Walsh method have restricted attention to first- and second-order theory and the same limiting assumption is applied to this work.

Before writing out the first- and second-order expressions, it is convenient to provide a description of the rough surface. In past works, it has been common to first define the surface as time-invariant before introducing a temporal variation. For brevity and because the analysis in this work involves the ocean surface, a time-varying random rough surface description is directly introduced as

$$\xi(x, y, t) = \sum_{\vec{K}, \omega} P_{\vec{K}, \omega} e^{j\vec{K}\cdot\vec{\rho}} e^{j\omega t} \quad , \tag{1.34}$$

where $\vec{\rho}$ is the position vector in polar coordinates, t refers to the time evolution of the rough surface, and $P_{\vec{K},\omega}$ is the Fourier series coefficient associated with the surface wave vector, $\vec{K}$, and frequency, ω. Assuming the ocean surface is homogeneous and stationary [57], the stochastic nature of the surface may be introduced by assuming the $P_{\vec{K},\omega}$'s are normally distributed random variables with ensemble average

$$\left\langle P_{\vec{K},\omega} P^*_{\vec{K}',\omega'} \right\rangle = \begin{cases} S(\vec{K},\omega) d\vec{K} d\omega, & \vec{K} = \vec{K}', \omega = \omega' \\ 0, & \text{otherwise} \end{cases} , \tag{1.35}$$

where $S(\vec{K},\omega)$ is the power spectral density of the ocean surface. As the ocean surface is considered zero-mean and real valued, the Fourier coefficients are seen to satisfy

$$P_{-\vec{K},-\omega} = P^*_{\vec{K},\omega} \quad . \tag{1.36}$$

To account for second-order hydrodynamic effects, the Fourier coefficients in (1.34) may be expanded to second-order as

$$P_{\vec{K},\omega} = {}_1P_{\vec{K},\omega} + {}_2P_{\vec{K},\omega} \tag{1.37}$$

with ${}_1P_{\vec{K},\omega}$ and ${}_2P_{\vec{K},\omega}$ associated with first- and second-order waves respectively. The second-order coefficients are given by

$${}_2P_{\vec{K},\omega} = \sum_{\substack{\vec{K}=\vec{K}_1+\vec{K}_2 \\ \omega=\omega_1\omega_2}} {}_H\Gamma \, {}_1P_{\vec{K}_1,\omega_1} \, {}_1P_{\vec{K}_2,\omega_2} \quad , \tag{1.38}$$

where ${}_H\Gamma$ is a hydrodynamic coupling coefficient and for deep waves may be found from Hasselmann's analysis [58] as

$$
{}_H\Gamma = \frac{1}{2}\left\{K_1 + K_2 + \frac{g}{\omega_1\omega_2}(K_1K_2 - \vec{K}_1 \cdot \vec{K}_2)\left(\frac{gK + (\omega_1+\omega_2)^2}{gK - (\omega_1+\omega_2)^2}\right)\right\} \quad . \tag{1.39}
$$

g is the usual gravitational acceleration.

A final consideration in the surface description is the relation between the frequency and wavelength of the individual ocean wave components. This dispersion relation for first-order gravity waves is

$$
\omega = \sqrt{gK \tanh Kd} \tag{1.40}
$$

where ω is the angular frequency of the surface component associated with the wavenumber K that is traveling in water of depth, d. For sufficiently deep water depths, (1.40) may be approximated as

$$
\omega = \sqrt{gK} \quad . \tag{1.41}
$$

For a more detailed discussion on the specification of the surface in the context of the ocean and HF radar, including second-order effects and wave-wave interactions, the reader is referred to Chapter 3 of [9].

First-Order

A first-order scatter refers to the case where electromagnetic radiation from a radar transmitter is scattered a single time from a first-order ocean wave. This scenario and its associated geometry are depicted in Figure 1.2. Electromagnetic radiation from a transmitter, T, propagates along $\vec{\rho_1}$ and is scattered by the rough surface at (x_1, y_1) as indicated by the planar convolution operator. It then propagates along $\vec{\rho_2}$ before reaching the receiver, R. The first-order electric field can be expressed as the convolution

$$
\begin{aligned}
\left(E_{0n}^{+}\right)_1 = \mathcal{T}_1(E^s) &\sim -jkC_0 \left[\hat{\rho} \cdot \nabla_{xy}(\xi) F(\rho) \frac{e^{-jk\rho}}{2\pi\rho} \overset{xy}{*} F(\rho) \frac{e^{-jk\rho}}{2\pi\rho}\right] \\
&\sim -\frac{jkC_0}{4\pi^2} \int_{x_1} \int_{y_1} \hat{\rho}_1 \cdot \nabla_{x_1,y_1}(\xi(x_1 y_1)) \frac{F(\rho_1)F(\rho_2)}{\rho_1 \rho_2} e^{-jk(\rho_1+\rho_2)} dx_1 dy_1
\end{aligned}
\tag{1.42}
$$

where the asymptotic approximation, $\nabla_{xy}[C_0 F(\rho) \frac{e^{jk\rho}}{2\pi\rho}] \sim -jkC_0 F(\rho) \frac{e^{jk\rho}}{2\pi\rho} \hat{\rho}$, has been used. This simplifying assumption is justified in Appendix A of [9], where the surface gradient is found in polar coordinates as

$$
\begin{aligned}
\nabla_{xy}[C_0 F(\rho) \frac{e^{jk\rho}}{2\pi\rho}] &= \frac{\partial}{\partial\rho} \left(C_0 F(\rho) \frac{e^{jk\rho}}{2\pi\rho}\right) \hat{\rho} \\
&= -jkC_0 F(\rho) \frac{e^{jk\rho}}{2\pi\rho} \hat{\rho} + \mathbf{X}\hat{\rho} \quad ,
\end{aligned}
\tag{1.43}
$$

where $\mathbf{X}$ involves the derivatives of $F(\rho)$ and $\frac{1}{2\pi\rho}$. For large ρ, the terms in $\mathbf{X}$ are argued to be much less than the leading term and may be ignored in an asymptotic sense.

On substituting only first-order components of the ocean surface description, (1.34), into (1.42), the convolution is converted to elliptical (μ, α) coordinates and the α integral is evaluated using a stationary phase approximation. After introducing the distance variable, $\rho_s = \frac{\rho_1+\rho_2}{2}$, a pulsed dipole source is specified and the time-domain

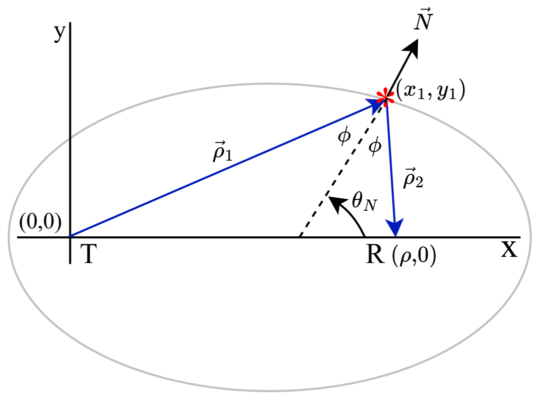

Figure 1.2: First-order rough surface scatter.

electric field is found through a temporal inverse Fourier transform as

$$\left(E_{0n}^{+}\right)_{11}(t_0, t) \approx \frac{-j\eta_0 \Delta l I_0 k_0^2}{(2\pi)^{\frac{3}{2}}} \sum_{\vec{K},\omega} {}_1P_{\vec{K},\omega} \sqrt{K\cos\phi_0}\, e^{j\frac{\vec{\rho}}{2}\cdot\vec{K}} e^{jk_0\Delta\rho_s} e^{j\omega t}$$
$$\cdot \frac{F(\rho_{01}, \omega_0)F(\rho_{02}, \omega_0)}{\sqrt{\rho_{0s}[\rho_{0s}^2 - (\frac{\rho}{2})^2]}} e^{-j\frac{\pi}{4}}\; e^{j\rho_{0s}K\cos\phi_0} \Delta\rho_s \mathrm{Sa}\left[\frac{\Delta\rho_s}{2}\left(\frac{K}{\cos\phi_0} - 2k_0\right)\right], \tag{1.44}$$

where $\mathrm{Sa}[\cdot]$ is the sampling or $\frac{\sin(x)}{x}$ function, I_0 is the amplitude of the excitation current, ω_0 is the centre frequency of the transmitted signal, and k_0 is its corresponding wavenumber. The first temporal variable, t_0, is understood as the total delay from transmit to receive and establishes a specific scattering ellipse. The second temporal variable, t, corresponds to the time evolution of the surface as previously discussed. Additionally, $\Delta\rho_s = \frac{c\tau_0}{2}$ is the bistatic patch width for a pulse radar with pulse width, τ_0, and c is the speed of light in free space. The 0 inserted in the subscripts of the quantities ρ_{01}, ρ_{02}, ρ_{0s}, ϕ_0 implies the variables are fixed to their central values for a specific patch of ocean. Lastly, the Sommerfeld attenuation functions have been modified to show they are evaluated for the constant centre frequency. It may be noted only surface components with vectors directed towards the outward pointing normal of the scattering ellipse contribute to the field in (1.44). Furthermore, the ellipse normal at this point is found to bisect the angle between the transmitter and receiver as viewed from the scattering point.

The first-order scattered electric field, (1.44), describes a stationary random process; thus its PSD may be found as the Fourier transform of its autocorrelation function. A convenient normalized form is introduced as

$$\mathcal{R}(\tau) = \frac{A_r}{2\eta_0} < E^{+}_{0_n}(t_0, t+\tau) E^{+*}_{0_n}(t_0, t) > \quad , \tag{1.45}$$

where η_0 is the intrinsic impedance of free space and t_0 is treated as a constant when evaluating the autocorrelation function for returns from a specific scattering ellipse. After applying a temporal Fourier transform to the autocorrelation of (1.44), the resulting PSD is compared with the radar equation to produce an equivalent RCS normalized per-unit area. To limit consideration to first-order effects, only the first-order component of the ocean wave spectrum is retained. The resulting RCS is

$$\sigma_{11}(\omega_d) = 2^4 \pi k_0^2 \sum_{m=\pm 1} S_1(m\vec{K}) \frac{K^{\frac{5}{2}} \cos\phi_0}{\sqrt{g}} \mathrm{Sa}^2 \left[\frac{\Delta\rho_s}{2} \left(\frac{K}{\cos\phi_0} - 2k_0 \right) \right] \quad , \tag{1.46}$$

where $S_1(m\vec{K})$ is the first-order component of the ocean wave spectrum, with positive and negative m corresponding to receding waves and advancing waves respectively. The square of the sampling function in (1.46) results in two major peaks in the first-order ocean cross section. Using the dispersion relation given in (1.41), these can be shown to occur for frequencies of

$$\omega_d = \pm\sqrt{2gk_0 \cos\phi} = \pm\omega_B = \pm 2\pi f_B \quad , \tag{1.47}$$

where the subscript B indicates these are referred to as Bragg frequencies [34].

Second-Order

A second-order scatter occurs when radiation from the transmitter is scattered a single time from a second-order ocean wave, or when the radiation is scattered twice from two distinct first-order ocean waves. The former case is generally referred to as the hydrodynamic contribution and a corresponding RCS expression may be derived by including the second-order ocean wave spectrum in (1.46). The latter case is referred to as the electromagnetic contribution. A derivation of a second-order electromagnetic scatter will first be detailed before including the hydrodynamic contribution in a total second-order RCS model.

Using (1.30) the second-order field that results from two electromagnetic scatters is

$$\left(E_{0n}^{+}\right)_2 = \mathcal{T}_1^2\{E^s\} = \mathcal{T}_1\{\mathcal{T}_1\{E^s\}\} \tag{1.48}$$

which from (1.42) can be written as

$$\left(E_{0n}^{+}\right)_2 = -jkC_0 \left\{ \nabla\xi \cdot \nabla_{xy} \left[\left(\hat{\rho} \cdot \nabla\xi F(\rho) \frac{e^{-jk\rho}}{2\pi\rho} \right) \overset{xy}{*} F(\rho) \frac{e^{-jk\rho}}{2\pi\rho} \right] \overset{xy}{*} F(\rho) \frac{e^{-jk\rho}}{2\pi\rho} \right\} \quad . \tag{1.49}$$

Using the differentiation and associative properties of convolutions, Gill [9] shows

(1.49) may also be expressed

$$\left(E_{0n}^{+}\right)_2 = -\frac{k^2 C_0}{(2\pi)^3}\left\{\left[\hat{\rho}\cdot\nabla\xi F(\rho)\frac{e^{-jk\rho}}{2\pi\rho}\right]_1 \overset{xy}{*} \left[\hat{\rho}\cdot\nabla\xi F(\rho)\frac{e^{-jk\rho}}{2\pi\rho}\right]_2 \overset{xy}{*} \left[F(\rho)\frac{e^{-jk\rho}}{2\pi\rho}\right]_3\right\} \quad . \tag{1.50}$$

A physical interpretation of this expression can be made with the aid of Figure 1.3. The $[\,]_1$ term describes propagation from the transmitter, T, along $\vec{\rho}_1$, and scattering at the first surface point, (x_1, y_1). Similarly, the propagation along $\vec{\rho}_{12}$ and scatter at (x_2, y_2) is accounted for in the $[\,]_2$ term. Finally, propagation along $\vec{\rho}_{20}$ from the second scatter point to the receiver, R, is described by $[\,]_3$

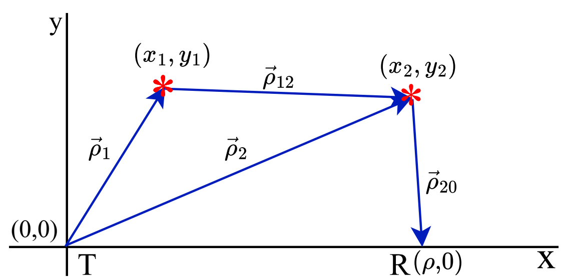

Figure 1.3: Second-order rough surface scatter.

In his doctoral thesis, Gill [9] applies a stationary phase analysis of the first convolution in (1.50) for a bistatic geometry and finds three significant contributions to the convolution integral. Referring to Figure 1.4, a physical meaning may be assigned to each of these contributions.

The first case is referred to as patch scatter when considering pulsed radar applications. Under this condition, $\rho_1 = \rho_2$, and both scatters occur at the 'same', location. This geometry is depicted in Figure 1.4a.

For the second case, $\rho_1 = 0$ and $\rho_{12} = \rho_2$. Thus, the first scatter occurs at the

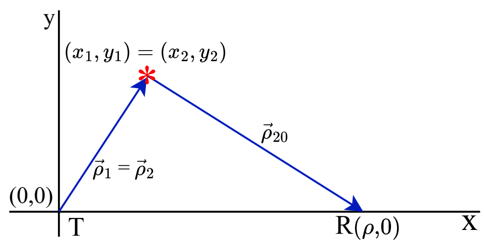

(a) Patch scatter.

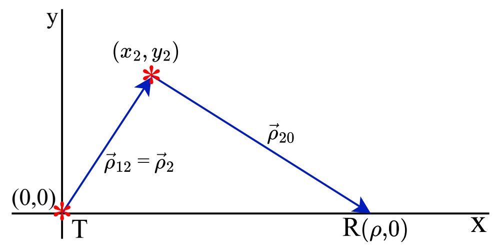

(b) Transmitter foot scatter.

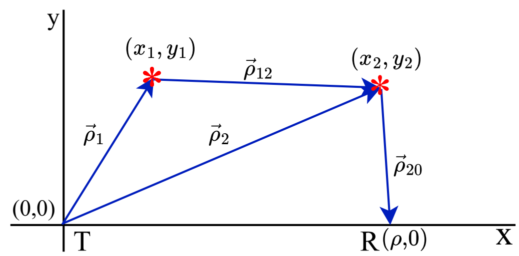

(c) Off-patch scatter.

Figure 1.4: Second-order scattering geometries.

transmitter, and the second occurs at a remote location (x_2, y_2) on the rough surface. This phenomenon has been referred to as foot scatter, specifically at the transmitter, and is depicted in Figure 1.4b. Gill also performs a 'backwards' analysis and finds that foot scatter can also occur at the receiver.

The last contribution is the general case and is referred to as off-patch scatter. In this case, shown in Figure 1.4c, both scatter points are remote from both the transmitter and receiver and must be at separate locations.

When considering shore-based HF radars, previous works [9, 59] have found that foot-scatter and off-patch scatter are generally negligible in comparison to patch scatter. For this reason, only the patch scatter case is considered in this work. After evaluating both convolutions in (1.50) for the patch-scatter case, a pulsed transmitting dipole is imposed as in the first-order analysis and an expression for the second-order electric field for patch scatter is derived. If only first-order components of the surface,

ξ, are considered, the patch scattered field is found as

$$\left(E_{0n}^{+}\right)_{2ep}(t_0,t) \approx \frac{-j\eta_0 \Delta l I_0 k_0^2}{(2\pi)^{\frac{3}{2}}} \sum_{\vec{K}_1,\omega_1} \sum_{\vec{K}_2,\omega_2} {}_1P_{\vec{K}_1,\omega_1}\, {}_1P_{\vec{K}_2,\omega_2} e^{j(\omega_1+\omega_2)t} \sqrt{K\cos\phi_0}$$
$$\cdot\, {}_E\Gamma_P(\vec{K}_1,\vec{K}_2) e^{j\frac{\vec{\rho}}{2}\cdot\vec{K}} e^{jk_0\Delta\rho_s} \frac{F(\rho_{01},\omega_0)F(\rho_{02},\omega_0)e^{-j\frac{\pi}{4}}}{\sqrt{\rho_{0s}[\rho_{0s}^2-(\frac{\rho}{2})^2]}} e^{j\rho_{0s}K\cos\phi_0} \tag{1.51}$$
$$\cdot\, \Delta\rho_s \mathrm{Sa}\left[\frac{\Delta\rho_s}{2}\left(\frac{K}{\cos\phi_0}-2k_0\right)\right] \quad ,$$

where $\vec{K}_1$, $\vec{K}_2$ and their associated quantities refer to the surface descriptions at the first and second scattering points respectively, and ${}_E\Gamma_P$ is defined as the electromagnetic coupling coefficient. For the patch scatter case, the vector sum of $\vec{K}_1$ and $\vec{K}_2$ must now be in the direction of the outward ellipse normal evaluated at the scattering point. It may be noted that in going from (1.50) to (1.51), Gill [9] uses a two-dimensional stationary phase approximation in elliptical coordinates to evaluate the first convolution. An updated analysis is derived in [44] for a radar installed on a moving platform. This refined analysis uses polar coordinates and a Sommerfeld-type integral in azimuth followed by a one-dimensional stationary phase approximation in the radial coordinate. When platform motion is removed, the updated analysis produces an expression equivalent to (1.51), with a new electromagnetic coupling coefficient that behaves similarly as the original expression derived in [9], but does not exhibit the non-physical singularities that were manually omitted in the computations of that work. The updated electromagnetic coupling coefficient, ${}_E\Gamma_P$, is used in this work and is given by

$${}_E\Gamma_P = \frac{jk_0}{K\cos\phi_0}(\vec{K}_1\cdot\hat{\rho}_2)(\hat{K}_s\cdot\vec{K}_2)G[K_s(\hat{\rho}_2,\vec{K}_1)] \quad , \tag{1.52}$$

where

$$\vec{K}_s(K_s, \theta_s) = k\hat{\rho}_2 - \vec{K}_1 \tag{1.53}$$

and

$$G[K_s(\hat{\rho}_2, \vec{K}_1)] = \frac{1}{K_s}\left[1 - j\frac{k(1+\Delta)}{\sqrt{K_s^2 - k^2 + jk\Delta}}\right] \quad , \tag{1.54}$$

with Δ being the surface impedance of the ocean. While the surface impedance is in general a frequency-dependent parameter, it is frequently considered constant over the narrow bandwidths of HF radar signals.

Before computing a second-order RCS for patch-scatter, a hydrodynamic contribution to the second-order electric field is found by substituting the second-order component of the ocean surface description, (1.38), for the first-order surface component in the first-order electric field (1.44). The resulting scattered field expression is denoted $(E_{0n}^{+})_{12}$, and corresponds to a single electromagnetic scatter from a second-order ocean wave. It is given by

$$\begin{aligned} \left(E_{0n}^{+}\right)_{12}(t_0, t) \approx \frac{-j\eta_0 \Delta l I_0 k_0^2}{(2\pi)^{\frac{3}{2}}} & \sum_{\vec{K}_1,\omega_1} \sum_{\vec{K}_2,\omega_2} {}_1P_{\vec{K}_1,\omega_1}\, {}_1P_{\vec{K}_2,\omega_2} e^{j(\omega_1+\omega_2)t} \sqrt{K\cos\phi_0} \\ & \cdot {}_H\Gamma_P(\vec{K}_1, \vec{K}_2) e^{j\frac{\vec{\rho}}{2}\cdot\vec{K}} e^{jk_0\Delta\rho_s} \frac{F(\rho_{01},\omega_0)F(\rho_{02},\omega_0)e^{-j\frac{\pi}{4}}}{\sqrt{\rho_{0s}[\rho_{0s}^2 - (\frac{\rho}{2})^2]}} e^{j\rho_{0s}K\cos\phi_0} \\ & \cdot \Delta\rho_s \mathrm{Sa}\left[\frac{\Delta\rho_s}{2}\left(\frac{K}{\cos\phi_0} - 2k_0\right)\right] \quad . \end{aligned} \tag{1.55}$$

The sum of (1.51) and (1.55) is considered the total second-order patch scattered field and is given by

$$\left(E_{0n}^{+}\right)_{2P}(t_0,t) \approx \frac{-j\eta_0 \Delta l I_0 k_0^2}{(2\pi)^{\frac{3}{2}}} \sum_{\vec{K}_1,\omega_1} \sum_{\vec{K}_2,\omega_2} {}_1P_{\vec{K}_1,\omega_1}\, {}_1P_{\vec{K}_2,\omega_2} e^{j(\omega_1+\omega_2)t} \sqrt{K\cos\phi_0}$$
$$\cdot\, \Gamma_P(\vec{K}_1,\vec{K}_2) e^{j\frac{\vec{\rho}}{2}\cdot\vec{K}} e^{jk_0\Delta\rho_s} \frac{F(\rho_{01},\omega_0)F(\rho_{02},\omega_0)e^{-j\frac{\pi}{4}}}{\sqrt{\rho_{0s}[\rho_{0s}^2-(\frac{\rho}{2})^2]}} e^{j\rho_{0s}K\cos\phi_0} \tag{1.56}$$
$$\cdot\, \Delta\rho_s \mathrm{Sa}\left[\frac{\Delta\rho_s}{2}\left(\frac{K}{\cos\phi_0}-2k_0\right)\right] \quad ,$$

where

$$\Gamma_P = {}_H\Gamma_P + {}_E\Gamma_P \quad . \tag{1.57}$$

Following the same approach that produced the first-order RCS from its corresponding electric field expression, a second-order RCS for patch scatter is derived as

$$\sigma_{2P}(\omega_d) = 2^3\pi k_0^2 \Delta\rho_s \sum_{m_1=\pm1}\sum_{m_2=\pm1} \int_0^{\infty}\int_{-\pi}^{\pi} \Big\{ S_1(m_1\vec{K}_1)S_1(m_2\vec{K}_2)$$
$$\cdot\, |{}_S\Gamma_P(\vec{K}_1,\vec{K}_2)|^2 K^2 \cos\phi_0 \mathrm{Sa}^2\left[\frac{\Delta\rho_s}{2}\left(\frac{K}{\cos\phi_0}-2k_0\right)\right] \tag{1.58}$$
$$\cdot\, \delta\left(\omega_d + m_1\sqrt{gK_1} + m_2\sqrt{gK_2}\right) K_1 \Big\} dK_1 d\theta_{\vec{K}_1} dK \quad ,$$

where ${}_S\Gamma_P(\vec{K}_1,\vec{K}_2)$ is a symmetrical form of the combined coupling coefficient, Γ_P, and is defined as

$${}_S\Gamma_P(\vec{K}_1,\vec{K}_2) = \frac{1}{2}[\Gamma_P(\vec{K}_1,\vec{K}_2) + {}_S\Gamma_P(\vec{K}_2,\vec{K}_1)] \quad . \tag{1.59}$$

1.4.2 Radar Cross Section Models of Deterministic Surface Targets

In [21], Walsh and Gill propose a method of adapting electric field equations governing scatter from a rough surface described as a Fourier series to model scattering from finite deterministic surface targets. The method expresses the target as an inverse Fourier transform which is substituted for the Fourier coefficients of the surface description. The Fourier summation over discrete surface components is then replaced with an integral over continuous surface components. The resulting expressions are simplified, and RCS models derived. In this work, the method is further extended to account for target motion as well as the presence of the surrounding ocean; thus, relevant details of the original work will be described here.

The method begins by describing the surface target as a height profile, $\xi_t(x, y)$. With reference to Figure 1.5, $\xi_t(x, y)$ is understood to be a function of x and y whose value is a height above the $z = 0$ plane and evaluates to zero everywhere outside the small, bounded region R. The two-dimensional Fourier transform of $\xi_t(x, y)$ is found as

$$\Xi_t(\vec{K}) = \int_x \int_y \xi_t(x, y) e^{-j\vec{K}\cdot\vec{\rho}} dx dy. \tag{1.60}$$

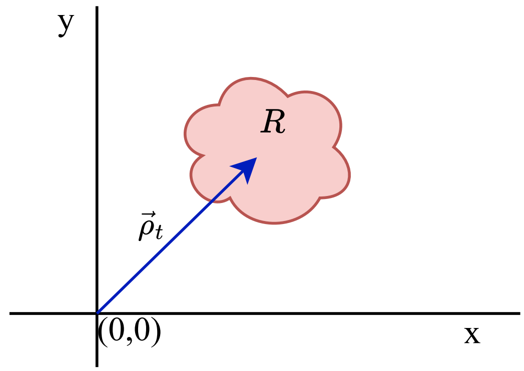

Figure 1.5: Discrete target definition geometry.

Using the change of variables

$$x' = x - x_t, \quad y' = y - y_t \quad , \tag{1.61}$$

an origin-shifted two-dimensional Fourier Transform, $\Xi_{t0}(\vec{K})$, is then introduced as

$$\begin{aligned} \Xi_{t0}(\vec{K}) &= \int_{x'}\int_{y'} \xi_t(x' + x_t, y' + y_t) e^{-j\vec{K}\cdot\vec{\rho}\,'} dx'dy' \\ &= e^{j\vec{K}\cdot\vec{\rho}_t} \int_x\int_y \xi_t(x, y) e^{-j\vec{K}\cdot\vec{\rho}} dxdy \quad , \end{aligned} \tag{1.62}$$

where

$$\vec{\rho} = x\hat{x} + y\hat{y} \quad , \quad \vec{\rho}\,' = x'\hat{x} + y'\hat{y}, \tag{1.63}$$

and

$$\vec{\rho}_t = \vec{\rho} - \vec{\rho}\,' = x_t\hat{x} + y_t\hat{y}. \tag{1.64}$$

The vector, $\vec{\rho}_t$, represents an arbitrary fixed location in R and is used as the origin for the Fourier transform. From (1.60) and (1.62), $\Xi_t(\vec{K})$ can also be expressed as

$$\Xi_t(\vec{K}) = e^{-j\vec{K}\cdot\vec{\rho}_t}\Xi_{t0}(\vec{K}) \quad , \tag{1.65}$$

such that $\xi_t(x, y)$ may be written as the inverse Fourier transform

$$\xi_t(x, y) = \frac{1}{(2\pi)^2}\int_{\vec{K}} e^{-j\vec{K}\cdot\vec{\rho}_t}\Xi_{t0}(\vec{K})e^{j\vec{K}\cdot\vec{\rho}}d\vec{K} \quad . \tag{1.66}$$

In [21], monostatic scattered electric field equations for a target described by (1.66) are found by modifying monostatic, time-invariant forms of the first- and second-order rough surface scattering fields, (1.44) and (1.51). For the first-order field, this modification takes the form of a single substitution,

$$P_{\vec{K}} \to e^{-j\vec{K}\cdot\vec{\rho}_t}\Xi_{t0}(\vec{K})\frac{d\vec{K}}{(2\pi)^2} \quad , \tag{1.67}$$

and conversion of the Fourier series to a Fourier integral. Similarly, the second-order substitution is

$$\begin{aligned} P_{\vec{K}_1} &\to e^{-j\vec{K}_1\cdot\vec{\rho}_t}\Xi_{t0}(\vec{K}_1)\frac{d\vec{K}_1}{(2\pi)^2} \\ P_{\vec{K}_2} &\to e^{-j\vec{K}_2\cdot\vec{\rho}_t}\Xi_{t0}(\vec{K}_2)\frac{d\vec{K}_2}{(2\pi)^2} \quad . \end{aligned} \tag{1.68}$$

Surface target radar cross section expressions are derived to second-order by comparing the magnitude squared of the scattered electric fields with the standard radar equation. The resulting total RCS is found as

$$\sigma = \left[\frac{16k_0^2}{\pi}|\mathcal{P}|^2\right] \quad , \tag{1.69}$$

where $\mathcal{P}$ is given by

$$\begin{aligned}\mathcal{P} = \Xi_{t0}(2k_0, \theta_1) + \frac{1}{2(2\pi)^2} \int_{\vec{K}} \Xi_{t0}(k_0\hat{\rho}_1 + \vec{K})\\ \cdot\, \Xi_{t0}(k_0\hat{\rho}_1 - \vec{K}) \frac{|\vec{K} \times \hat{\rho}_t|^2}{\sqrt{K^2 - k_0^2}} d\vec{K} \quad .\end{aligned} \tag{1.70}$$

where θ_1 is the angle of a vector, $\vec{\rho_1}$, pointing from the radar to the scattering point and $\hat{\rho}_1$ is the corresponding unit vector. In their analysis, Walsh and Gill [21] set the target origin to the nominal scattering point location, i.e. $\vec{\rho}_t = \vec{\rho}_1$.

1.5 Scope of the Thesis

This thesis presents a theoretical analysis of the scattered electric field from deterministic targets embedded in time-varying random rough surfaces. As discussed in Section 1.4, the foundation of the analysis is formed from two applications of the general scattering techniques developed and extended by Walsh and colleagues. These applications both consider the scattering of high frequency electromagnetic radiation but treat the cases of ocean scatter and finite, deterministic surface targets independently. By combining and extending aspects of each application, radar cross section models are derived for bistatic HFSWR targets that account for the target geometry and motion as well as the presence of the nearby surrounding ocean.

In Chapter 2, bistatic scattered electric field expressions are derived to second-order for a moving surface target embedded in a time-varying random rough surface. These expressions include first- and second-order components involving scattering solely from the deterministic target, and an additional target-ocean second-order expression corresponding to an electromagnetic scatter from the target followed by a secondary scatter from a point on the surface in close proximity to the target. The starting point for the analysis is the bistatic scattered electric fields from a rough surface after a pulsed dipole source has been imposed. The surface target definition is modified to allow for arbitrary motion. For scattering from the surface target only, the target substitutions are applied as described in Section 1.4.2. To account for the target-ocean scatter, only terms related to the first scattering point in the second-order rough surface scattered field are replaced with their deterministic target equivalents. The electric fields derived in this chapter are simplified to forms suitable for deriving RCS expressions.

Chapter 3 follows the established process in finding RCS models from time-varying electric field expressions. First, the target and target-ocean field components derived in this work are added to existing expressions for the scattered field from the ocean itself to form the total scattered electric field from an ocean patch containing a surface target. The autocorrelation function of the total field is then found through ensemble averaging and shown to reduce to the sum of the autocorrelation functions of each field component treated separately. Here, the properties of a zero-mean stationary Gaussian surface are imposed to simplify the autocorrelation functions before power spectral densities are found via a temporal Fourier transform. Lastly, RCS models are derived through a comparison of the spectral densities with the standard radar range equation. In this chapter, the motion of the surface target remains arbitrary to allow for more general applications of the results.

Chapter 4 demonstrates the utility of the derived RCS models through an application to a marine vessel moving with constant velocity. The chapter begins by simplifying the general motion expressions for the case of uniform linear motion. For the first-order target RCS, the resulting expression is found to contain the expected Doppler shift for a bistatic target. A surface target profile representative of a simplified *Visby*-class corvette hull is then introduced as an example target. The *Visby*-class features a tumblehome hull, which narrows as the height above the ocean surface increases. A radar system model is used to predict the total Doppler spectrum of the received signal from an ocean patch containing the target using the RCS models derived in this work and existing RCS models of the ocean surface. Doppler spectra are computed for varying radar geometries, sea-states, and target velocities and compared with the background sea-clutter in order to facilitate observations regarding the detectability of both the direct target scatter as well as the target-ocean scatter.

Chapter 5 contains a summary of the research completed in this work and proposes directions for future work.

Chapter 2

Electric Field Equations for a Deterministic Surface Target Embedded in a Time-Varying Random Rough Surface

2.1 Introduction

A method to obtain the scattered electric field from a non-moving deterministic surface target using the scattered electric field from a time-invariant rough surface represented as a Fourier series was presented by Walsh and Gill in [21]. In that work, the starting point was the first and second-order patch scatter expressions for a time-invariant rough surface where only a monostatic radar geometry was considered. In this chapter, the method will be extended to allow the surface target to move between radar acquisitions and applied to the bistatic expressions presented by Gill and Walsh [18] for the scattered electric field from a time-varying surface. Furthermore, an additional second-order target-ocean component (and its converse ocean-target component) will be found accounting for a secondary scatter from the ocean surface following a scatter from a target (or vice-versa).

In the derivations of both the rough surface scattering equations and their adaptation for deterministic surface target scattering, the authors in [21] employed a number of simplifying assumptions with the intention to apply the results to HF radar. As the analysis carried out in this chapter builds upon these derivations, the results will inherently rely on these same assumptions. As such, it is appropriate to summarize and comment on their implications in the context of surface targets before carrying out the analysis. The first key assumption is that the rough surface, and therefore target, is a good conductor. For marine vessels with metallic hulls, this is clearly suitable. Secondly, the rough surface is constrained to be electrically small in height. When modelling the RCS of a small hemisphere, Walsh and Gill [21] found their results consistent with Rayleigh theory, where the radius (or equivalently height for surface targets) is less than one tenth of a wavelength. At the lower end of the HF band, where many surveillance radars operate, the operating wavelength is 100 m; thus targets with heights up to 10 m may be modelled without violating this constraint. Thirdly, the slope of the rough surface or target must also be small. While this may prevent the models from perfectly modelling all features of a ship hull, Walsh and Gill noted that when neglecting the larger slopes of the hemisphere, the RCS contained the expected geometry dependence with only a constant proportional error. Lastly, the target should be able to be described as an inverse Fourier transform, meaning the height of the target should be a function of position in a flat plane. The implications of the last two assumptions related to the target's shape will be further addressed in an application in Chapter 4.

2.2 First-Order Scattered Field from a Deterministic Surface Target

The first-order analysis begins with equation (1.44), the electric field equation for first-order scatter from a time-varying rough surface for a pulsed dipole transmitting source. Repeating it here for convenience, the normal component of the scattered field is

$$\left(E_{0n}^{+}\right)_1(t_0,t) \approx \frac{-j\eta_0 \Delta l I_0 k_0^2}{(2\pi)^{\frac{3}{2}}} \sum_{\vec{K},\omega} P_{\vec{K},\omega} \sqrt{K\cos\phi_0}\, e^{j\frac{\vec{\rho}}{2}\cdot\vec{K}} e^{jk_0\Delta\rho_s} e^{j\omega t} \cdot \frac{F(\rho_{01},\omega_0)F(\rho_{02},\omega_0)}{\sqrt{\rho_{0s}[\rho_{0s}^2-(\frac{\rho}{2})^2]}} e^{-j\frac{\pi}{4}}\; e^{j\rho_{0s}K\cos\phi_0} \Delta\rho_s \mathrm{Sa}\left[\frac{\Delta\rho_s}{2}\left(\frac{K}{\cos\phi_0}-2k_0\right)\right], \tag{2.1}$$

where the surface is understood to be described by the time-varying Fourier series

$$\xi(x,y,t) = \sum_{\vec{K},\omega} P_{\vec{K},\omega} e^{j\vec{K}\cdot\vec{\rho}} e^{j\omega t} \quad . \tag{2.2}$$

To allow for target motion, the origin-shifted Fourier transform of the target profile, (1.62), is modified to vary with time, t, by re-writing it as

$$\begin{aligned} \Xi_{t0}(\vec{K}) &= \int_{x'}\int_{y'} \xi_t(x'+x_t(t), y'+y_t(t)) e^{-j\vec{K}\cdot\vec{\rho}'} dx'dy' \\ &= e^{j\vec{K}\cdot\vec{\rho}_t(t)} \int_x\int_y \xi_t(x,y) e^{-j\vec{K}\cdot\vec{\rho}} dxdy \quad , \end{aligned} \tag{2.3}$$

where $\vec{\rho}_t(t) = x_t(t)\hat{x} + y_t(t)\hat{y}$ is now a function of a temporal variable, t. Similar to the definition of the time-varying rough surface, (2.2), the time required for an appreciable change in target position is much greater than the delay between a radar transmission and reception, t_0. Thus, the target location may be assumed fixed during a single radar measurement. With this in mind, the 'surface' may be described as the inverse Fourier transform of (2.3), that is

$$\xi(x, y, t) = \frac{1}{(2\pi)^2} \int_{\vec{K}} e^{-j\vec{K}\cdot\vec{\rho}_t(t)} \Xi_{t0}(\vec{K}) e^{j\vec{K}\cdot\vec{\rho}} d\vec{K} \quad . \tag{2.4}$$

Comparing (2.4) and (2.2) in the context of (1.67), it is seen that the appropriate transformation to convert the summation over random surface components in (2.1) to a deterministic integral is

$$P_{\vec{K}\omega} e^{j\omega t} \rightarrow e^{-j\vec{K}\cdot\vec{\rho}_t(t)} \Xi_{t0}(\vec{K}) \frac{d\vec{K}}{(2\pi)^2} \quad . \tag{2.5}$$

Applying this transformation to (2.1), yields the first-order scattered electric field from a moving surface target. The result, denoted $(E_{0n}^{+})_{1t}$, is

$$\begin{aligned} \left(E_{0n}^{+}\right)_{1t}(t_0, t) \approx \frac{-j\eta_0 \Delta l I_0 k_0^2}{(2\pi)^{\frac{7}{2}}} \int_{\vec{K}} & e^{-j\vec{K}\cdot\vec{\rho}_t(t)} \Xi_{t0}(\vec{K}) \sqrt{K\cos\phi_0} \\ & \cdot e^{j\frac{\vec{\rho}}{2}\cdot\vec{K}} e^{j\rho_{0s} K \cos\phi_0} \Delta\rho_s \mathrm{Sa}\left[\frac{\Delta\rho_s}{2}\left(\frac{K}{\cos\phi_0} - 2k_0\right)\right] \\ & \cdot \frac{F(\rho_{01}, \omega_0) F(\rho_{02}, \omega_0) e^{-j\frac{\pi}{4}}}{\sqrt{\rho_{0s}[\rho_{0s}^2 - (\frac{\rho}{2})^2]}} e^{jk_0\Delta\rho_s} d\vec{K} \quad . \end{aligned} \tag{2.6}$$

The integral in (2.6) may be simplified by first expressing it in polar form

$$
\begin{aligned}
\left(E_{0n}^{+}\right)_{1t}(t_0,t) \approx & \frac{-j\eta_0 \Delta l I_0 k_0^2 F(\rho_{01},\omega_0) F(\rho_{02},\omega_0) e^{-j\frac{\pi}{4}}}{(2\pi)^{\frac{7}{2}}\sqrt{\rho_{0s}[\rho_{0s}^2-(\frac{\rho}{2})^2]}} e^{jk_0\Delta\rho_s} \\
& \cdot \int_K e^{j\rho_{0s}K\cos\phi_0} K\sqrt{K\cos\phi_0}\,\Delta\rho_s \mathrm{Sa}\left[\frac{\Delta\rho_s}{2}\left(\frac{K}{\cos\phi_0}-2k_0\right)\right] \\
& \cdot \int_{\theta_K} e^{-j\vec{K}\cdot\vec{\rho}_t} e^{j\frac{\vec{\rho}}{2}\cdot\vec{K}} \Xi_{t0}(\vec{K})\, d\theta_K\, dK \quad .
\end{aligned}
\tag{2.7}
$$

Next, $\vec{\rho}_t(t)$ is expressed as the sum of two components, one constant and one time-varying

$$
\vec{\rho}_t(t) = \vec{\rho}_{0t} + \vec{\delta\rho}_t(t) \quad , \tag{2.8}
$$

and a new vector, $\vec{\rho}\,'_{0t}$ is defined as

$$
\vec{\rho}\,'_{0t} = \vec{\rho}_{0t} - \frac{\vec{\rho}}{2} \quad . \tag{2.9}
$$

Using (2.8) and (2.9) in (2.7) , allows the θ_K integral to be written as

$$
\begin{aligned}
I_{\theta_K} &= \int_{\theta_K} e^{-j\vec{K}\cdot\vec{\rho}_t} e^{j\frac{\vec{\rho}}{2}\cdot\vec{K}} \Xi_{t0}(\vec{K})\, d\theta_K \\
&= \int_{\theta_K} e^{-j\vec{K}\cdot\vec{\delta\rho}_t(t)} e^{-j\vec{K}\cdot\vec{\rho}\,'_{0t}} \Xi_{t0}(\vec{K})\, d\theta_K \\
&= \int_{\theta_K} e^{-j\vec{K}\cdot\vec{\delta\rho}_t(t)} \Xi_{t0}(\vec{K}) e^{-jK\rho'_{0t}\cos(\theta_K-\theta_{\rho'_{0t}})}\, d\theta_K
\end{aligned}
\tag{2.10}
$$

With the intention of applying a stationary phase approximation to (2.10), it is first noted that the sampling function in (2.7) will limit contributions to values of $K \approx 2k_0\cos\phi_0$ and that in the HF band, k_0 will be on the order 10^{-2} to $10^{-1}\mathrm{m}^{-1}$. Furthermore, targets of interest to coastal HF radar operators are likely to be 10's to

100's of kilometers from either transmitter, receiver, or the centre point on the line between them. Thus, the product $K\rho_{0t}'$ may be assumed large, and the application of the stationary phase method is appropriate. This assumption requires that the time-varying component of the target origin, $\vec{\delta\rho}_t(t)$, is small with respect to both $\vec{\rho}_{0t}$ and $\vec{\rho}_{0t}'$ or that the total target displacement over multiple radar acquisitions is small relative to the distances to the transmitter, receiver, or the centre-point of the line between them.

As a first step in applying the approximation, the stationary points are found as the solution to

$$\frac{d\cos(\theta_K - \theta_{\rho_{0t}'})}{d\theta_K} = 0 \quad . \tag{2.11}$$

Solving (2.11) yields the following condition

$$\theta_K = \theta_{\rho_{0t}'} \ , \ \theta_{\rho_{0t}'} + \pi \quad . \tag{2.12}$$

Recalling that only surface components with $\vec{K}$ directed towards the outward pointing normal of the scattering ellipse contribute to (2.1) and by extension (2.7), the solution in (2.12) is valid only if $\theta_{\rho_{0t}'} = \theta_N$, where θ_N is the angle the normal of the ellipse makes with the x axis. Thus, only the first stationary point found in (2.12) is meaningful. With this in mind, the θ_K integral may be approximated as

$$\begin{aligned} I_{\theta_K} &\approx \sqrt{2\pi}\,\Xi_{t0}(\vec{K})e^{-j\vec{K}\cdot\delta\vec{\rho}_t(t)} \left. \frac{e^{-j\vec{\rho}_{0t}{}'\cdot\vec{K}}}{\sqrt{-j\vec{K}\cdot\vec{\rho}_{0t}{}'}} \right|_{\theta_K=\theta_{\rho_{0t}'}} \\ &\approx \sqrt{2\pi}\,\Xi_{t0}(\vec{K})e^{-j\vec{K}\cdot\delta\vec{\rho}_t(t)} \frac{e^{-jK\rho_{0t}'}}{\sqrt{K\rho_{0t}'}} e^{j\frac{\pi}{4}} \quad . \end{aligned} \tag{2.13}$$

Substituting (2.13) into the first-order field expression, (2.7), yields

$$
\begin{aligned}
\left(E_{0n}^{+}\right)_{1t}(t_0,t) \approx & \frac{-j\eta_0 \Delta l I_0 k_0^2 F(\rho_{01},\omega_0)F(\rho_{02},\omega_0)}{(2\pi)^3\sqrt{\rho'_{0t}\rho_{0s}[\rho_{0s}^2-(\frac{\rho}{2})^2]}} e^{jk_0\Delta\rho_s} \\
& \cdot \int_K e^{j\rho_{0s}K\cos\phi_0} e^{-jK\rho'_{0t}} e^{-j\vec{K}\cdot\delta\vec{\rho}_t(t)} K\sqrt{\cos\phi_0} \\
& \cdot \Xi_{t0}(\vec{K})\Delta\rho_s \mathrm{Sa}\left[\frac{\Delta\rho_s}{2}\left(\frac{K}{\cos\phi_0}-2k_0\right)\right] dK \ .
\end{aligned}
\tag{2.14}
$$

To evaluate the K integration, the radar patch width, $\Delta\rho_s$, is assumed sufficiently large such that

$$
\Delta\rho_s \mathrm{Sa}\left[\frac{\Delta\rho_s}{2}\left(\frac{K}{\cos\phi_0}-2k_0\right)\right] \rightarrow 2\pi\cos\phi_0\delta(K-2k_0\cos\phi_0) \quad , \tag{2.15}
$$

where $\delta(\cdot)$ is the familiar Dirac delta function. The monostatic equivalent of (2.15) was used by Walsh and Gill [21] in developing cross sections of surface targets, while Gill [9] employed the assumption as written in computing second-order ocean cross sections. When (2.15) is applied to (2.14), the K integral yields to the Dirac delta function and the first-order scattered electric field from a moving target reduces to

$$
\begin{aligned}
\left(E_{0n}^{+}\right)_{1t}(t_0,t) \approx & \frac{-j2\eta_0 \Delta l I_0 k_0^3 F(\rho_{01},\omega_0)F(\rho_{02},\omega_0)}{(2\pi)^2\sqrt{\rho'_{0t}\rho_{0s}[\rho_{0s}^2-(\frac{\rho}{2})^2]}} \sqrt{\cos^5\phi_0}\,\Xi_{t0}(\vec{K}) \\
& \cdot e^{jk_0\Delta\rho_s} e^{j\rho_{0s}K\cos\phi_0} e^{-jK\rho'_{0t}} e^{-j\vec{K}\cdot\delta\vec{\rho}_t(t)} \ ,
\end{aligned}
\tag{2.16}
$$

where K is now understood to be equal to $2k_0\cos\phi_0$. As a last step in the simplification of the first-order scattered field, the distance, ρ'_{0t}, will be assumed to be approximately equal to the radius of curvature of the scattering ellipse at centre of the scattering patch, ρ_{0c}. When combined with the stationary phase condition, (2.12), this suggests

$$\vec{\rho}'_{0t} = \rho_{0c}\hat{N} \quad , \tag{2.17}$$

where $\hat{N}$ is the unit vector of the outward pointing normal of the scattering ellipse. If the central scattering point (x_{01}, y_{01}) is located at the target reference location (x_t, y_t), (2.17) is only satisfied for monostatic radar geometries. While this assumption provides a convenient 'special case', Appendix B shows equivalent general bistatic expressions result for a continuous wave source and an arbitrarily located rectangular scattering patch. On noting that the radius of curvature can be expressed as found in [9] as

$$\rho_{0c} = \frac{(\rho_{01}\rho_{02})^{\frac{3}{2}}}{\rho_{0s}\sqrt{\rho_{0s}^2 - \left(\frac{\rho}{2}\right)^2}} \quad , \tag{2.18}$$

using (2.17) in (2.16) results in

$$\begin{aligned} \left(E_{0n}^{+}\right)_{1t}(t_0, t) \approx & \frac{-j2\eta_0 \Delta l I_0 k_0^3 F(\rho_{01}, \omega_0) F(\rho_{02}, \omega_0)}{(2\pi)^2 \rho_{01}\rho_{02}} \cos^2\phi_0 \Xi_{t0}(\vec{K}) \\ & \cdot e^{jk_0\Delta\rho_s} e^{j\rho_{0s}K\cos\phi_0} e^{-jK\rho'_{0c}} e^{-j\vec{K}\cdot\delta\vec{\rho}_t(t)} \quad , \end{aligned} \tag{2.19}$$

where the identity $\rho_{0s}^2 - (\frac{\rho}{2})^2 = \rho_{01}\rho_{02}\cos^2\phi_0$ has been used.

2.3 Second-Order Scattered Field from a Deterministic Surface Target

A second-order scatter from a deterministic surface target refers to the case where electromagnetic radiation from a radar transmitter experiences two scatters before being measured at a receiver. It follows that the second-order expression for patch scatter from a rough surface, (1.51), is a suitable starting point for the analysis. This expression, repeated here for completeness, is given by

$$\left(E_{0n}^{+}\right)_{2ep}(t_0,t) \approx \frac{-j\eta_0 \Delta l I_0 k_0^2}{(2\pi)^{\frac{3}{2}}} \sum_{\vec{K}_1,\omega_1} \sum_{\vec{K}_2,\omega_2} P_{\vec{K}_1,\omega_1} P_{\vec{K}_2,\omega_2} e^{j(\omega_1+\omega_2)t} \sqrt{K\cos\phi_0}\, {}_{E}\Gamma_P(\vec{K}_1,\vec{K}_2)$$
$$\cdot\, e^{j\frac{\vec{\rho}}{2}\cdot\vec{K}} e^{jk_0\Delta\rho_s} \frac{F(\rho_{01},\omega_0)F(\rho_{02},\omega_0)e^{-j\frac{\pi}{4}}}{\sqrt{\rho_{0s}[\rho_{0s}^2-(\frac{\rho}{2})^2]}} e^{j\rho_{0s}K\cos\phi_0}$$
$$\cdot\, \Delta\rho_s \mathrm{Sa}\left[\frac{\Delta\rho_s}{2}\left(\frac{K}{\cos\phi_0}-2k_0\right)\right] \quad . \tag{2.20}$$

To produce second-order cross section expressions for surface targets from (2.20), the transformation defined in (2.5) must be applied to terms corresponding to the first and second scattering points separately. Here, that takes the form of

$$\begin{aligned} P_{\vec{K}_1,\omega_1} e^{j\omega_1 t} &\rightarrow e^{-j\vec{K}_1\cdot\vec{\rho}_t(t)} \Xi_{t0}(\vec{K}_1) \frac{d\vec{K}_1}{(2\pi)^2} \\ P_{\vec{K}_2,\omega_2} e^{j\omega_2 t} &\rightarrow e^{-j\vec{K}_2\cdot\vec{\rho}_t(t)} \Xi_{t0}(\vec{K}_2) \frac{d\vec{K}_2}{(2\pi)^2} \quad . \end{aligned} \tag{2.21}$$

Applying (2.21) to (2.20) gives

$$\left(E_{0n}^{+}\right)_{2t}(t_0,t) \approx \frac{-j\eta_0 \Delta l I_0 k_0^2}{(2\pi)^{\frac{11}{2}}} \int_{\vec{K}_1}\int_{\vec{K}_2} e^{-j\vec{K}_1\cdot\vec{\rho}_t(t)} \Xi_{t0}(\vec{K}_1) e^{-j\vec{K}_2\cdot\vec{\rho}_t(t)} \Xi_{t0}(\vec{K}_2)$$
$$\cdot\, \sqrt{K\cos\phi_0}\, {}_{E}\Gamma_P(\vec{K}_1,\vec{K}_2) \frac{F(\rho_{01},\omega_0)F(\rho_{02},\omega_0)e^{-j\frac{\pi}{4}}}{\sqrt{\rho_{0s}[\rho_{0s}^2-(\frac{\rho}{2})^2]}}$$
$$\cdot\, e^{j\frac{\vec{\rho}}{2}\cdot\vec{K}} e^{jk_0\Delta\rho_s} e^{j\rho_{0s}K\cos\phi_0}$$
$$\cdot\, \Delta\rho_s \mathrm{Sa}\left[\frac{\Delta\rho_s}{2}\left(\frac{K}{\cos\phi_0}-2k_0\right)\right] d\vec{K}_1 d\vec{K}_2 \quad , \tag{2.22}$$

where the subscript $2t$ indicates a second-order electromagnetic scatter from a surface target. Using the fact that $\vec{K} = \vec{K}_1 + \vec{K}_2$, the integration over $\vec{K}_2$ may be changed to an integration over $\vec{K}$. After expressing the resulting $\vec{K}$ integration in polar form, the second-order target scattered electric field is

$$
\begin{aligned}
\left(E_{0n}^{+}\right)_{2t}(t_0,t) \approx & \frac{-j\eta_0 \Delta l I_0 k_0^2}{(2\pi)^{\frac{11}{2}}} \frac{F(\rho_{01},\omega_0)F(\rho_{02},\omega_0)e^{-j\frac{\pi}{4}}}{\sqrt{\rho_{0s}[\rho_{0s}^2-(\frac{\rho}{2})^2]}} e^{jk_0\Delta\rho_s} \\
& \cdot \int_{\vec{K}1} \Xi_{t0}(\vec{K}_1) \int_K K\sqrt{K\cos\phi_0}\, e^{j\rho_{0s}K\cos\phi_0} \\
& \cdot \Delta\rho_s \mathrm{Sa}\left[\frac{\rho_s}{2}\left(\frac{K}{\cos\phi_0}-2k_0\right)\right] \int_{\theta_K} {}_E\Gamma_P(\vec{K}_1,\vec{K}-\vec{K}_1) \\
& \cdot \Xi_{t0}(\vec{K}-\vec{K}_1) e^{-j\vec{K}\cdot[\vec{\rho}_t(t)-\frac{\rho}{2}]} d\theta_K dK d\vec{K}_1 \quad .
\end{aligned}
\tag{2.23}
$$

Similar to the first-order target scatter analysis, only the θ_K integration will be considered. Using the definitions (2.8) and (2.9), I_{θ_K}, is

$$
\begin{aligned}
I_{\theta_K} &= \int_{\theta_K} {}_E\Gamma_P(\vec{K}_1,\vec{K}-\vec{K}_1)\Xi_{t0}(\vec{K}-\vec{K}_1)e^{-j\vec{K}\cdot[\vec{\rho}_t(t)-\frac{\rho}{2}]}d\theta_K \\
&= \int_{\theta_K} {}_E\Gamma_P(\vec{K}_1,\vec{K}-\vec{K}_1)e^{-j\vec{K}\cdot\delta\vec{\rho}_t(t)}e^{-j\vec{K}\cdot\vec{\rho}'_{0t}}\Xi_{t0}(\vec{K}-\vec{K}_1)d\theta_K \\
&= \int_{\theta_K} {}_E\Gamma_P(\vec{K}_1,\vec{K}-\vec{K}_1)e^{-j\vec{K}\cdot\delta\vec{\rho}_t(t)}\Xi_{t0}(\vec{K}-\vec{K}_1)e^{-jK\rho'_{0t}\cos(\theta_K-\theta_{\rho'_{0t}})}d\theta_K \ .
\end{aligned}
\tag{2.24}
$$

The exponential in (2.24) is exactly the same as the exponential seen in (2.10). Thus, using the same arguments in Section 2.2, a stationary phase approximation of the integral is deemed appropriate. Furthermore, the stationary analysis follows the results of (2.13), allowing (2.24) to be re-written as

$$
I_{\theta_K} \approx \sqrt{2\pi}\, {}_E\Gamma_P(\vec{K}_1,\vec{K}-\vec{K}_1)\Xi_{t0}(\vec{K}-\vec{K}_1)e^{-j\vec{K}\cdot\delta\vec{\rho}_t(t)}\frac{e^{-jK\rho'_{0t}}}{\sqrt{K\rho'_{0t}}}e^{j\frac{\pi}{4}} \quad , \tag{2.25}
$$

where it is understood that $\theta_{\rho'_{0t}} = \theta_K = \theta_N$. On substituting the result of (2.25) into

(2.23), the second-order scattered field from a surface target becomes

$$\left(E_{0n}^{+}\right)_{2t}(t_0,t) \approx \frac{-j\eta_0 \Delta l I_0 k_0^2}{(2\pi)^5} \frac{F(\rho_{01},\omega_0)F(\rho_{02},\omega_0)}{\sqrt{\rho'_{0t}\rho_{0s}[\rho_{0s}^2-(\frac{\rho}{2})^2]}} e^{jk_0\Delta\rho_s}$$
$$\cdot \int_{\vec{K}1} \Xi_{t0}(\vec{K}_1) \int_K K\sqrt{\cos\phi_0} e^{j\rho_{0s}K\cos\phi_0} \Delta\rho_s \mathrm{Sa}\left[\frac{\rho_s}{2}\left(\frac{K}{\cos\phi_0}-2k_0\right)\right]$$
$$\cdot\, {}_E\Gamma_P(\vec{K}_1,\vec{K}-\vec{K}_1)\Xi_{t0}(\vec{K}-\vec{K}_1)e^{-j\vec{K}\cdot\delta\vec{\rho}_t(t)}e^{-jK\rho'_{0t}}dKd\vec{K}_1\ . \tag{2.26}$$

Using the result of the long pulse assumption from (2.15), the sampling function in (2.26) may be replaced with a Dirac delta function and the K integral can be immediately evaluated to give

$$\left(E_{0n}^{+}\right)_{2t}(t_0,t) \approx \frac{-j2\eta_0 \Delta l I_0 k_0^3}{(2\pi)^4} \frac{F(\rho_{01},\omega_0)F(\rho_{02},\omega_0)}{\sqrt{\rho'_{0t}\rho_{0s}[\rho_{0s}^2-(\frac{\rho}{2})^2]}} e^{jk_0\Delta\rho_s}\cos^{5/2}\phi_0$$
$$\cdot \int_{\vec{K}1} \Xi_{t0}(\vec{K}_1)\Xi_{t0}(\vec{K}-\vec{K}_1)e^{j\rho_{0s}K\cos\phi_0} \tag{2.27}$$
$$\cdot\, {}_E\Gamma_P(\vec{K}_1,\vec{K}-\vec{K}_1)e^{-j\vec{K}\cdot\delta\vec{\rho}_t(t)}e^{-jK\rho'_{0t}}d\vec{K}_1\ ,$$

where it is now understood that $\vec{K} = 2k_0\cos\phi_0\hat{N}$. If it is agreed to set $\rho'_{0t} \approx \rho_{0c}$ as was done for the first-order expressions, (2.27) is further reduced to

$$\left(E_{0n}^{+}\right)_{2t}(t_0,t) \approx \frac{-j2\eta_0 \Delta l I_0 k_0^3}{(2\pi)^4} \frac{F(\rho_{01},\omega_0)F(\rho_{02},\omega_0)}{\rho_{01}\rho_{02}}\cos^2\phi_0$$
$$\cdot\, e^{jk_0\Delta\rho_s}e^{j\rho_{0s}K\cos\phi_0}e^{-j\vec{K}\cdot\delta\vec{\rho}_t(t)}e^{-jK\rho_{0c}} \tag{2.28}$$
$$\cdot \int_{\vec{K}1} \Xi_{t0}(\vec{K}_1)\Xi_{t0}(\vec{K}-\vec{K}_1)\ {}_E\Gamma_P(\vec{K}_1,\vec{K}-\vec{K}_1)d\vec{K}_1\ ,$$

where the identity $\rho_{0s}^2 - (\frac{\rho}{2})^2 = \rho_{01}\rho_{02}\cos^2\phi_0$ has been used.

The $\vec{K}_1$ integration in (2.28) can be re-written following the additional simplification steps taken in [21] by first noting $\vec{K}_2 = \vec{K} - \vec{K}_1$, giving

$$
\begin{aligned}
I_{\vec{K}_1} &= \int_{\vec{K}1} \Xi_t(\vec{K}_1)\Xi_t(\vec{K} - \vec{K}_1)\,{}_E\Gamma_P(\vec{K}_1, \vec{K} - \vec{K}_1)d\vec{K}_1 \\
&= \int_{\vec{K}_2} \Xi_{t0}(\vec{K} - \vec{K}_2)\Xi_{t0}(\vec{K}_2)\,{}_E\Gamma_P(\vec{K} - \vec{K}_2, \vec{K}_2)d\vec{K}_2 \\
&= \int_{\vec{K}'} \Xi_{t0}(\vec{K}')\Xi_{t0}(\vec{K} - \vec{K}') \\
&\cdot \left\{\frac{1}{2}\left[{}_E\Gamma_P(\vec{K}', \vec{K} - \vec{K}') + {}_E\Gamma_P(\vec{K} - \vec{K}', \vec{K}')\right]\right\} d\vec{K}'\ ,
\end{aligned}
\tag{2.29}
$$

where the last equality in (2.29) results from the fact that both $\vec{K}_1$ and $\vec{K}_2$ are over all wavenumber space. The expression within the braces may be recognized as a symmetrical electromagnetic coefficient, more commonly written as

$$
{}_{SE}\Gamma_P(\vec{K}_1, \vec{K}_2) = \frac{1}{2}\left[{}_E\Gamma_P(\vec{K}_1, \vec{K}_2) + {}_E\Gamma_P(\vec{K}_2, \vec{K}_1)\right]. \tag{2.30}
$$

As a final simplification, (2.29) may be re-written using the variable change

$$
\vec{K}' = \vec{K}'' + \frac{\vec{K}}{2} = \vec{K}'' + k_0 \cos\phi_0 \quad , \tag{2.31}
$$

with the result being

$$
\begin{aligned}
I_{\vec{K}_1} = \int_{\vec{K}''} &\Xi_{t0}(k_0\cos\phi_0\hat{N} + \vec{K}'')\Xi_{t0}(k_0\cos\phi_0\hat{N} - \vec{K}'') \\
&\cdot {}_{SE}\Gamma_P(k_0\cos\phi_0\hat{N} + \vec{K}'', k_0\cos\phi_0\hat{N} - \vec{K}'')d\vec{K}'' \quad .
\end{aligned}
\tag{2.32}
$$

Substituting (2.32) into (2.27) gives the final expression for the second-order target field as

$$
\begin{aligned}
\left(E_{0n}^{+}\right)_{2t}(t_0,t) \approx & \frac{-j2\eta_0 \Delta l I_0 k_0^3}{(2\pi)^4} \frac{F(\rho_{01},\omega_0)F(\rho_{02},\omega_0)}{\rho_{01}\rho_{02}} \cos^2\phi_0 \\
& \cdot e^{jk_0\Delta\rho_s} e^{j\rho_{0s}K\cos\phi_0} e^{-j\vec{K}\cdot\delta\vec{\rho}_t(t)} e^{-jK\rho_{0c}} \\
& \cdot \int_{\vec{K}''} \Xi_{t0}(k_0\cos\phi_0\hat{N} + \vec{K}'')\Xi_{t0}(k_0\cos\phi_0\hat{N} - \vec{K}'') \\
& \cdot {}_{SE}\Gamma_P(k_0\cos\phi_0\hat{N} + \vec{K}'', k_0\cos\phi_0\hat{N} - \vec{K}'')d\vec{K}'' \quad .
\end{aligned}
\tag{2.33}
$$

Noting the similarities between the first- and second-order target scattered field expressions given in (2.19) and (2.33) respectively, a combined scattered electric field can be found by summing the components. The total target scattered field may then be written as

$$
\begin{aligned}
\left(E_{0n}^{+}\right)_{t}(t_0,t) \approx & \frac{-j2\eta_0 \Delta l I_0 k_0^3}{(2\pi)^2} \frac{F(\rho_{01},\omega_0)F(\rho_{02},\omega_0)}{\rho_{01}\rho_{02}} \cos^2\phi_0 \mathcal{P}_0(2k_0\cos\phi_0\hat{N}) \\
& \cdot e^{jk_0\Delta\rho_s} e^{j\rho_{0s}K\cos\phi_0} e^{-j\vec{K}\cdot\delta\vec{\rho}_t(t)} e^{-jK\rho_{0c}}
\end{aligned}
\tag{2.34}
$$

where $\mathcal{P}_0$ is a function of surface wave number defined by

$$
\begin{aligned}
\mathcal{P}_0(\vec{K}) = & \Xi_{t0}(\vec{K}) + \frac{1}{(2\pi)^2} \int_{\vec{K}''} \Xi_{t0}\left(\frac{\vec{K}}{2} + \vec{K}''\right) \Xi_{t0}\left(\frac{\vec{K}}{2} - \vec{K}''\right) \\
& \cdot \quad {}_{SE}\Gamma_P\left(\frac{\vec{K}}{2} + \vec{K}'', \frac{\vec{K}}{2} - \vec{K}''\right) d\vec{K}'' \, .
\end{aligned}
\tag{2.35}
$$

2.4 Second-Order Target-Ocean Scattered Field from a Deterministic Surface Target and Time-varying Random Rough Surface

A second-order scatter involving both a target and the surrounding surface is depicted in Figure 2.1. In this scenario, referred to as target-ocean scatter, radiation from the transmitter is first scattered by a deterministic target before being scattered a second time from the randomly rough ocean surface.

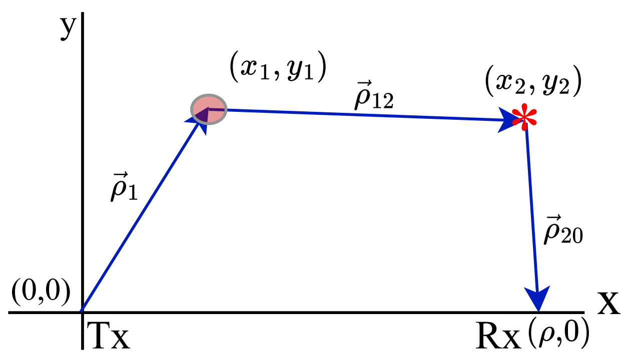

Figure 2.1: General target-ocean scattering geometry.

If the transformation described by (2.21) is applied to only the first scattering point in (2.20), an expression is obtained which describes the scattered electric field when the secondary scatter is near the target. The relevant geometry is depicted in Figure 2.2. This second-order target-ocean patch scatter field, denoted as $(E_{0n}^{+})_{2to}$, is given by

$$
\begin{aligned}
\left(E_{0n}^{+}\right)_{2to}(t_0,t) \approx\ & \frac{-j\eta_0 \Delta l I_0 k_0^2}{(2\pi)^{\frac{7}{2}}} \int_{\vec{K}_1} \sum_{\vec{K}_2,\omega_2} e^{-j\vec{K}_1\cdot\vec{\rho}_t(t)} \Xi_{t0}(\vec{K}_1) e^{j\omega_2 t}\, {}_1P_{\vec{K}_2,\omega_2} \\
& \cdot e^{j\frac{\vec{\rho}}{2}\cdot\vec{K}} e^{jk_0\Delta\rho_s} e^{j\rho_{0s}K\cos\phi_0}\, {}_E\Gamma_P(\vec{K}_1,\vec{K}_2)\sqrt{K\cos\phi_0} \\
& \cdot \frac{F(\rho_{01},\omega_0)F(\rho_{02},\omega_0)e^{-j\frac{\pi}{4}}}{\sqrt{\rho_{0s}[\rho_{0s}^2-(\frac{\rho}{2})^2]}} \Delta\rho_s \mathrm{Sa}\left[\frac{\Delta\rho_s}{2}\left(\frac{K}{\cos\phi_0}-2k_0\right)\right] d\vec{K}_1 \quad .
\end{aligned} \tag{2.36}
$$

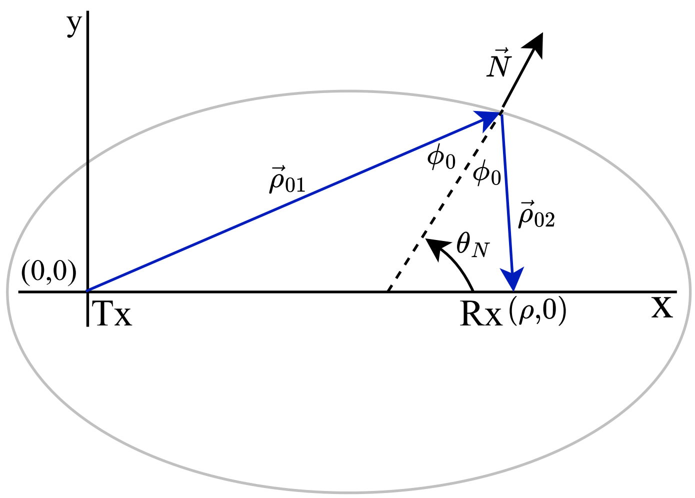

Figure 2.2: Target-ocean patch scatter geometry.

To simplify this expression, the integration variable in (2.36) is first changed to $\vec{K} = \vec{K}_1 + \vec{K}_2$ and the transformed integral is expressed in polar coordinates. This process yields

$$
\begin{aligned}
\left(E_{0n}^{+}\right)_{2to}(t_0,t) \approx\ & \frac{-j\eta_0 \Delta l I_0 k_0^2}{(2\pi)^{\frac{7}{2}}} \frac{F(\rho_{01},\omega_0)F(\rho_{02},\omega_0)e^{-j\frac{\pi}{4}}}{\sqrt{\rho_{0s}[\rho_{0s}^2-(\frac{\rho}{2})^2]}} \\
& \cdot e^{jk_0\Delta\rho_s} \sum_{\vec{K}_2,\omega_2} e^{j\omega_2 t}\, {}_1P_{\vec{K}_2,\omega_2} e^{j\vec{K}_2\cdot\vec{\rho}_t(t)} \\
& \cdot \int_K K\sqrt{K\cos\phi_0}\, e^{j\rho_{0s}K\cos\phi_0} \Delta\rho_s \mathrm{Sa}\left[\frac{\Delta\rho_s}{2}\left(\frac{K}{\cos\phi_0}-2k_0\right)\right] \\
& \cdot \int_{\theta_K} \Xi_{t0}(\vec{K}-\vec{K}_2)\, {}_E\Gamma_P(\vec{K}-\vec{K}_2,\vec{K}_2) e^{-j\vec{K}\cdot\left[\vec{\rho}_t(t)-\frac{\vec{\rho}}{2}\right]} d\theta_K dK \quad .
\end{aligned}
\tag{2.37}
$$

The θ_K integral is seen to be of the same form as the θ_{K_1} integral in the second-order target expression (2.23) if the definitions given in (2.8) and (2.9) are used. It follows from (2.24) and (2.25) that (2.37) can be immediately simplified to

$$
\begin{aligned}
\left(E_{0n}^{+}\right)_{2to}(t_0,t) \approx\ & \frac{-j\eta_0 \Delta l I_0 k_0^2}{(2\pi)^3} \frac{F(\rho_{01},\omega_0)F(\rho_{02},\omega_0)}{\sqrt{\rho_{0t}'\rho_{0s}[\rho_{0s}^2-(\frac{\rho}{2})^2]}} \\
& \cdot e^{jk_0\Delta\rho_s} \sum_{\vec{K}_2,\omega_2} e^{j\omega_2 t}\, {}_1P_{\vec{K}_2,\omega_2} e^{j\vec{K}_2\cdot\vec{\rho}_{0t}} e^{j\vec{K}_2\cdot\delta\vec{\rho}_t(t)} \\
& \cdot \int_K K\sqrt{\cos\phi_0}\, e^{j\rho_{0s}K\cos\phi_0} \Delta\rho_s \mathrm{Sa}\left[\frac{\Delta\rho_s}{2}\left(\frac{K}{\cos\phi_0}-2k_0\right)\right] \\
& \cdot \Xi_{t0}(\vec{K}-\vec{K}_2)\, {}_E\Gamma_P(\vec{K}-\vec{K}_2,\vec{K}_2) e^{-j\vec{K}\cdot\delta\vec{\rho}_t(t)} e^{-jK\rho_{0t}'} dK \quad .
\end{aligned}
\tag{2.38}
$$

As in the previous two sections, the radar pulse width will be assumed sufficiently long so that the sampling function in (2.38) may be replaced with a Dirac delta function according to (2.15). Completing the K integral under this condition gives

$$
\begin{aligned}
\left(E_{0n}^{+}\right)_{2to}(t_0,t) \approx & \frac{-j2\eta_0 \Delta l I_0 k_0^3}{(2\pi)^2} \frac{F(\rho_{01},\omega_0)F(\rho_{02},\omega_0)}{\sqrt{\rho_{0t}'\rho_{0s}[\rho_{0s}^2-(\frac{\rho}{2})^2]}} \cos^{5/2}\phi_0 \\
& \cdot e^{jk_0\Delta\rho_s}\phi_0 e^{j\rho_{0s}K\cos\phi_0} e^{-j\vec{K}\cdot\delta\vec{\rho}_t(t)} e^{-jK\rho_{0t}'} \\
& \cdot \sum_{\vec{K}_2,\omega_2} e^{j\omega_2 t}\, {}_1P_{\vec{K}_2,\omega_2} e^{j\vec{K}_2\cdot\vec{\rho}_{0t}} e^{j\vec{K}_2\cdot\delta\vec{\rho}_t(t)} \Xi_{t0}(\vec{K}-\vec{K}_2)\, {}_E\Gamma_P(\vec{K}-\vec{K}_2,\vec{K}_2) \quad ,
\end{aligned}
\tag{2.39}
$$

where $K = 2k_0\cos\phi_0$. Again, as was assumed for both first- and second-order electric field expressions, the distance, ρ_{0t}', is taken to be approximately equal to the radius of curvature, ρ_{0c}, at the scattering point, (x_{01}, y_{01}). This yields

$$
\begin{aligned}
\left(E_{0n}^{+}\right)_{2to}(t_0,t) \approx & \frac{-j2\eta_0 \Delta l I_0 k_0^3}{(2\pi)^2} \frac{F(\rho_{01},\omega_0)F(\rho_{02},\omega_0)}{\rho_{01}\rho_{02}} \cos^{2}\phi_0 \\
& \cdot e^{jk_0\Delta\rho_s} e^{j\rho_{0s}K\cos\phi_0} e^{-j\vec{K}\cdot\delta\vec{\rho}_t(t)} e^{-jK\rho_{0c}} \\
& \cdot \sum_{\vec{K}_2,\omega_2} e^{j\omega_2 t}\, {}_1P_{\vec{K}_2,\omega_2} e^{j\vec{K}_2\cdot\vec{\rho}_{0t}} e^{j\vec{K}_2\cdot\delta\vec{\rho}_t(t)} \Xi_{t0}(\vec{K}-\vec{K}_2)\, {}_E\Gamma_P(\vec{K}-\vec{K}_2,\vec{K}_2)\ ,
\end{aligned}
\tag{2.40}
$$

where the identity $\rho_{0s}^2 - (\frac{\rho}{2})^2 = \rho_{01}\rho_{02}\cos^2\phi_0$ has been used.

The expression derived in (2.40) describes the scattered electric field that results from a secondary scatter from the ocean surface following an initial scatter from the deterministic target. Intuitively, it follows that the converse scenario should be accounted for. If the transformation described in (2.21) is now applied to only the second scattering point in (2.20), and an identical process to that resulting in (2.40) is conducted, by symmetry the second-order field for ocean-target scatter, $(E_{0n}^{+})_{2ot}$, can be immediately written as

$$
\begin{aligned}
\left(E_{0n}^{+}\right)_{2ot}(t_0,t) \approx\ & \frac{-j2\eta_0 \Delta l I_0 k_0^3}{(2\pi)^2} \frac{F(\rho_{01},\omega_0)F(\rho_{02},\omega_0)}{\rho_{01}\rho_{02}} \cos^2\phi_0 \\
& \cdot e^{jk_0\Delta\rho_s} e^{j\rho_{0s}K\cos\phi_0} e^{-j\vec{K}\cdot\delta\vec{\rho}_t(t)} e^{-jK\rho_{0c}} \\
& \cdot \sum_{\vec{K}_1,\omega_1} e^{j\omega_1 t}\, {}_1P_{\vec{K}_1,\omega_1} e^{j\vec{K}_1\cdot\vec{\rho}_{0t}} e^{j\vec{K}_1\cdot\delta\vec{\rho}_t(t)} \Xi_{t0}(\vec{K}-\vec{K}_1)\, {}_E\Gamma_P(\vec{K}_1,\vec{K}-\vec{K}_1)\ .
\end{aligned}
\tag{2.41}
$$

On recognizing that the summations in (2.40) and (2.41) are over all surface wavenumbers, a combined ocean-target, target-ocean scattered electric field may be written as

$$
\begin{aligned}
\left(E_{0n}^{+}\right)_{2to+ot}(t_0,t) \approx\ & \frac{-j2\eta_0 \Delta l I_0 k_0^3}{(2\pi)^2} \frac{F(\rho_{01},\omega_0)F(\rho_{02},\omega_0)}{\rho_{01}\rho_{02}} \cos^2\phi_0 \\
& \cdot e^{jk_0\Delta\rho_s} e^{j\rho_{0s}K\cos\phi_0} e^{-j\vec{K}\cdot\delta\vec{\rho}_t(t)} e^{-jK\rho_{0c}} \\
& \cdot \Bigg[\sum_{\vec{K}_2,\omega_2} e^{j\omega_2 t}\, {}_1P_{\vec{K}_2,\omega_2} e^{j\vec{K}_2\cdot\vec{\rho}_{0t}} e^{j\vec{K}_2\cdot\delta\vec{\rho}_t(t)} \Xi_{t0}(\vec{K}-\vec{K}_2)\, {}_E\Gamma_P(\vec{K}-\vec{K}_2,\vec{K}_2) \\
& + \sum_{\vec{K}_1,\omega_1} e^{j\omega_1 t}\, {}_1P_{\vec{K}_1,\omega_1} e^{j\vec{K}_1\cdot\vec{\rho}_{0t}} e^{j\vec{K}_1\cdot\delta\vec{\rho}_t(t)} \Xi_{t0}(\vec{K}-\vec{K}_1)\, {}_E\Gamma_P(\vec{K}_1,\vec{K}-\vec{K}_1) \Bigg] \\
\approx\ & \frac{-j2\eta_0 \Delta l I_0 k_0^3}{(2\pi)^2} \frac{F(\rho_{01},\omega_0)F(\rho_{02},\omega_0)}{\rho_{01}\rho_{02}} \cos^2\phi_0 \\
& \cdot e^{jk_0\Delta\rho_s} e^{j\rho_{0s}K\cos\phi_0} e^{-j\vec{K}\cdot\delta\vec{\rho}_t(t)} e^{-jK\rho_{0c}} \\
& \cdot \sum_{\vec{K}_2,\omega_2} e^{j\omega_2 t}\, {}_1P_{\vec{K}_2,\omega_2} e^{j\vec{K}_2\cdot\vec{\rho}_{0t}} e^{j\vec{K}_2\cdot\delta\vec{\rho}_t(t)} \Xi_{t0}(\vec{K}-\vec{K}_2) \\
& \cdot \left[{}_E\Gamma_P(\vec{K}-\vec{K}_2,\vec{K}_2) + {}_E\Gamma_P(\vec{K}_2,\vec{K}-\vec{K}_2) \right]\ .
\end{aligned}
\tag{2.42}
$$

Using (2.30), (2.42) may be rewritten as

$$
\begin{aligned}
\left(E_{0n}^{+}\right)_{2to}(t_0,t) \approx \frac{-j4\eta_0 \Delta l I_0 k_0^3}{(2\pi)^2}\frac{F(\rho_{01},\omega_0)F(\rho_{02},\omega_0)}{\rho_{01}\rho_{02}}\cos^2\phi_0 \\
\cdot\, e^{jk_0\Delta\rho_s} e^{j\rho_{0s}K\cos\phi_0} e^{-j\vec{K}\cdot\delta\vec{\rho}_t(t)} e^{-jK\rho_{0c}} \\
\cdot \sum_{\vec{K}_2,\omega_2} e^{j\omega_2 t}\, {}_1P_{\vec{K}_2,\omega_2} e^{j\vec{K}_2\cdot\vec{\rho}_{0t}} e^{j\vec{K}_2\cdot\delta\vec{\rho}_t(t)} \Xi_{t0}(\vec{K}-\vec{K}_2)\, {}_{SE}\Gamma_P(\vec{K}-\vec{K}_2,\vec{K}_2)\ ,
\end{aligned}
\tag{2.43}
$$

where the original subscript $2to$ has been reused for compactness.

2.5 Summary

In this chapter, bistatic electric field expressions were derived for deterministic targets in motion on a surface described by a time-varying Fourier series. In deriving the expressions, a method originally presented by Walsh and Gill [21] and applied to non-moving monostatic radar targets was extended to permit arbitrary target motion and applied to bistatic expressions subsequently derived by the same authors. The electric field expressions were simplified through asymptotic methods and other approximations to forms suitable for finding power spectral densities. Obtaining the power spectral densities and corresponding radar cross sections associated with each of these expressions constitutes the objectives of the next chapter.

Chapter 3

Radar Cross Sections for Surface Targets in Motion on the Ocean Surface

3.1 Introduction

In the preceding chapter, electric field expressions were derived to second-order for a deterministic target in motion on a time-varying rough surface. The objective in this chapter is to obtain the corresponding RCS models by considering the total scattered electric field from an ocean patch containing a surface target. The target velocity will remain arbitrary to allow it to be specified in a variety of future applications. In evaluating the various operations performed in deriving RCS models, relevant stochastic properties typically used in studying HF scattering from the ocean surface will be employed.

The process to obtain the RCS models will follow the general method that has been used by previous authors studying scattering from the ocean surface [18, 33]. The PSD of the scattered electric field at the receiver will be found and compared with a bistatic form of the radar equation. To accomplish this, the corresponding autocorrelation function must first be derived. The PSD is then found through a Fourier transform. To validate the results of this chapter, the bistatic moving target cross sections will be shown to reduce to that of monostatic, fixed target RCSs found in previous work [21].

3.2 Power Spectral Densities of the Received Electric Field

The process for deriving the received spectral densities begins with finding the autocorrelation function of the scattered electric field. A convenient form of the autocorrelation function was defined in Chapter 1 and is repeated here as

$$\mathcal{R}(\tau) = \frac{A_r}{2\eta_0} < E_{0_n}^{+}(t_0, t+\tau) E_{0_n}^{+*}(t_0, t) > \quad , \tag{3.1}$$

where A_r is the effective aperture of the receiving antenna and $E_{0_n}^{+}$ is the total vertically polarized electric field measured at the receiver. This work considers the scattered electric field from a deterministic target as well as the surrounding surface. If it is agreed to limit the analysis to second-order effects, the total electric field should include the first- and second-order contributions from a target only, (2.16) and (2.33), the first- and second-order components from the surrounding ocean, (1.44) and (1.56), as well as the second-order target-ocean scatter derived in Section 2.4. This may be written explicitly as

$$\begin{aligned}(E_{0_n})^+(t_0,t) &= \left(E_{0n}^+\right)_{1t}(t_0,t) + \left(E_{0n}^+\right)_{2t}(t_0,t)\\ &\quad + \left(E_{0_n}^+\right)_{11}(t_0,t) + \left(E_{0n}^+\right)_{2p}(t_0,t) + \left(E_{0n}^+\right)_{2to}(t_0,t)\\ &= \left(E_{0n}^+\right)_{t}(t_0,t) + \left(E_{0_n}^+\right)_{11}(t_0,t) + \left(E_{0n}^+\right)_{2p}(t_0,t) + \left(E_{0n}^+\right)_{2to}(t_0,t)\ ,\end{aligned} \tag{3.2}$$

where the second equality results from summing the two components involving only target scatter to

$$\left(E_{0n}^+\right)_{t}(t_0,t) = \left(E_{0n}^+\right)_{1t}(t_0,t) + \left(E_{0n}^+\right)_{2t}(t_0,t) \quad . \tag{3.3}$$

The total autocorrelation function of the received electric field is then found by applying (3.1) to (3.2). Formally, this is

$$\begin{aligned}\mathcal{R}(\tau) = \frac{A_r}{2\eta_0}\Big\langle\Big[&\left(E_{0n}^+\right)_{t}(t_0,t+\tau) + \left(E_{0_n}^+\right)_{11}(t_0,t+\tau) + \left(E_{0n}^+\right)_{2p}(t_0,t+\tau)\\ &+ \left(E_{0n}^+\right)_{2to}(t_0,t)\Big]\cdot\Big[\left(E_{0n}^+\right)^*_{t}(t_0,t) + \left(E_{0_n}^+\right)^*_{11}(t_0,t) + \left(E_{0n}^+\right)^*_{2p}(t_0,t)\\ &+ \left(E_{0n}^+\right)^*_{2to}(t_0,t)\Big]\Big\rangle,\end{aligned} \tag{3.4}$$

and may be expanded as the sum of sixteen ensemble averages containing both auto- and cross-correlations i.e.

$$
\begin{aligned}
\mathcal{R}(\tau) = \frac{A_r}{2\eta_0} \Big\{ & \left\langle \left(E_{0n}^{+}\right)_t (t_0, t+\tau) \left(E_{0n}^{+}\right)_t^* (t_0, t) \right\rangle \\
& + \left\langle \left(E_{0n}^{+}\right)_t (t_0, t+\tau) \left(E_{0_n}^{+}\right)_{11}^* (t_0, t) \right\rangle ... \\
& + \left\langle \left(E_{0_n}^{+}\right)_{11} (t_0, t+\tau) \left(E_{0n}^{+}\right)_t^* (t_0, t) \right\rangle + \left\langle \left(E_{0_n}^{+}\right)_{11} (t_0, t+\tau) \left(E_{0_n}^{+}\right)_{11}^* (t_0, t) \right\rangle ... \\
& + \left\langle \left(E_{0n}^{+}\right)_{2p} (t_0, t+\tau) \left(E_{0n}^{+}\right)_t^* (t_0, t) \right\rangle + \left\langle \left(E_{0n}^{+}\right)_{2p} (t_0, t+\tau) \left(E_{0_n}^{+}\right)_{11}^* (t_0, t) \right\rangle ... \\
& + \left\langle \left(E_{0n}^{+}\right)_{2to} (t_0, t) \left(E_{0n}^{+}\right)_t^* (t_0, t) \right\rangle + \left\langle \left(E_{0n}^{+}\right)_{2to} (t_0, t) \left(E_{0_n}^{+}\right)_{11}^* (t_0, t) \right\rangle ... \Big\}.
\end{aligned} \tag{3.5}
$$

Before finding expressions for the important terms in (3.5), it is shown that a number of terms can be eliminated. A similar expression for the autocorrelation of the received signal from the ocean surface only is found in Chapter 3 of Gill's doctoral thesis [9]. There it was found that all cross-correlations involving ocean scatters only (e.g. $< (E_{0n}^{+})_{2p}(t_0, t+\tau)(E_{0_n}^{+})_{11}^*(t_0, t) >$) evaluated to zero. Next, the cross-correlation $< (E_{0n}^{+})_t(t_0, t+\tau)(E_{0_n}^{+})_{11}^*(t_0, t) >$, is considered, i.e.

$$
\begin{aligned}
& \left\langle \left(E_{0n}^{+}\right)_t (t_0, t+\tau) \left(E_{0_n}^{+}\right)_{11}^* (t_0, t) \right\rangle = \Bigg\langle \frac{2\eta_0^2 |\Delta l I_0|^2 k_0^5}{(2\pi)^{\frac{7}{2}}} \frac{F(\rho_{01}, \omega_0) F(\rho_{02}, \omega_0)}{\rho_{01}\rho_{02}} \cos^2 \phi_0 \\
& \cdot \mathcal{P}_0(2k_0 \cos\phi_0 \hat{N}) e^{j\rho_{0s} K \cos\phi_0} e^{-j\vec{K}\cdot\delta\vec{\rho}_t(t+\tau)} e^{-jK\rho_{0c}} e^{j\frac{\pi}{4}} \frac{F^*(\rho_{01}', \omega_0) F^*(\rho_{02}', \omega_0)}{\sqrt{\rho_{0s}' [\rho_{0s}'^2 - (\frac{\rho}{2})^2]}} \\
& \cdot \sum_{\vec{K}', \omega'} {}_1P_{\vec{K}', \omega'}^* \sqrt{K' \cos\phi_0} e^{-j\frac{\vec{\rho}}{2}\cdot\vec{K}'} e^{-j\omega t} e^{-j\rho_{0s} K' \cos\phi_0} \Delta\rho_s \mathrm{Sa}\left[\frac{\Delta\rho_s}{2} \left(\frac{K'}{\cos\phi_0} - 2k_0 \right) \right] \Bigg\rangle \quad .
\end{aligned} \tag{3.6}
$$

If the target velocity and the ocean surface displacement are assumed uncorrelated, this becomes

$$\left\langle \left(E_{0n}^{+}\right)_t (t_0, t+\tau) \left(E_{0_n}^{+}\right)_{11}^{*} (t_0, t) \right\rangle = \frac{2\eta_0^2 |\Delta l I_0|^2 k_0^5}{(2\pi)^{\frac{7}{2}}} \frac{F(\rho_{01}, \omega_0) F(\rho_{02}, \omega_0)}{\rho_{01}\rho_{02}} \mathcal{P}_0(2k_0 \cos\phi_0 \hat{N})$$
$$\cdot\, e^{j\rho_{0s} K \cos\phi_0} e^{-jK\rho_{0c}} e^{j\frac{\pi}{4}} \left\langle e^{-j\vec{K}\cdot\delta\vec{\rho}_t(t+\tau)} \right\rangle \frac{F^*(\rho_{01}', \omega_0) F^*(\rho_{02}', \omega_0)}{\sqrt{\rho_{0s}'[\rho_{0s}'^2 - (\frac{\rho}{2})^2]}}$$
$$\cdot \sum_{\vec{K}', \omega'} \left\langle {}_1P_{\vec{K}', \omega'}^{*} \right\rangle \sqrt{K' \cos\phi_0}\, e^{-j\frac{\vec{\rho}}{2}\cdot\vec{K}'} e^{-j\omega t} e^{-j\rho_{0s} K' \cos\phi_0} \Delta\rho_s \mathrm{Sa}\left[\frac{\Delta\rho_s}{2}\left(\frac{K'}{\cos\phi_0} - 2k_0\right)\right] \quad , \tag{3.7}$$

which evaluates to zero as

$$\left\langle {}_1P_{\vec{K}', \omega'}^{*} \right\rangle = 0 \tag{3.8}$$

for the zero-mean first-order ocean surface. The same result occurs for any cross-correlation containing only a single rough surface component; thus, any cross correlation between a target field component and either first-order ocean, or target-ocean scattered field will evaluate to zero. Similarly, any cross-correlation containing $\left(E_{0n}^{+}\right)_{2to} (t_0, t)$ and a second-order ocean component will include an odd number of Fourier components as factors, with an ensemble average that evaluates to zero as noted in [9]. Lastly, the cross-correlation containing the target-only electric field and a second-order scatter from the ocean is considered. One such term is $< (E_{0n}^{+})_t (t_0, t+\tau) (E_{0n}^{+})_{2P}^{*} (t_0, t) >$ which may be expressed as

$$
\begin{aligned}
\left\langle \left(E_{0n}^{+}\right)_t (t_0, t+\tau) \left(E_{0n}^{+}\right)_{2P} (t_0, t) \right\rangle = \Bigg\langle & \frac{2\eta_0^2 |\Delta l I_0|^2 k_0^5}{(2\pi)^{\frac{7}{2}}} \frac{F(\rho_{01}, \omega_0) F(\rho_{02}, \omega_0)}{\rho_{01}\rho_{02}} \cos^2 \phi_0 \\
& \cdot \mathcal{P}_0(2k_0 \cos\phi_0 \hat{N}) e^{j\rho_{0s} K \cos\phi_0} e^{-j\vec{K}\cdot\delta\vec{\rho}_t(t)} e^{-jK\rho_{0c}} \frac{F^*(\rho'_{01}, \omega_0) F^*(\rho'_{02}, \omega_0)}{\sqrt{\rho'_{0s}[\rho'^2_{0s} - (\frac{\rho}{2})^2]}} \\
& \sum_{\vec{K}'_1, \omega'_1} \sum_{\vec{K}'_2, \omega'_2} {}_1P^*_{\vec{K}'_1, \omega'_1} \, {}_1P^*_{\vec{K}'_2, \omega'_2} e^{-j(\omega'_1 + \omega'_2)t} \sqrt{K' \cos\phi_0} \Gamma^*_P(\vec{K}'_1, \vec{K}'_2) \\
& \cdot e^{j\frac{\pi}{4}} e^{-j\frac{\vec{\rho}}{2}\cdot\vec{K}'} e^{-j\rho'_{0s} K' \cos\phi_0} \Delta\rho_s \mathrm{Sa}\left[\frac{\Delta\rho_s}{2}\left(\frac{K'}{\cos\phi_0} - 2k_0\right)\right] \Bigg\rangle \quad ,
\end{aligned}
\tag{3.9}
$$

and reduces to

$$
\begin{aligned}
\left\langle \left(E_{0n}^{+}\right)_t (t_0, t+\tau) \left(E_{0n}^{+}\right)_{2P} (t_0, t) \right\rangle = & \frac{2\eta_0^2 |\Delta l I_0|^2 k_0^5}{(2\pi)^{\frac{7}{2}}} \frac{F(\rho_{01}, \omega_0) F(\rho_{02}, \omega_0)}{\rho_{01}\rho_{02}} \cos^2 \phi_0 \\
& \cdot \mathcal{P}_0(2k_0 \cos\phi_0 \hat{N}) e^{j\rho_{0s} K \cos\phi_0} \left\langle e^{-j\vec{K}\cdot\delta\vec{\rho}_t(t)} \right\rangle e^{-jK\rho_{0c}} \frac{F^*(\rho'_{01}, \omega_0) F^*(\rho'_{02}, \omega_0)}{\sqrt{\rho'_{0s}[\rho'^2_{0s} - (\frac{\rho}{2})^2]}} \\
& \sum_{\vec{K}'_1, \omega'_1} \sum_{\vec{K}'_2, \omega'_2} \left\langle {}_1P^*_{\vec{K}'_1, \omega'_1} \, {}_1P^*_{\vec{K}'_2, \omega'_2} \right\rangle e^{-j(\omega'_1 + \omega'_2)t} \sqrt{K' \cos\phi_0} \Gamma^*_P(\vec{K}'_1, \vec{K}'_2) \\
& \cdot e^{j\frac{\pi}{4}} e^{-j\frac{\vec{\rho}}{2}\cdot\vec{K}'} e^{-j\rho'_{0s} K' \cos\phi'_0} \Delta\rho_s \mathrm{Sa}\left[\frac{\Delta\rho_s}{2}\left(\frac{K'}{\cos\phi'_0} - 2k_0\right)\right] \quad ,
\end{aligned}
\tag{3.10}
$$

if the ocean surface displacement and target velocity are uncorrelated. Using (1.35) and (1.36) it is permissible to write

$$
\left\langle {}_1P^*_{\vec{K}'_1, \omega'_1} \, {}_1P^*_{\vec{K}'_2, \omega'_2} \right\rangle = \begin{cases} S_1(\vec{K}'_1, \omega'_1) d\vec{K} d\omega, & \vec{K}'_1 = -\vec{K}'_2 \ , \ \omega'_1 = -\omega'_2 \\ 0, & \text{otherwise} \quad . \end{cases}
\tag{3.11}
$$

In deriving the second-order patch scattered field, it was noted that $\vec{K} = \vec{K}_1 + \vec{K}_2$. The constraints on (3.11) require $\vec{K}_1 + \vec{K}_2 = \vec{0}$. On noting that the sampling function in (3.10) is negligible for $K = 0$, and exactly zero if the long pulse assumption (2.15) is employed, the cross-correlation $< (E_{0n}^{+})_t(t_0, t+\tau)(E_{0n}^{+})_{2P}^{*}(t_0, t) >$ may be eliminated. In exactly the same manner, the cross-correlation $< (E_{0n}^{+})_{2P}(t_0, t+\tau)(E_{0n}^{+})_{t}^{*}(t_0, t) >$ may also be neglected.

From the analyses given in this section, and the arguments presented in Chapter 3 and Appendix B of [9], all cross-correlation components of (3.5) may be neglected and the total autocorrelation function for the received electric field can be expressed

$$\begin{aligned}
\mathcal{R}(\tau) = \frac{A_r}{2\eta_0}\Big\{ & \left\langle \left(E_{0n}^{+}\right)_t (t_0, t+\tau) \left(E_{0n}^{+}\right)_t^{*} (t_0, t)\right\rangle + \left\langle \left(E_{0_n}^{+}\right)_{11} (t_0, t+\tau) \left(E_{0_n}^{+}\right)_{11}^{*} (t_0, t)\right\rangle \\
& + \left\langle \left(E_{0n}^{+}\right)_{2P} (t_0, t+\tau) \left(E_{0n}^{+}\right)_{2P}^{*} (t_0, t)\right\rangle + \left\langle \left(E_{0n}^{+}\right)_{2to} (t_0, t) \left(E_{0n}^{+}\right)_{to}^{*} (t_0, t)\right\rangle \Big\}. \\
& = \mathcal{R}_t(\tau) + \mathcal{R}_{11}(\tau) + \mathcal{R}_{2P}(\tau) + \mathcal{R}_{to}(\tau) \quad .
\end{aligned} \tag{3.12}$$

where the subscript on the terms defined in the last equality corresponds to the appropriate electric field component on which the autocorrelation operation must be performed. The Doppler power spectral density, $\mathcal{P}_d(\omega_d)$, of the received electric field is found as the Fourier transform of (3.12). As the Fourier transform is a linear operator, the Doppler power spectral density can be expressed as

$$\begin{aligned}
\mathcal{P}_d(\omega_d) &= \mathcal{F}\left[\mathcal{R}(\tau)\right] \\
&= \mathcal{F}\left[\mathcal{R}_t(\tau)\right] + \mathcal{F}\left[\mathcal{R}_{11}(\tau)\right] + \mathcal{F}\left[\mathcal{R}_{2P}(\tau)\right] + \mathcal{F}\left[\mathcal{R}_{to}(\tau)\right] \\
&= \mathcal{P}_t(\omega_d) + \mathcal{P}_{11}(\tau) + \mathcal{P}_{2P}(\tau) + \mathcal{P}_{to}(\tau) \quad .
\end{aligned} \tag{3.13}$$

and each term may be evaluated separately to form a total composite RCS for the return from an ocean patch containing a surface target as

$$\sigma(\omega_d) = \sigma_t(\omega_d) + \sigma_{11}(\tau) + \sigma_{2P}(\tau) + \sigma_{to}(\tau) \quad . \tag{3.14}$$

Expressions for the terms related to ocean scatter only, $\sigma_{11}(\tau)$ and $\sigma_{2P}(\tau)$, are presented in [18] with additional details contained in [9]. Thus, attention is now directed towards finding the power spectral densities involving target scatter, $\mathcal{P}_t(\omega_d)$ and $\mathcal{P}_{to}(\omega_d)$, and their corresponding cross section models.

3.2.1 Target Scatter Power Spectral Density

From (3.12), and applying (3.1) to (2.34), the autocorrelation function of the combined first- and second-order scattered field from a surface target is

$$\begin{aligned}\mathcal{R}_t(\tau) &= \frac{A_r}{2\eta_0}\left\langle \left(E_{0n}^{+}\right)_t (t_0, t+\tau) \left(E_{0n}^{+}\right)_t^* (t_0, t)\right\rangle \\ &= \frac{2A_r\eta_0|\Delta l I_0|^2 k_0^6}{(2\pi)^4}\frac{F(\rho_{01},\omega_0)F(\rho_{02},\omega_0)}{\rho_{01}\rho_{02}}\frac{F^*(\rho_{01}',\omega_0)F^*(\rho_{02}',\omega_0)}{\rho_{01}'\rho_{02}'} \\ &\cdot \left\langle e^{-j\vec{K}\cdot\delta\vec{\rho}_t(t+\tau)} e^{j\vec{K}'\cdot\delta\vec{\rho}_t(t)}\right\rangle e^{-jK\rho_{0c}} e^{jK'\rho_{0c}'} \\ &\cdot \cos^2\phi_0'\cos^2\phi_0\mathcal{P}_0^*(2k_0\cos\phi_0\hat{N}')\mathcal{P}_0(2k_0\cos\phi_0\hat{N}) \quad .\end{aligned} \tag{3.15}$$

This expression can be greatly simplified if a narrow beam receiver is assumed such that the nominal geometry of the scattering point or ‘patch’ is fixed between measurements. In this case, the primed quantities in (3.15) are equal to their unprimed equivalents. The result is

$$
\begin{aligned}
\mathcal{R}_t(\tau) =& \frac{2A_r\eta_0|\Delta l I_0|^2 k_0^6}{(2\pi)^8}\frac{|F(\rho_{01},\omega_0)F(\rho_{02},\omega_0)|^2}{\rho_{01}^2\rho_{02}^2} \\
&\cdot \cos^4\phi_0|\mathcal{P}_0(2k_0\cos\phi_0\hat{N})|^2\left\langle M_t(\vec{K},\tau,t)\right\rangle ,
\end{aligned}
\tag{3.16}
$$

where M_t has been defined as

$$
M_t(\vec{K},\tau,t) = e^{-j\vec{K}\cdot\delta\vec{\rho}_t(t+\tau)}e^{j\vec{K}\cdot\delta\vec{\rho}_t(t)} \quad . \tag{3.17}
$$

This expression may be recognized as the phase difference in the received electric field between successive radar acquisitions due to a small displacement of the target. Similar expressions are derived in previous work addressing HF radars installed on moving platforms [42, 44] where the phase contribution is associated with a small displacement of the transmitting source.

The power spectral density of the scattered field from a surface target only is found by taking the Fourier transform of its autocorrelation function with respect to the delay variable τ. Performing this operation on (3.16) yields

$$
\begin{aligned}
\mathcal{P}_t(\omega_d) =& \frac{2A_r\eta_0|\Delta l I_0|^2 k_0^6}{(2\pi)^4}\frac{F(\rho_{01},\omega_0)F(\rho_{02},\omega_0)^2}{\rho_{01}^2\rho_{02}^2}\cos^4\phi_0|\mathcal{P}_0(2k_0\cos\phi_0\hat{N})|^2 \\
&\cdot \mathcal{F}\left[\left\langle M_t(2k_0\cos\phi_0\hat{N},\tau,t)\right\rangle\right] \quad ,
\end{aligned}
\tag{3.18}
$$

where the stationary, long-pulse value of $\vec{K} = 2k_0\cos\phi_0\hat{N}$ has been substituted into the argument of M_t.

3.2.2 Target-Ocean Scatter Power Spectral Density

The autocorrelation of the target-ocean scattered electric field, $\mathcal{R}_{to}(\tau)$, is found by applying (3.1) to (2.43). The result is

$$\mathcal{R}_{to}(\tau) = \frac{8A_r\eta_0|\Delta l I_0|^2 k_0^6}{(2\pi)^4} \frac{F(\rho_{01},\omega_0)F(\rho_{02},\omega_0)}{\rho_{01}\rho_{02}} \frac{F^*(\rho'_{01},\omega_0)F^*(\rho'_{02},\omega_0)}{\rho'_{01}\rho'_{02}} \cos^2\phi'_0 \cos^2\phi_0$$
$$e^{j\rho_{0s}K\cos\phi_0} e^{-j\rho'_{0s}K'\cos\phi'_0} e^{-jK\rho_{0c}} e^{jK'\rho'_{0c}}$$
$$\cdot \sum_{\vec{K}_2,\omega_2} \sum_{\vec{K}'_2,\omega'_2} e^{j\omega_2(t+\tau)} e^{-j\omega'_2 t} \left\langle {}_1P_{\vec{K}_2,\omega_2}\, {}_1P^*_{\vec{K}'_2,\omega'_2} \right\rangle e^{j\vec{K}_2\cdot\vec{\rho}_{0t}} e^{-j\vec{K}'_2\cdot\vec{\rho}_{0t}}$$
$$\cdot\, \Xi_{t0}(\vec{K}-\vec{K}_2)\Xi^*_{t0}(\vec{K}'-\vec{K}'_2)\, {}_{SE}\Gamma_P(\vec{K}-\vec{K}_2,\vec{K}_2)\, {}_{SE}\Gamma^*_P(\vec{K}'-\vec{K}'_2,\vec{K}'_2)$$
$$\left\langle e^{-j\vec{K}\cdot\delta\vec{\rho}_t(t+\tau)} e^{j\vec{K}'\cdot\delta\vec{\rho}_t(t)} e^{j\vec{K}_2\cdot\delta\vec{\rho}_t(t+\tau)} e^{-j\vec{K}'_2\cdot\delta\vec{\rho}_t(t)} \right\rangle \quad . \tag{3.19}$$

In distributing the ensemble average operator, <>, to the exponentials related to the target motion and the Fourier series coefficients separately, it has been implicitly assumed that the target velocity is independent of the ocean surface displacement. Invoking (1.35), equation (3.19) reduces to

$$\mathcal{R}_{to}(\tau) = \frac{8A_r\eta_0|\Delta l I_0|^2 k_0^6}{(2\pi)^4} \frac{F(\rho_{01},\omega_0)F(\rho_{02},\omega_0)}{\rho_{01}\rho_{02}} \frac{F^*(\rho'_{01},\omega_0)F^*(\rho'_{02},\omega_0)}{\rho'_{01}\rho'_{02}} \cos^2\phi'_0 \cos^2\phi_0$$
$$e^{j\rho_{0s}K\cos\phi_0} e^{-j\rho'_{0s}K'\cos\phi'_0} e^{-jK\rho_{0c}} e^{jK'\rho'_{0c}}$$
$$\cdot \int_{\vec{K}_2}\int_{\omega_2} e^{j\omega_2\tau} S_1(\vec{K}_2,\omega_2)$$
$$\cdot\, \Xi_{t0}(\vec{K}-\vec{K}_2)\Xi^*_{t0}(\vec{K}'-\vec{K}_2)\, {}_{SE}\Gamma_P(\vec{K}-\vec{K}_2,\vec{K}_2)\, {}_{SE}\Gamma^*_P(\vec{K}'-\vec{K}_2,\vec{K}_2)$$
$$\left\langle e^{-j\vec{K}\cdot\delta\vec{\rho}_t(t+\tau)} e^{j\vec{K}'\cdot\delta\vec{\rho}_t(t)} e^{j\vec{K}_2\cdot\delta\vec{\rho}_t(t+\tau)} e^{-j\vec{K}'_2\cdot\delta\vec{\rho}_t(t)} \right\rangle d\vec{K}_2 d\omega_2 \quad . \tag{3.20}$$

Imposing a narrow beam receiver assumption as was done in the previous section, (3.20) can also be simplified to

$$\begin{aligned}\mathcal{R}_{to}(\tau) =& \frac{8A_r\eta_0|\Delta l I_0|^2k_0^6}{(2\pi)^4}\frac{|F(\rho_{01},\omega_0)F(\rho_{02},\omega_0)|^2}{\rho_{01}^2\rho_{02}^2}\cos^4\phi_0 \\ &\cdot \int_{\vec{K}_2}\int_{\omega_2} e^{j\omega_2\tau}S_1(\vec{K}_2,\omega_2)|\Xi_{t0}(\vec{K}-\vec{K}_2)|^2|_{SE}\Gamma_P(\vec{K}-\vec{K}_2,\vec{K}_2)|^2 \\ &\cdot \left\langle M_{to}(\vec{K},\vec{K}_2,t,\tau)\right\rangle d\vec{K}_2 d\omega_2 \quad .\end{aligned} \tag{3.21}$$

where

$$M_{to} = e^{-j\vec{K}\cdot[\delta\vec{\rho}_t(t+\tau)-\delta\vec{\rho}_t(t)]}e^{j\vec{K}_2\cdot\delta[\vec{\rho}_t(t+\tau)-\delta\vec{\rho}_t(t)]} \quad . \tag{3.22}$$

The corresponding power spectral density is easily found as the Fourier transform with respect to τ of (3.21). The result may be written directly as

$$\begin{aligned}\mathcal{P}_{to}(\omega_d) =& \frac{8A_r\eta_0|\Delta l I_0|^2k_0^6}{(2\pi)^4}\frac{|F(\rho_{01},\omega_0)F(\rho_{02},\omega_0)|^2}{\rho_{01}^2\rho_{02}^2}\cos^4\phi_0 \\ &\cdot \int_{\vec{K}_2}\int_{\omega_2} S_1(\vec{K}_2,\omega_2)|\Xi_{t0}(\vec{K}-\vec{K}_2)|^2|_{SE}\Gamma_P(\vec{K}-\vec{K}_2,\vec{K}_2)|^2 \\ &\cdot \mathcal{F}\left[e^{j\omega_2\tau}\left\langle M_{to}(\vec{K},\vec{K}_2,t,\tau)\right\rangle\right] d\vec{K}_2 d\omega_2 \quad .\end{aligned} \tag{3.23}$$

3.3 Radar Cross Section Models: General Form

Radar cross section models corresponding to the power spectral densities derived in the previous section may be found with the aid of the bistatic radar range equation. In [18], Gill and Walsh present a convenient form of a modified radar equation incorporating the Sommerfeld attenuation functions. In that work, the incremental received power spectral density from a differential area is expressed as a function of radar parameters and a per-unit area radar cross section. Here, this expression is re-used with a conventional radar cross section in place of the per-unit area cross section with the understanding that output of the function is now a typical received power spectral density from a finite area. Thus, the bistatic radar equation used in this chapter is

$$\mathcal{P}(\omega_d) = \frac{A_r \eta_0 k_0^2 |I_0 \Delta l|^2 |F(\rho_{01}, \omega_0) F(\rho_{02}, \omega_0)|^2}{16(2\pi)^3 (\rho_{01}\rho_{02})^2} \sigma(\omega_d) \quad , \tag{3.24}$$

where $\sigma(\omega_d)$ is a radar cross section evaluated at a Doppler frequency of ω_d.

3.3.1 Target-Only Radar Cross Section

The bistatic RCS of a surface target is found by comparing the received power spectral density of the electric field scattered by a target, (3.18), with the form of the radar equation given in (3.24). The result, including first- and second-order scatters exclusively from the target is

$$\sigma_t(\omega_d) = \frac{16k_0^4}{\pi} \cos^4 \phi_0 |\mathcal{P}_0(2k_0 \cos\phi_0 \hat{N})|^2 \mathcal{F}\left[\left\langle M_t(2k_0 \cos\phi_0 \hat{N}, \tau, t)\right\rangle\right] \quad , \tag{3.25}$$

where $\mathcal{P}_0(2k_0 \cos\phi_0 \hat{N})$ is found using (2.35) as

$$\begin{aligned} \mathcal{P}_0(2k_0 \cos\phi_0 \hat{N}) =& \Xi_{t0}(2k_0 \cos\phi_0 \hat{N}) \\ &+ \frac{1}{(2\pi)^2} \int_{\vec{K}''} \Xi_{t0}\left(k_0 \cos\phi_0 \hat{N} + \vec{K}''\right) \Xi_{t0}\left(k_0 \cos\phi_0 \hat{N} - \vec{K}''\right) \\ &\cdot {}_{SE}\Gamma_P\left(k_0 \cos\phi_0 \hat{N} + \vec{K}'', k_0 \cos\phi_0 \hat{N} - \vec{K}''\right) d\vec{K}'' \ . \end{aligned} \tag{3.26}$$

This expression represents a new bistatic RCS model for a surface target with arbitrary motion.

The general bistatic target RCS described by (3.25) may be compared with the monostatic cross sections derived by Walsh and Gill [21] and discussed in Section 1.4.2. For convenience, the monostatic RCS model produced in that work is reproduced here:

$$\sigma = \left[\frac{16k_0^4}{\pi}|\mathcal{P}|^2\right] \quad , \tag{3.27}$$

with $\mathcal{P}$ defined as

$$\mathcal{P} = \Xi_{t0}(2k_0, \theta_1) + \frac{1}{2(2\pi)^2}\int_{\vec{K}} \Xi_{t0}(k_0\hat{\rho}_1 + \vec{K})\Xi_{t0}(k_0\hat{\rho}_1 - \vec{K})\frac{|\vec{K}\times\hat{\rho}_1|^2}{K^2 - k_0^2}d\vec{K}, \tag{3.28}$$

where $\hat{\rho}_1$ is a unit vector that points from the radar to the origin of the target profile or centre of the scattering patch and θ_1 is its associated angle. Comparing (3.25) and (3.26) with (3.27) and (3.28) the expressions are seen to be in general agreement, with the model derived in this work containing two additional factors that may be attributed separately to the bistatic geometry and target motion. The $\cos^4\phi_0$ in (3.25) may be shown to appear in the bistatic ocean cross section models derived by Gill [18] for an unbounded patch width, $\Delta\rho_s$. This is equivalent to the long pulse width assumption used in this work. The Fourier factor in (3.25) accounts for the Doppler shift associated with the target motion. It will be revisited and evaluated in the next chapter in an application considering a constant target velocity.

As a last comparison, it is straight forward to show that when considering only first-order scatters, (3.25) reduces to (3.27) for a monostatic radar and zero-velocity target. This is accomplished by first assigning a monostatic geometry such that

$$\phi_0 = 0 \text{ and } \hat{N} = \hat{\rho}_{01} \quad . \tag{3.29}$$

For a zero-velocity target, the Fourier transform of the motion-related factor evaluates as

$$\mathcal{F}\left[\left\langle M_t(2k_0 \cos\phi_0 \hat{N}, \tau, t)\right\rangle\right] = \mathcal{F}\left[1\right] = 2\pi\delta(\omega_d) \quad ; \tag{3.30}$$

however, the RCS given in (3.27) is not considered in the context of a Doppler spectrum. Thus, to compare the expressions, it is appropriate to set

$$\mathcal{F}\left[\left\langle M_t(2k_0 \cos\phi_0 \hat{N}, \tau, t)\right\rangle\right] = 1 \tag{3.31}$$

and omit the ω_d argument. Under these conditions, (3.25) evaluates to

$$\sigma_t = \frac{16k_0^4}{\pi}|\mathcal{P}_0(2k_0\hat{\rho}_{01})|^2 \quad . \tag{3.32}$$

If first-order scattering effects are exclusively considered, only the leading term of $\mathcal{P}_0$ (or $\mathcal{P}$ from (3.27)) need be retained, and the expressions agree exactly. If second-order target scattering effects are included, the full form of $\mathcal{P}_0(2k_0 \cos\phi_0 \hat{N})$ must be considered. Appendix C addresses this case and shows they are approximately equal, with the differences attributed to the refined analysis that produced the updated version of the electromagnetic coupling coefficient, ${}_E\Gamma_P$.

3.3.2 Target-Ocean Radar Cross Section

The second-order target-ocean RCS is found in equating the corresponding power spectral density, (3.23), with the received power spectral density predicted by the radar equation (3.24). The result is

$$\begin{aligned}\sigma_{to}(\omega_d) =& \frac{64k_0^4}{\pi}\cos^4\phi_0 \int_{\vec{K}_2}\int_{\omega_2} S_1(\vec{K}_2,\omega_2) \\ &\cdot |\Xi_{t0}(\vec{K}-\vec{K}_2)|^2 |{}_{SE}\Gamma_P(\vec{K}-\vec{K}_2,\vec{K}_2)|^2 \\ &\cdot \mathcal{F}\left[e^{j\omega_2\tau}\left\langle M_{to}(\vec{K},\vec{K}_2,t,\tau)\right\rangle\right] d\vec{K}_2 d\omega_2 \quad .\end{aligned} \tag{3.33}$$

This expression represents a new second-order RCS component that has not been investigated in the literature and thus has no previous results with which it may be directly compared. It may be noted however, if $|\Xi_{t0}(\vec{K}-\vec{K}_2)|^2$ is interpreted as a surface power spectral density, (3.33) takes the general form of a second-order RCS frequently seen in scattering from the ocean surface [12, 18]. In that manner, it is calculated as an integration over all ocean surface vector wavenumbers and radian frequencies. Additionally, it contains a Fourier factor within the integration that accounts for a Doppler shift involving both the target's displacement and the temporal frequency of the ocean surface.

3.4 Summary

In this chapter, two bistatic radar cross section components were obtained for a deterministic surface target on the ocean surface. This includes a cross section component involving first- and second-order scatters directly from the surface target, and an additional second-order component involving one scatter from the deterministic target and one scatter from the nearby ocean. In deriving the RCS components, the target motion was maintained arbitrary, allowing the models to be used in a variety of applications. The target-only cross section was shown to agree with previous work, producing exactly the same first-order expression if a monostatic geometry is imposed and the target is held to zero velocity. The second-order target-ocean component was seen to appear similarly as previous second-order ocean scattering radar cross sections.

In the following chapter, the expressions derived here are evaluated for a target travelling with constant velocity on the ocean surface. After introducing a target profile and ocean surface spectrum, the RCS will be computed and included in a radar model predicting the received signal from an ocean patch containing a marine vessel.

Chapter 4

Radar Cross Section Models of Ocean Surface Targets with Constant Velocity

In the analyses leading to this chapter, a radar cross section model for a deterministic target on the ocean surface was derived. In both the derivations of the electric fields in Chapter 2 and the determination of the cross section expressions themselves in Chapter 3, the target motion was left as arbitrary - to be defined as needed in specific applications. The only constraints imposed were that the total displacement over successive radar acquisitions must be small relative to the distance to either radar transmitter or receiver and the target must remain within a radar patch defined by the radar beamwidth and range resolution. The first part of this chapter imposes a constant target velocity on the models derived in Chapter 3 and simplifies the resulting RCS expressions.

The second part of this chapter applies the constant velocity models to a simplified model of a marine vessel featuring a tumblehome hull that narrows as its height above the ocean surface increases. In particular, the Swedish *Visby*-class corvette [29] is considered. The use of a tumblehome hull is an example of an RCS reduction, or 'stealth', technique through shaping. A ship's RCS may be reduced by avoiding vertical features and right angles, with the most significant reduction occurring for backscatter geometries at microwave and higher frequencies. It has been noted in previous literature that the HF RCSs of ships and large aircraft are relatively independent of shaping details as the overall target dimensions are of the same order of magnitude as the radar wavelength [60, 61]. Thus, HFSWRs are uniquely capable of detecting ships with hulls designed for low radar observability.

After defining a mathematical model of a simplified *Visby*-class corvette, example cross sections are calculated and implemented in a radar system model presented by Gill [62]. The system model is used to predict the frequency-domain power spectral density of the received signal from a radar cell on the ocean including a surface target. The results are compared with external noise sources as well as the returns from an ocean patch without a target to determine the ability to detect the presence of a ship either by direct target scatter, or through the secondary target-ocean return. The calculations are repeated for varying target orientations, velocities, ocean conditions, and bistatic angles. Characteristics of the results are then discussed. In a final example, time-series data for the radar returns of the ocean patch containing a target are simulated and processed in a similar manner as a pulsed Doppler radar. The results demonstrate how the received signal obtained by a practical radar may appear.

4.1 Cross Section Models for Targets with Constant Velocity

In this section, the expressions derived in Chapter 3 for the target-only RCS component, (3.25), and the target-ocean component, (3.33) are evaluated for a target moving with constant velocity, $\vec{v}$. To effect this, the time-varying component of the target position as defined in (2.8) is expressed as

$$\vec{\delta\rho}_t(t) = \vec{v}t \quad . \tag{4.1}$$

4.1.1 Target Scatter Component

For the target-only cross section, (3.25), the motion-related factor, M_t, is first considered. On substituting (4.1) into the definition of M_t, (3.17), the resulting expression reduces to

$$\begin{aligned} M_t(K, \theta_K, \tau, t) &= e^{-j\vec{K}\cdot\vec{v}\tau} \\ &= e^{-j2k_0 v \cos\phi_0 \cos(\theta_N - \theta_v)\tau} \quad , \end{aligned} \tag{4.2}$$

where v and θ_v are the magnitude and direction of $\vec{v}$ respectively and the stationary long-pulse value of $\vec{K} = 2k_0 \cos\phi_0 \hat{N}$ has been used. In [42], the ensemble average of a similar motion-related autocorrelation factor is evaluated for a sinusoidal displacement of the transmitting source through a temporal average. Here, (4.2) is seen to no longer contain a t dependency; it is therefore its own ensemble average. From (4.2) and (3.25), the target cross section component expression for constant velocity is

$$\sigma_t(\omega_d) = \frac{16k_0^4}{\pi} \cos^4\phi_0 |\mathcal{P}_0(2k_0\cos\phi_0\hat{N})|^2 \mathcal{F}\left[e^{-j2k_0 v\cos\phi_0\cos(\theta_N-\theta_v)\tau}\right] \quad . \tag{4.3}$$

From any standard Fourier transform table (e.g. Lathi [63], Chapter 7), the Fourier transform in (4.3) can be found as

$$\mathcal{F}\left[e^{-j2k_0 v\cos\phi_0\cos(\theta_N-\theta_v)\tau}\right] = 2\pi\delta(\omega_d + 2k_0 v\cos\phi_0\cos(\theta_N-\theta_v)) \quad , \tag{4.4}$$

and the target-only radar cross section component for uniform linear motion evaluates to

$$\sigma_t(\omega_d) = 32k_0^4\cos^4\phi_0|\mathcal{P}_0(2k_0\cos\phi_0\hat{N})|^2\delta(\omega_d + 2k_0 v\cos\phi_0\cos(\theta_N-\theta_v)) \quad . \tag{4.5}$$

It is observed here that the target cross section contains a delta function limiting the received signal to a single point in the Doppler domain at $\omega_d = -2k_0 v\cos\phi_0\cos(\theta_N - \theta_v)$. This is the expected bistatic Doppler shift for a target moving with constant velocity [64]. As a last point, if attention is limited to first-order scatters, only the leading term of $\mathcal{P}_0(2k_0\cos\phi_0\hat{N})$ is retained, and the RCS reduces to

$$\sigma_{1t}(\omega_d) = 32k_0^4\cos^4\phi_0|\Xi_{t0}(2k_0\cos\phi_0\hat{N})|^2\delta(\omega_d + 2k_0 v\cos\phi_0\cos(\theta_N-\theta_v)) \quad , \tag{4.6}$$

where the subscript, $1t$, refers to a first-order scatter from a target. In this case, if the Fourier transform of the surface target is known or pre-computed, the target RCS component can be calculated directly. If second-order target-only effects must be considered, the integration in the second-term of $\mathcal{P}_0(2k_0\cos\phi_0\hat{N})$ may be calculated numerically.

4.1.2 Second-Order Target-Ocean Cross Section

To form expressions for the second-order target-ocean cross section component, the motion related factor, which for this case is M_{to}, is again considered first. Using (4.1) and (3.22), an expression for M_{to} can be written for a target with constant velocity as

$$\begin{aligned} M_{to}(K,\theta_K,K_2,\theta_{K_2},\tau,t) &= e^{-j\vec{K}\cdot\vec{v}\tau}e^{j\vec{K}_2\cdot\vec{v}\tau} \\ &= e^{-j\tau\left[2k_0 v\cos(\theta_N-\theta_v)-K_2 v\cos(\theta_{K_2}-\theta_v)\right]} \quad . \end{aligned} \tag{4.7}$$

As was the case with (4.2), this expression is its own ensemble average. On substituting (4.7) into (3.33) and evaluating the Fourier transform, the second-order target-ocean cross-section for uniform linear motion is

$$\begin{aligned} \sigma_{to}(\omega_d) =& 128k_0^4\cos^4\phi_0 \int_{\vec{K}_2}\int_{\omega_2} S_1(\vec{K}_2,\omega_2) \\ &\cdot|\Xi_{t0}(\vec{K}-\vec{K}_2)|^2|_{SE}\Gamma_P(\vec{K}-\vec{K}_2,\vec{K}_2)|^2 \\ &\cdot\delta(\omega_d-\omega_2+2k_0v\cos(\theta_N-\theta_v)-K_2v\cos(\theta_{K_2}-\theta_v))d\omega_2 d\vec{K}_2 \quad . \end{aligned} \tag{4.8}$$

When compared to the target-only cross section given in (4.5), it may be observed that the delta function argument of the target-ocean cross section contains two additional terms, ω_2 and $K_2 v\cos(\theta_{K_2}-\theta_v)$. The former is the radian frequency of each ocean wave component that contributes to the integration; a similar term arises in derivations of second-order ocean cross sections (e.g. [18]). On writing the latter term as $\vec{K}_2\cdot\vec{v}$, it can be seen this term represents an additional phase shift corresponding to the target displacement between successive radar measurements projected along a given surface wave component. It will be seen in the next section that once an ocean wave spectrum model is introduced, the target-ocean cross section produces a continuous

Doppler response. This is in contrast to the single-frequency Doppler response of the target-only component.

4.2 Application to Marine Vessels

Here, the results of the previous section are applied to predict the radar returns from a simplified profile of a *Visby*-class corvette moving with a constant velocity. A mathematical model for a surface target is introduced, and a discussion regarding the model's constraints relative to the assumptions inherent to the analyses that resulted in (4.6) and (4.8) is presented in the context of tumblehome hulls. After specifying an ocean spectrum and radar system model, the cross section components and received power spectral density from an ocean patch containing a target are calculated. The calculations are repeated for varying operating parameters and conditions and observations are made regarding the ability to detect a ship in the presence of sea clutter.

4.2.1 Surface Target Model

The RCS models derived in this work require the Fourier transform of the surface target profile as an input. To facilitate the example calculations and subsequent analyses in this section, a mathematical model describing a general tumblehome shape is proposed. It is defined as

$$\xi_{t0}(x', y') = \frac{h_e}{4}\left[1 + \cos\left(\vec{K}_l \cdot \vec{\rho}\,'\right)\right]\left[1 - \frac{|\vec{K}_w \cdot \vec{\rho}\,'|}{\pi}\right] w(x', y'), \tag{4.9}$$

where h_e is the maximum height of the target, $\vec{K}_l, \vec{K}_w$ are orthogonal surface wave vectors, and $w(x', y')$ is a windowing function used to ensure the profile is zero outside of a rectangular region. It is noted that the subscript on ξ_{t0} indicates that this surface model forms a Fourier transform pair with Ξ_{t0}. Thus, the primed coordinate variables x' and y' are referred to the time-varying target origin $\vec{\rho}_t(t)$ that was defined in (2.3). To model a tumblehome-like shape, it is appropriate to set

$$\vec{K}_l = \frac{2\pi}{L}\hat{x}\ ,\ \vec{K}_w = \frac{2\pi}{W}\hat{y} \tag{4.10}$$

and specify a rectangular window function

$$w(x', y') = \begin{cases} 1, & |x'| \leq L, |y'| \leq W \\ 0, & \text{otherwise} \end{cases} . \tag{4.11}$$

The resulting shape is characterized by a raised cosine profile along its length and a triangular profile in width. It follows that (4.9) models a hull shape that narrows with height as required and accounts for the vessel's approximate volume, aspect ratio, and orientation.

The target profile that results from setting $L = 72.7$ m and $W = 10.4$ m in (4.10) and substituting the result into (4.9) is depicted in Figure 4.1. These dimensions correspond to the length and beam of the *Visby*-class [29]. In this manner, Figure 4.1 represents a simplified model of the *Visby*-class's tumblehome hull that is oriented along the x-axis. Arbitrary orientations may be modelled through suitable rotational transformations of (4.9). As the actual height of a *Visby*-class corvette was not available, the height of the model is set as the maximum value permitted under the small height approximation for a radar operating frequency of 3 MHz, or $h_e = 10$ m.

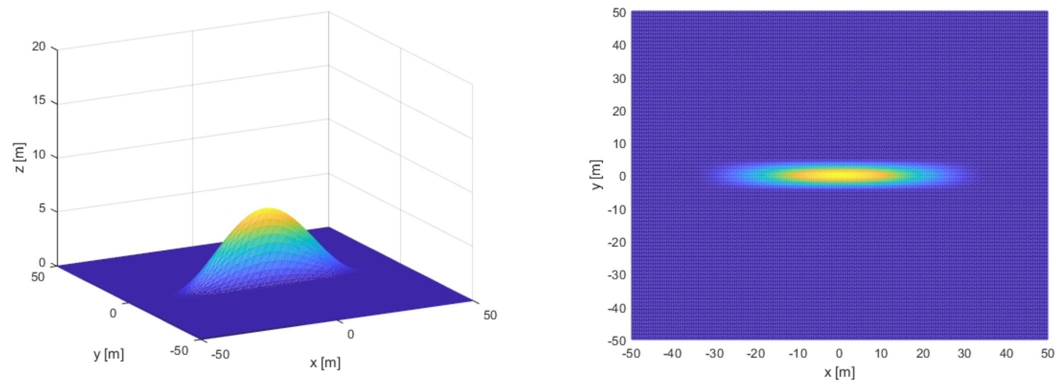

(a) Three-dimensional view (b) Top-down view

Figure 4.1: Simplified *Visby*-class model.

4.2.1.1 Surface Target Constraints

The key constraints related to the surface target definition are that it must be able to be described by an inverse Fourier transform and that it is small in height and slope. The requirement that the target profile be described by a Fourier transform suggests the results of this work are well suited to the modelling of cross sections of marine vessels with tumblehome hulls. As a tumblehome hull narrows as its height above the ocean surface increases, its exterior profile may be described as a surface, the elevation of which is a function of position in a flat plane. As a result, the surface profile will have a computable two-dimensional Fourier transform. Recent examples of modern warships have used tumblehome hulls to reduce their cross sections at microwave and higher frequencies [29, 30].

In Chapter 2, it was noted that according to Rayleigh theory, the maximum target height should be constrained to less than one tenth the operating wavelength of the radar. It should also be noted that it is typical for HF radars deployed for target detection and tracking to operate at the lower end of the band to achieve maximum range. Thus, for a practical application including the previously described 10 m tall target, a 3 MHz radar operating frequency will be considered in the example calculations later in this chapter.

In simplifying the expressions for the scattered electric field from the rough surface, Walsh and Gill [21] employed a small slope assumption that is inherited in this work. Additional details related to the small slope assumption may be found in [9], where the mean square slope of the ocean surface is used as the criterion to apply the approximation. The mean square slope of the target described by (4.9) is dependent on the surface wavenumbers K_l, K_w and its height. If the small slope assumption is applied, albeit somewhat liberally, to constrain the mean square slope, $\overline{|\nabla_{xy}\xi(x,y)|^2}$, such that

$$\overline{|\nabla_{xy}\xi(x,y)|^2} < \frac{1}{2} \quad , \tag{4.12}$$

and the values of K_l and K_w that produced Figure 4.1 are maintained, it is empirically found that the target height should be limited to approximately 4.2 m. Clearly, the model depicted in Figure 4.1 violates this constraint. For the purposes of this example, the height will be maintained at its small height limit of 10 m. In [21], the small slope assumption was similarly neglected for the first-order cross-section of a sphere. In that work, the RCS expression was found to be dimensionally consistent with, but 7 dB below, the accepted value for a small sphere. In that context, in violating the small-slope assumption, the radar returns associated with steeper aspects of the target are likely to be underestimated; however, the model will appropriately account for the target's volume, aspect ratio, orientation, and velocity. To prevent any errors this assumption may generate from compounding, consideration will be limited to single scatters from the target, i.e. the target-only cross section component will be limited to first-order.

In further consideration of the small slope assumption, it is observed that the shape defined by (4.9) avoids any sharp features. While ships that use shaping to reduce their RCS, including tumblehome hulls, avoid vertical or steep features, smaller aspects of a practical ship will violate the small slope requirement. This includes edges that may be present in the ship's hull and bridge as well as equipment installed on its deck. Previous works have noted that the decametric wavelengths of HF electromagnetic radiation limit the radar returns from such small features. This is evident in both a numerical study of skywave cross sections conducted in [28], and the fact that the commonly-used empirical model [5] is a function of only the ship displacement and radar operating frequency. Thus, for the purposes of estimating ship radar cross sections, including the target-ocean effect derived in this work, the smaller, steep features of a ship are neglected and only the general overall shape is considered.

4.2.2 Ocean Spectrum Model

In order to compute the target-ocean cross section component, a model for the first-order ocean spectrum, $S_1(\vec{K}, \omega)$, must be specified. In studying radar returns from the ocean surface, previous authors have focused attention on gravity-waves [9, 33].

These waves contain the majority of the ocean wave energy and have wavelengths on the same order of magnitude as electromagnetic radiation in the HF band. It follows that gravity waves interact strongly with signals from HF radars. If only gravity waves are considered and the ocean depth, d, near the target is sufficiently deep as compared to the wavelength of the ocean waves of interest, λ_w, (i.e. $\frac{d}{\lambda_w} \geq \frac{1}{2}$), a convenient form of the first-order surface power spectral density is [65]

$$S_1(\vec{K}, \omega) = \frac{1}{2} \sum_{m=\pm 1} S_1(m\vec{K}) \delta(\omega + m\sqrt{gK}) \quad . \tag{4.13}$$

In this work, the ocean spectrum will be obtained using a Pierson–Moskowitz ocean model for a fully developed sea and a cardioid distribution factor for $S_1(m\vec{K})$ with a spreading factor of 2. Similar models have been used in previous bistatic cross section modelling work by Gill and Walsh [18] and Ma *et al.* [66]. The resulting expression for $S_1(m\vec{K})$ in a form compatible with this work is

$$S_1(m\vec{K}) = \left[\frac{0.0081}{4K^2} e^{\left(\frac{-0.74g^2}{K^2 U^4} \right)} \right] \cdot \left[\frac{4}{3\pi} \cos^4 \left(\frac{\theta_{\vec{K}} + \frac{(1-m)\pi}{2} - \overline{\theta}}{2} \right) \right] \tag{4.14}$$

where U is the speed of the wind generating the waves 19.5 m above the ocean surface in m/s and $\overline{\theta}$ may be interpreted as the overall mean direction of the generating wind. The full details in deriving this model may be found in Chapter 3 of [9]. It may be noted that in applying this ocean model to the expressions developed in this work, the contribution of the wake produced by the surface target and any high-order wave interactions with the surrounding ocean that may result are neglected.

With the ocean spectrum model specified, the second-order target-ocean cross section can be further simplified by substituting (4.13) into (4.8). This gives

$$\sigma_{to}(\omega_d) = 64k_0^4 \cos^4\phi_0 \sum_{m=\pm1} \int_{\vec{K}_2} S_1(m\vec{K}_2)|\Xi_{t0}(\vec{K}-\vec{K}_2)|^2 |_{SE}\Gamma_P(\vec{K}-\vec{K}_2, \vec{K}_2)|^2$$
$$\cdot\, \delta(\omega_d + m\sqrt{gK_2} + 2k_0 v\cos(\theta_N - \theta_v) - K_2 v\cos(\theta_{K_2} - \theta_v))d\vec{K}_2 \quad , \tag{4.15}$$

where the ω_2 integral has yielded to the Dirac delta function in the ocean spectrum.

4.2.3 Radar System Model

With the target profile defined and an ocean spectrum model specified, the cross section expressions derived in Section 4.1 are able to be calculated for arbitrary target locations and velocities. To draw meaningful conclusions from the results, however, they must be considered in the context of the total signal received by the radar. This includes both the radar returns from the ocean itself (i.e. sea clutter) and external noise sources. If a particular region of ocean is considered, the magnitude of the clutter signal relative to the target and target-ocean returns can be determined directly from the ocean cross section expressions, (1.46) and (1.58), discussed in Chapter 1. A more detailed system model must be considered to determine the absolute strength of the received signal when comparing it with external noise sources. In [62], Gill and Walsh present two such models. The first model calculates the received power spectral density in the Doppler frequency domain, while the second method generates time-series data for the received signal. This section considers the frequency domain model while the time-series simulation is discussed in Section 4.3.

The radar cross section components given in (1.46) and (1.58) correspond to the first- and second-order returns from a differential area of the ocean surface. For a radar operating with an omnidirectional transmitting antenna and a separate narrowbeam receiving antenna in either bistatic or quasi-monostatic configurations, the received signal from the ocean for a specific delay (or, equivalently, range) may be attributed to a 'patch' defined by the radar's range resolution, or pulse width, and beamwidth. For the receiving array geometry shown in Figure 4.2, the patch area, A_p may be found as

$$A_p = \rho_{02}\Delta\rho_{0s}\theta_{BW} \quad , \tag{4.16}$$

where θ_{BW} is the beamwidth of the receiving antenna in radians and the remaining parameters were defined in Chapter 1. If the patch is considered sufficiently small such that the normalized ocean cross section components, $\sigma_{11}(\omega_d)$ and $\sigma_{2P}(\omega_d)$, may be considered constant over the patch, the aggregate clutter RCS, $\sigma_c(\omega_d)$, may be expressed as

$$\sigma_c(\omega_d) = A_p \left[\sigma_{11}(\omega_d) + \sigma_{2P}(\omega_d)\right] \quad . \tag{4.17}$$

When the returns from a target are included, a total RCS for a specific patch may be given as

$$\sigma_{total}(\omega_d) = \sigma_t(\omega_d) + \sigma_{to}(\omega_d) + A_p \left[\sigma_{11}(\omega_d) + \sigma_{2P}(\omega_d)\right] \quad . \tag{4.18}$$

The system model presented by Gill and Walsh [62] provides a means to determine the signal-to-noise ratio by computing both the received power spectral density of the signal and the noise spectral density measured by the radar. To determine the received power spectral density measured at the receiver, the radar equation is modified to

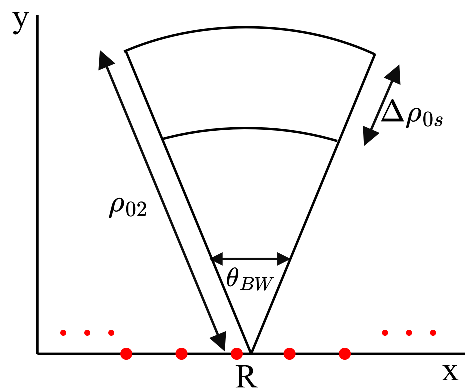

Figure 4.2: Receiving array geometry with elements along x-axis.

account for average (as opposed to peak) transmitter power. In this case, it is written as

$$\mathcal{P}(\omega_d) = \frac{\lambda_0^2 \left(\frac{\tau_0}{T_L}\right) P_t G_t G_r |F(\rho_{01}, \omega_0) F(\rho_{02}, \omega_0)|^2}{(4\pi)^3 \rho_{01}^2 \rho_{02}^2} \sigma(\omega) \tag{4.19}$$

where G_t and G_r are the transmitting and receiving antenna gains respectively, P_t is peak transmitter power, and T_L is the pulse repetition interval (PRI) such that the average transmitter power is $P_t \left(\frac{\tau_0}{T_L}\right)$. As written, equation (4.19) produces the received power spectral density of an arbitrary radar cross section. The power spectral density of the full patch may be obtained by substituting in $\sigma_{total}(\omega_d)$, while individual components may be calculated by substituting their respective values.

To predict the noise measured by a HF radar during a measurement, Gill [62] provides a model for the approximated noise power spectral density, $(\mathcal{P}_N)$. It is given in decibels by

$$(\mathcal{P}_N(f)) = -204 \text{ dB} + F_{am} \tag{4.20}$$

where f is the frequency in hertz, and F_{am} is the median external noise figure. It is well known that HF radars are frequently externally noise limited, i.e. the noise received from ambient sources dominates the internal noise generated by the radar. Thus, (4.20) represents, to a good approximation, the total noise signal. The International Telecommunication Union (ITU), provides recommended noise figure values for three significant categories, atmospheric, galactic, and man-made for a range of radar operating frequencies [67] that may be used in computing noise powers from (4.20).

To make use of (4.19) and (4.20), a set of radar operating parameters are listed in Table 4.1. These values are similar to those of a surface wave radar demonstrator installed at Cape Race in Newfoundland [25, 62, 68] for target tracking. The median external noise figure is taken as the linear sum of the three components given in [67] assuming a "quiet receiving site". The atmospheric noise component is taken as the average of its value exceeded 0.5% of the time and its value exceeded 99.5% of the time. In [62], a FORTRAN program [69] was used to compute the Sommerfeld attenuation function. As the program was not available, a representative value of 0.312 was assumed from [62]. The value is reported as the attenuation for a wind velocity of 15 m/s directed at an angle 120° relative to the look direction, for a radar operating frequency of 25 MHz. For the lower operating frequencies of the examples in this work, this value may be considered a conservative estimate. Lastly, it may be noted that the Cape Race radar evolved over a number of generations and the values used here reflect characteristics of different iterations, with the exception of the receiving beamwidth and the transmitting waveform whose chosen values are addressed below.

The first notable deviation from the Cape Race system is related to the receiving antenna aperture. In Table 4.1, the receiver beamwidth has been assumed to be 3°.

Parameter	Symbol	Value
Operating Frequency	f_0	3 MHz
Peak Transmitter Power	P_t	16 kW
Waveform		Pulsed Sinusoid
Pulse Width	τ_0	3 μs
Pulse Repetition Interval	T_L	500 μs
Transmitting Antenna Gain	G_t	2 dBi
Receiving Antenna Gain	G_r	19.67 dBi
Receiving Antenna Half Power Beamwidth	θ_{3dB}	3°
Median External Noise Figure	F_{am}	45 dB
Sommerfeld Attenuation Function	$F(\rho, \omega_0)$	0.312

Table 4.1: Radar operating parameters

If the array is assumed to be uniform and linear, the relationship between its length and beamwidth can be approximated as [70]

$$\theta_{3dB} = \frac{2.65\lambda_0}{(N+1)d} \quad , \tag{4.21}$$

where θ_{3dB} is the half power beamwidth of the array in radians, $(N+1)$ is the number of antenna elements, and d is the spacing between elements. For the 3° beamwidth and 3 MHz operating frequency assumed here, the total array length, $(N+1)d$, should be 1.69 km. While this length is approximately twice that of the Cape Race system, similar and longer arrays have been used in a number of HF skywave radars in the United States [71]. For a lossless long dipole array with $\lambda_0/2$ spacing, the gain may be estimated by [70]

$$G_r = \frac{5.48(N+1)d}{\lambda_0} \quad , \tag{4.22}$$

which evaluates to 92.61 for the receiving array. This value, in decibels, is reflected in the receiving antenna gain of Table 4.1 where antenna losses have been neglected.

The second notable deviation from the Cape Race demonstrator is that a pulsed waveform has been assumed, where the range resolution and signal bandwidth are fixed for a specified pulse width. All iterations of the Cape Race system employed some form of pulse compression to decouple the range resolution (or signal bandwidth) from the pulse width. In Table 4.1 the pulse width has been set to provide the same range resolution as the 375 kHz bandwidth used in [25]. It is noted here that the Walsh technique employed in this work has been used successfully to produce ocean cross section models for alternative waveforms [72, 73] but is considered outside the scope of this thesis and left for future work.

4.2.4 Computation of the Model

To compute the total RCS for a single radar cell of the system model described in the previous section, each term in (4.18) is first evaluated individually and the total RCS found as their sum. This section details the process of computing the target-related cross-section terms, σ_t and σ_{to}. The details for calculating the ocean surface RCS components may be found in [9,17,18]. Once the RCS components are calculated, the received power spectral density and signal-to-noise ratio (SNR) may be determined using the system and noise models given by (4.19) and (4.20) respectively.

As discussed in Section 4.2.1.1, the radar cross section contribution attributed to scatter directly from the target will be limited to first-order. The first-order target RCS, (4.6), can be directly computed once a profile's Fourier transform has been found. For the results in this chapter, the target model, as defined by (4.9), is specified numerically in MATLAB$^{\mathrm{R}}$ and the Fourier transform, $\Xi_{t0}(\vec{K})$, found using a suitably scaled Fast Fourier Transform (FFT) implementation. The required value of $\Xi_{t0}(\vec{K})$ for a given wavenumber $\vec{K}$ is extracted as needed.

The evaluation of the second-order target-ocean RCS is complicated due to the presence of the delta function whose argument is itself a function of the integration variable. To solve the delta function constraint, a technique similar to that previously employed in calculating second-order ocean cross sections employed by Gill [9] (and Barrick and Lipa [74] prior) will be adapted. The technique begins by introducing a change of variable, $Y = \sqrt{K_2}$, to the target-ocean cross section expression, (4.15), such that $K_2 dK_2 = 2Y^3 dY$ and rewriting (4.15) as

$$\begin{aligned}\sigma_{to}(\omega_d) =& 128 k_0^4 \cos^4\phi_0 \sum_{m=\pm 1} \int_{\theta_{K_2}=0}^{2\pi} \int_{Y=0}^{\infty} |\Xi_{t0}(\vec{K} - \vec{K}_2)|^2 \\ & \cdot S_1(m\vec{K}_2)|_{SE} \Gamma_P(2k_0 \cos\phi_0 \hat{N} - \vec{K}_2, \vec{K}_2)|^2 \delta(G(Y)) Y^3 dY d\theta_{K_2} \quad ,\end{aligned} \tag{4.23}$$

where

$$G(Y) \;=\; \omega_d \,+\, m\sqrt{g}Y \,-\, Y^2 v\cos(\theta_{K_2} \,-\, \theta_v) \,+\, 2k_0 v \cos\phi_0 \cos(\theta_N \,-\, \theta_v) \quad . \tag{4.24}$$

At this point, it is convenient to note the property of the Dirac delta function [75],

$$\delta(G(Y)) = \sum_k \frac{\delta(Y - Y_k)}{|G'(Y_k)|} \quad , \tag{4.25}$$

where the Y_k's are the zeros of $G(Y)$, and the singular point, $G'(Y_k) = 0$, must be excluded. Using (4.24) and (4.25), (4.23) can be cast as

$$\begin{aligned}\sigma_{to}(\omega_d) =& 128k_0^4 \cos^4\phi_0 \sum_{m=\pm1} \int_{\theta_{K_2}=0}^{2\pi} \sum_k \int_{Y=0}^{\infty} |\Xi_{t0}(\vec{K}-\vec{K}_2)|^2 \\ & \cdot S_1(m\vec{K}_2)|_{SE}\Gamma_P(2k_0\cos\phi_0\hat{N}-\vec{K}_2,\vec{K}_2)|^2 \\ & \cdot \frac{\delta\left(Y-Y_k\right)}{|m\sqrt{g}-2Y_k v\cos(\theta_{K_2}-\theta_v)|} Y^3 dY d\theta_{K_2} \quad .\end{aligned} \tag{4.26}$$

To calculate (4.26), a Riemann sum is used to approximate the θ_{K_2} integral. For each θ_K, the Y integral is found treating θ_{K_2} as a constant. The Y integral yields to the Dirac delta function, producing 0, 1, or 2 values to sum, depending on the number of real, non-zero solutions to $G(Y)=0$ found.

4.2.4.1 Significant Contributions to the Integrand

Prior to performing example calculations of (4.26) and discussing the results, it is noted that there are two sources of singularities and/or maxima within the integrand that have the potential to produce significant contributions to the target-ocean RCS. These are the symmetric electromagnetic coupling coefficient, ${}_{SE}\Gamma_P$, and the denominator of the fraction term seen in the final line of the equation.

In [9], Gill addresses the singularities of the electromagnetic coupling coefficient, as derived in that work. In this work, a refined coupling coefficient as found in [44] and given in (1.52)-(1.54) is employed that does not contain these singularities; however, it demonstrates similar behaviour and contains sharp local maxima for the same condition that produce the singularity observed in Gill's work. This condition is

$$\vec{K}_1 \cdot \left[\vec{K}_1 - 2k_0\hat{\rho}_2\right] = 0 \text{ or } \vec{K}_2 \cdot \left[\vec{K}_2 - 2k_0\hat{\rho}_2\right] = 0 \quad , \tag{4.27}$$

where, for the patch scatter case here, the unit vector $\hat{\rho_2}$ can be considered as the unit vector associated with $\vec{\rho_{02}}$ in Figure 2.2. Gill shows that the conditions in (4.27) represent circles in the $\vec{K}_1, \vec{K}_2$ complex planes and establishes that significant contributions occur when the circle is tangent to the integration contour for a given ω_d. These conditions are shown to correspond to the 'corner reflector' effect commonly observed in scattering applications. As the integration contours in this work are distinct from the ocean patch scatter addressed by Gill, the condition for a significant contribution may be unrelated to Gill's analysis. Thus, rather than formally derive a tangent condition, here it is simply acknowledged that significant contributions may occur for ω_d contours that pass near the circles in the $\vec{K}_1$ or $\vec{K}_2$ plane. This fact will be recalled as needed in the discussion of results of example calculations performed in the next section.

It also may be seen that when

$$2Y_k v \cos(\theta_{K_2} - \theta_v) = m\sqrt{g} \tag{4.28}$$

the denominator in the integrand of (4.26) evaluates to zero, resulting in a singularity. Recalling that $Y = \sqrt{K_2}$, the condition given in (4.28) may be re-written as

$$\frac{\vec{K}_2 \cdot \vec{v}}{K_2} = \frac{m}{2}\sqrt{\frac{g}{K_2}} \quad . \tag{4.29}$$

The left hand side of this expression can be interpreted as the component of the target velocity projected in the direction of the ocean wave vector $\vec{K}_2$, denoted $v_{\theta_{K_2}}$. The magnitude of the right hand side can be recognized as the group velocity of an ocean wave with wave number K_2. Thus, in the context of evaluating (4.26), for a given target velocity and ocean wave direction, a singularity can result from a secondary scatter involving an ocean wave with group velocity equal to $v_{\theta_{K_2}}$. If (4.28) is substituted into (4.24), it follows that the singularity will occur at the Doppler frequency,

$$\omega_d = -K_2 v \cos(\theta_{K_2} - \theta_v) - 2k_0 v \cos\phi_0 \cos(\theta_N - \theta_v). \tag{4.30}$$

The first term on the right hand side of (4.30) is the negative scalar product of the ocean wave vector that satisfies (4.29) with the target velocity, while the second term is the classical bistatic Doppler shift for uniform linear motion as seen in (4.6). Thus, (4.30) may be interpreted as the sum of two Doppler shifts, with one associated with translation across a specific ocean surface component and the second associated with the normal component of the target velocity relative to the radar geometry.

4.2.5 Results and Observations

To demonstrate the utility of the cross section models for detecting targets in the presence of sea clutter, the power spectral density of a scattered signal received by the system described in Section 4.2.3 from an ocean patch with and without the target defined in Section 4.2.1 are calculated. Where it is deemed helpful to the discussion, the individual radar cross section components are calculated and presented. Table 4.2 lists the nominal values for the target and wind velocities, as well as the location of ocean patch relative to the radar. It should be noted that angles are given relative to the positive x-axis in the receiver geometry shown in Figure 4.2. These values, in addition to those listed in Table 4.1 are used as inputs to the radar cross section components and system model. In the following four examples, the target speed, target heading, wind speed, and bistatic angle will be independently varied from their nominal values to observe their effects, if any, on target detection. All other values will remain as listed in Tables 4.1 and 4.2.

Parameter	Symbol	Value
Target Heading	θ_v	$-30°$
Target Speed	v	15 m/s
Wind Speed	U	8 m/s
Wind Direction	$\overline{\theta}$	0°
Bistatic Angle	ϕ_0	0° (monostatic)
Ellipse Normal Direction	θ_N	90°
Transmitter Range	ρ_{01}	50 km
Receiver Range	ρ_{02}	50 km

Table 4.2: Nominal parameters for calculations.

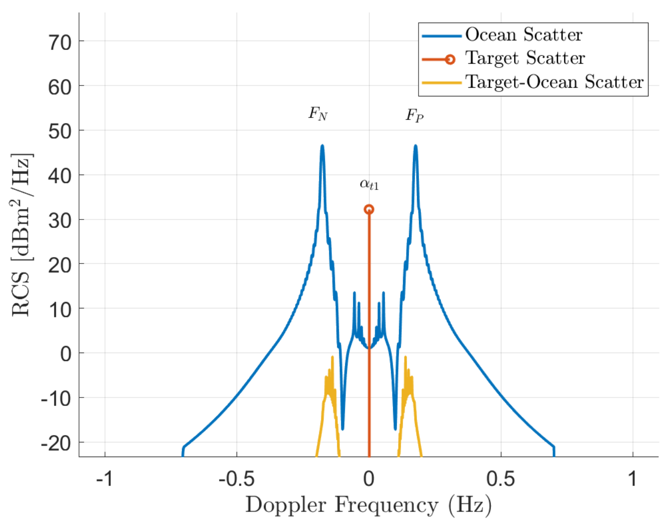

Figure 4.3: Radar cross section components of an ocean patch containing a *Visby*-class like target with zero-velocity and oriented along the x-axis. See Tables 4.1 and 4.2 for the various model parameters.

Prior to calculating and plotting cross sections and spectral densities for a variety of conditions, the zero-velocity case is first considered. The radar cross section components of an ocean patch containing the target described in Section 4.2.1 are calculated and plotted in Figure 4.3. In calculating the RCS components, the nominal values in Tables 4.1 and 4.2 have been used with the exception that the target has been oriented along the x-axis and fixed at zero-velocity, i.e. $\theta_v = 0$ and $v = 0$. This is evident in the first-order target RCS, depicted as an impulse at zero Doppler, labeled α_{t1}. The ocean cross section component contains the characteristic Bragg peaks, labeled F_N and F_P, at ± 0.1766 Hz as predicted by (1.47). It may be noted that for the radar operating frequency and sea state in this example, the ocean Doppler spectrum peaks attributed to second-order effects are not observed. Additionally, the second-order target-ocean contribution to the radar cross section is seen to be negligible, appearing as small bands on either side of α_{t1}. The second plot, Figure 4.4, contains the corresponding PSD of the sum of all components in Figure 4.3 as well as the PSD of just the ocean component. Also shown is the predicted noise floor. The PSD's are seen to completely overlap except for the target scatter peak, α_{t1}. While in this example, the second-order target ocean component does not significantly contribute to the total received PSD, it follows that if there is a discrepancy between the PSD of the total patch and the PSD of just the ocean contribution away from α_{t1}, it may be attributed to a target-ocean scatter component.

4.2.5.1 Varying Target Speed

In this example, the marine vessel's speed is varied from 0 to 15 m/s in 5 m/s increments while the target orientation and direction of motion is maintained at $-30°$

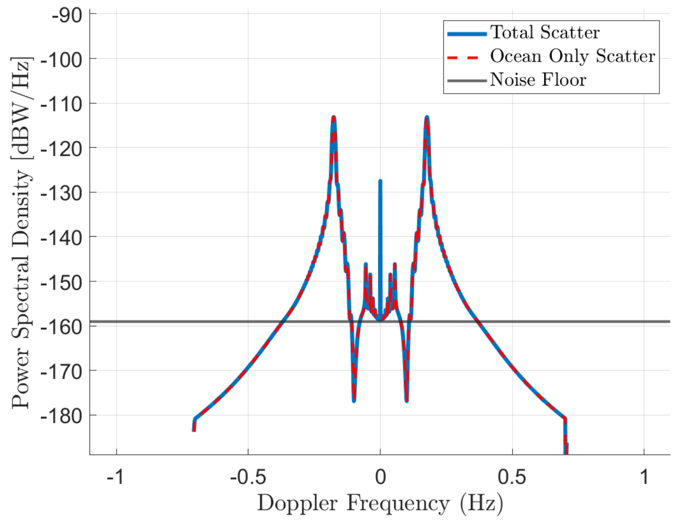

Figure 4.4: Received power spectral densities from an ocean patch with and without a *Visby*-class like target with zero-velocity and oriented along the x-axis. See Tables 4.1 and 4.2 for the various model parameters.

with respect to the positive x-axis. The resulting predicted received power spectral densities are plotted in Figures 4.5a through 4.5d and a summary of the locations and magnitudes of the first-order target and second-order target-ocean peaks is listed in Table 4.3. In the first three plots, the first-order return from the target manifests as a strong peak in the total scatter that is clearly distinguished from the ocean only scatter. The magnitude of this peak is approximately constant through the three plots, while the locations of these peaks shift to increasingly higher Doppler frequencies as predicted by the argument of the delta function in (4.6).

A particularly important result is observed in Figure 4.5d. The strong first-order ocean return almost entirely masks the first-order return from the target near $f_d =$ 0.15 Hz; however, a secondary peak occurs near $f_d = 0.0805$ Hz when the ship is present. Figure 4.6 plots the first-order target and second-order target cross section components separately, as well as the ocean patch cross section for this case. In

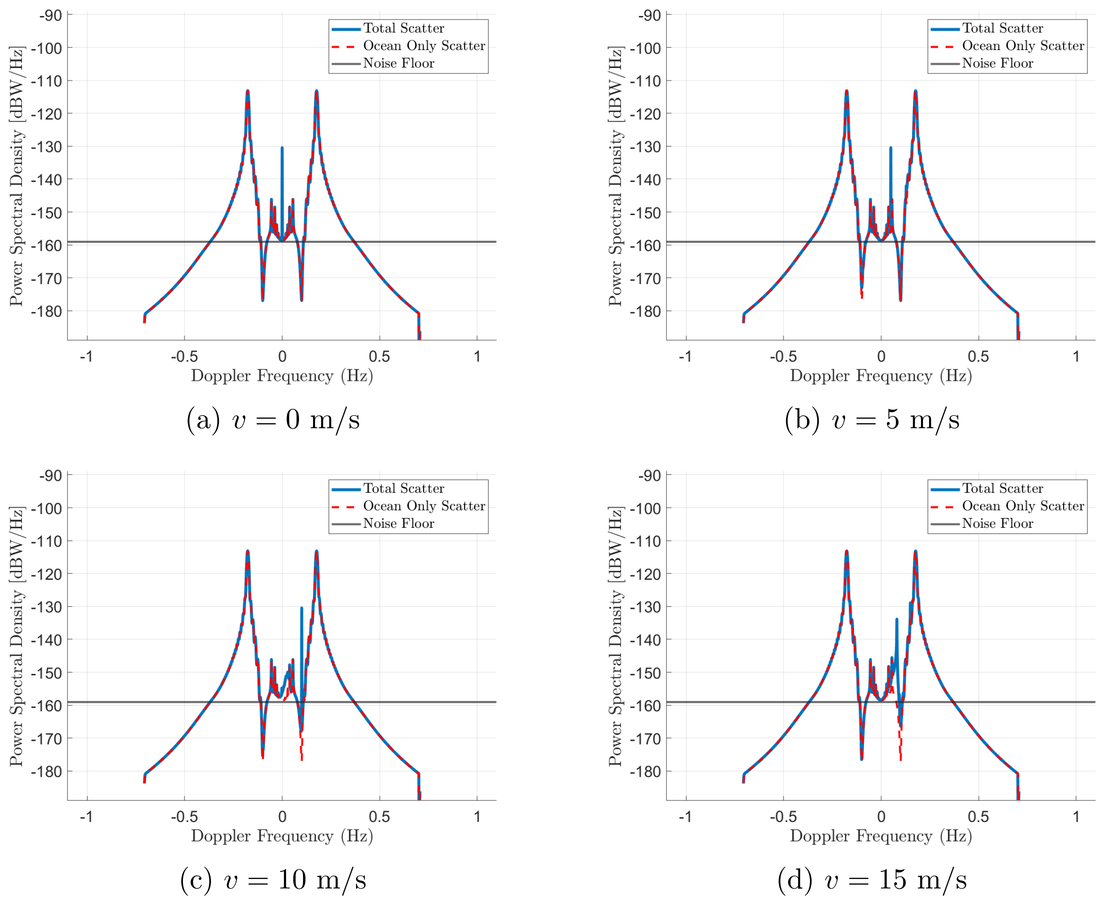

Figure 4.5: Predicted received power spectral densities from an ocean patch with and without a *Visby*-class like target with the parameters listed in Tables 4.1 and 4.2. The target speed, v, is set to 0, 5, 10, and 15 m/s in subfigures (a) through (d) respectively.

addition to the peaks identified in Figure 4.3, a strong second-order target-ocean peak, labelled α_{2to}, is observed for a Doppler frequency of $f_d = 0.0805$ Hz. Thus, it is the second-order target-ocean component of the radar cross section producing the additional peak in the total return. This suggests the possibility of detecting a ship masked by ocean clutter by its secondary scatter.

To illustrate how the strong peak in the second-order target-ocean component is generated, the $m = 1$ integration contour of the target-ocean cross section, as written

Target Speed [m/s]		$v=0$	$v=5$	$v=10$	$v=15$
First-order target peak	f_d [Hz]	0	0.0495	0.1003	0.1498
	$\mathcal{P}(f_d)$ [dBW]	-130.4	-130.4	-130.4	-128.9
Second-order target-ocean peak	f_d [Hz]	-	-	-	0.0805
	$\mathcal{P}(f_d)$ [dBW]	-	-	-	-133.9

Table 4.3: Summary of observations of the varying speed calculations depicted in Figure 4.5. A '$-$' indicates the corresponding peak was not observable for the specified target speed.

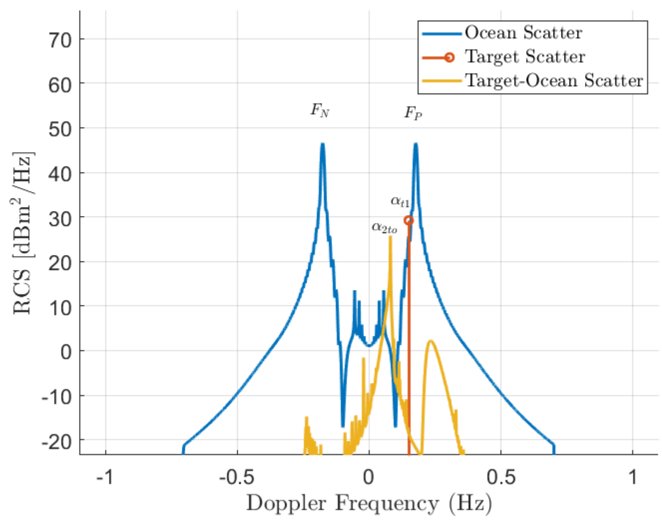

Figure 4.6: Radar cross section components of an ocean patch with a *Visby*-class like target with the parameters listed in Tables 4.1 and 4.2. The direction of target velocity, θ_v, is set to $-30°$.

in (4.15), in the $\vec{K}_1 = \vec{K} - \vec{K}_2$ plane is overlaid on a representation of the magnitude of the two-dimensional Fourier transform of the target profile, $\Xi_{t0}(\vec{K}_1)$, as shown in Figure 4.7. Two additional contours are also included in the plot that indicate conditions of singularities or sharp local maxima in the integrand of (4.26). The solid black contour corresponds to a singularity that arises when the denominator under the delta function in the cross section expression as written in (4.26) evaluates to zero. The dashed black contour represents the condition of a sharp local maximum in the symmetric electromagnetic coupling coefficient. This contour, as noted by Gill [9], takes the shape of a circle in the $\vec{K}_1$ plane. The red integration contour is seen to pass through an intersection of the singularity and maxima contours that occurs within the 'main lobe' of $|\Xi_{t0}|(\vec{K})$. It follows that the integration produces a significant value as three factors within the integrand are large in the neighbourhood of this intersection.

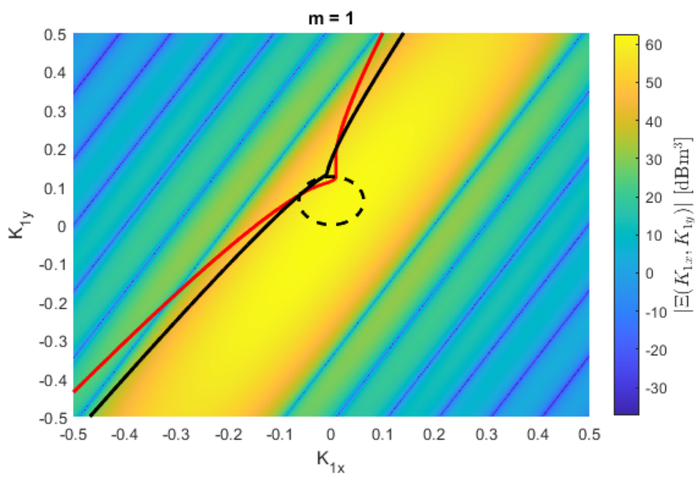

Figure 4.7: Illustration of the $m = 1$ integration contour for the second-order target-ocean cross section component in the $\vec{K}_1$ plane. The contour is shown in red and corresponds to the Doppler frequency of $f_d = 0.0805$ Hz in Figure 4.5d. The conditions that produce significant contributions are shown in solid and dashed black traces. The plot is overlaid on the magnitude of the Fourier transform of the target profile.

4.2.5.2 Varying Target Heading

Figures 4.8a through 4.8d depict the predicted received power spectral densities for target headings of $0°$, $-30°$, $-60°$, and $-90°$, with all angles referred to the positive x-axis. A summary of the locations and magnitudes of the first-order target and second-order target-ocean peaks is listed in Table 4.4. Similar to the previous example, each figure contains a peak in the total scatter corresponding to the first-order return from the target. The location of this peak corresponds to the Doppler shift due to the normal component of the ship's velocity increasing as predicted by the delta function of (4.6). Unlike the last example however, the magnitude of the first-order target RCS reduces as the direction of the ship is rotated. Physically, this may be explained as the projected cross sectional area of the target in the direction of the radar decreases from its maximum value when the ship is oriented along the x-axis ($\theta_v = 0°$), to its narrowest when the ship is heading directly towards the radar ($\theta_v = -90°$). Each plot in 4.8 also contains an observable second-order target-ocean contribution in the total return. In Figure 4.8a, the contribution appears as sharp peak to the left of the first-order peak. Figure 4.8b, contains the same results as 4.5d that were previously detailed. In Figures 4.8c and 4.8d the second-order target-ocean contribution appears as shoulders to the right of the first-order target peak. These results suggest that in addition to providing a means of detecting clutter-limited targets, information regarding the target orientation may be determined from the target-ocean returns.

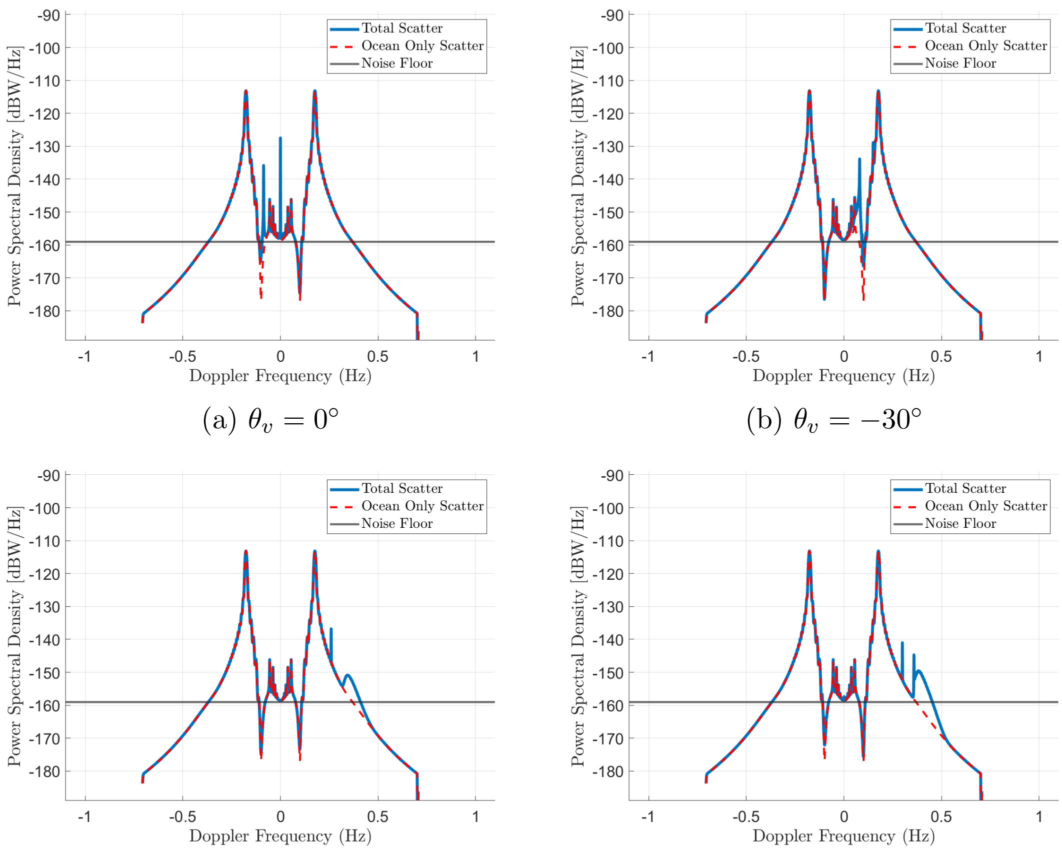

(a) $\theta_v = 0°$ (b) $\theta_v = -30°$

(c) $\theta_v = -60°$ (d) $\theta_v = -90°$

Figure 4.8: Predicted received power spectral densities from an ocean patch with and without a *Visby*-class like target with the parameters listed in Tables 4.1 and 4.2. The direction of target velocity, θ_v, is set to $0°$, $-30°$, $-60°$, and $-90°$ respectively in subfigures (a) through (d).

Target Heading [°]		$\theta_v = 0$	$\theta_v = -30$	$\theta_v = -60$	$\theta_v = -90$
First-order target peak	f_d [Hz]	0	0.1498	0.2600	0.3000
	$\mathcal{P}(f_d)$ [dBW]	-127.5	-128.9	-136.8	-141.0
Second-order target-ocean peak	f_d [Hz]	-0.862	0.0805	0.349	0.359
	$\mathcal{P}(f_d)$ [dBW]	-135.8	-133.9	-150.9	-144.7

Table 4.4: Summary of observations of the varying heading calculations depicted in Figure 4.8. A '$-$' indicates the corresponding peak was not observable for the specified target speed.

4.2.5.3 Varying Ocean Conditions

In Figure 4.9, the received power spectral densities have been calculated for three different sea-states. This is achieved by adjusting the speed of the wind generating the ocean waves to 5, 10, and 15 m/s. A summary of the locations and magnitudes of the first-order target and second-order target-ocean peaks is listed in Table 4.5. In the lowest sea-state, plotted in Figure 4.9a, the first-order target scatter peak at $f_d = 0.15$ Hz is observed to exceed that of the ocean clutter and noise floor, suggesting a target is likely to be successfully detected. As the sea-state increases, the first-order target peak is dominated by the first-order ocean clutter; however, an interesting effect is observed in the second-order target-ocean peak near $f_d = 0.0805$ Hz. When the wind speed increases from 5 to 10 m/s, the magnitude of this peak is seen to increase significantly relative to the ocean returns, and it is easily distinguished from the ocean clutter. As the wind speed is further increased to 15 m/s, higher-order peaks in the ocean clutter are seen to appear such that target-ocean return is difficult to discern. This suggests there may be a particular range of sea-states where the target-ocean returns provide a secondary detection mechanism.

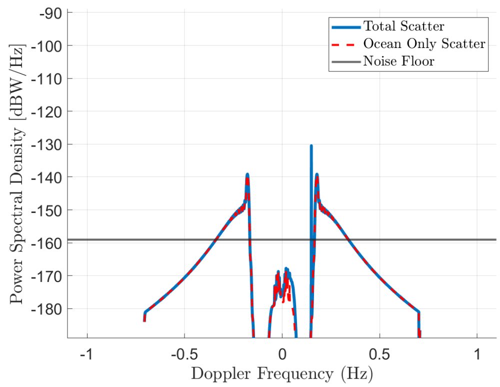

(a) $U = 5$ m/s

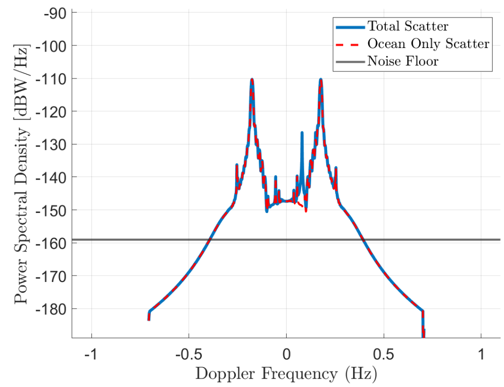

(b) $U = 10$ m/s

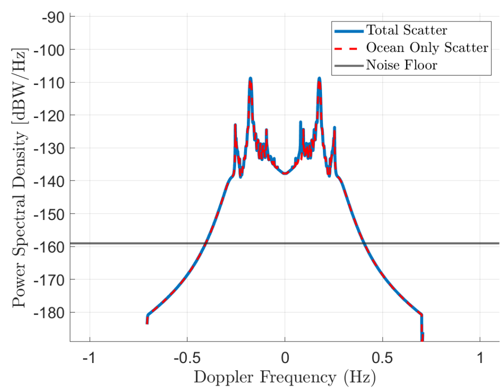

(c) $U = 15$ m/s

Figure 4.9: Predicted received power spectral densities from an ocean patch with and without a *Visby*-class like target with the parameters listed in Tables 4.1 and 4.2. The speed of the wind generating the ocean waves, U, is set to 5, 10, and 15 m/s in subfigures (a) through (c) respectively.

Wind Speed [m/s]		$U = 5$	$U = 10$	$U = 15$
First-order target peak	f_d [Hz]	0.1498	0.1498	-
	$\mathcal{P}(f_d)$ [dBW]	-130.5	-126.4	-
Second-order target-ocean peak	f_d [Hz]	-	0.0805	0.0805
	$\mathcal{P}(f_d)$ [dBW]	-	-126.5	-122.1

Table 4.5: Summary of observations of the varying ocean condition calculations depicted in Figure 4.9. A '$-$' indicates the corresponding peak was not observable for the specified target speed.

4.2.5.4 Varying Bistatic Angle

In a final example exploring the dependence on model inputs, the bistatic angle is set to 0°, 30°, and 60° and the results shown in Figure 4.10. The locations and magnitudes of the first-order target and second-order target-ocean peaks listed in Table 4.6. The plots show that the location of the first-order target peak has a stronger dependency on the bistatic angle than the locations of the first-order ocean peaks. From the delta function in equation (4.6), the Doppler shift of the target peak may be found as

$$f_{dt0} = \frac{2k_0 v \cos\phi_0 \cos(\theta_N - \theta_v)}{2\pi} = \frac{2v}{\lambda_0} \cos\phi_0 \cos(\theta_N - \theta_v) \quad , \tag{4.31}$$

while (1.47) gives the locations of the first-order Bragg peaks as $f_d = \pm\sqrt{2gk_0 \cos\phi_0}$. Thus, the target peak frequencies vary with $\cos\phi_0$ and the Bragg frequencies vary with $\sqrt{\cos\phi_0}$ and the behaviour seen in Figure 4.10 is expected. The results also show the second-order target-ocean peak shifting to lower Doppler frequencies for larger bistatic angles. As a consequence, for the same target and ocean conditions, the bistatic angle may determine whether a first-order target peak or second-order target-ocean peak is observable.

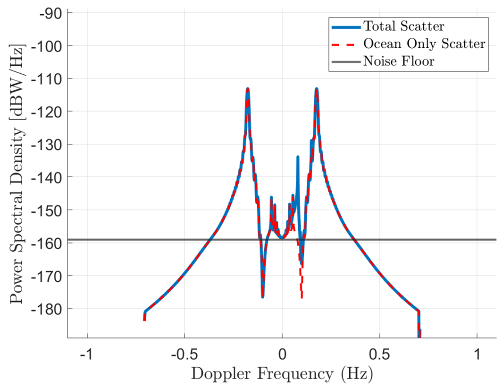

(a) $\phi_0 = 0°$

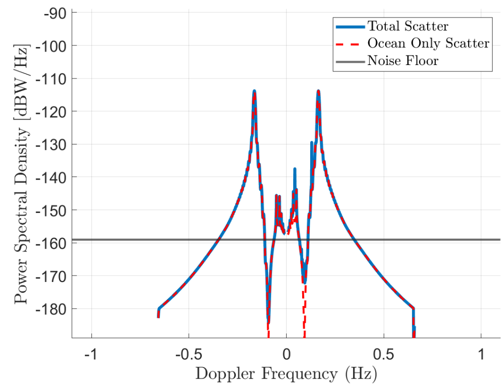

(b) $\phi_0 = 30°$

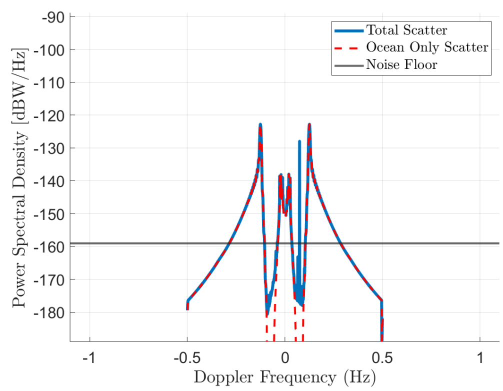

(c) $\phi_0 = 60°$

Figure 4.10: Predicted received power spectral densities from an ocean patch with and without a *Visby*-class like target with the parameters listed in Tables 4.1 and 4.2. The bistatic angle at the patch of interest, ϕ_0, is set to 0, 30, and 60 degrees in subfigures (a) through (c) respectively.

Bistatic Angle [°]		$\phi_0 = 0$	$\phi_0 = 30$	$\phi_0 = 60$
First-order target peak	f_d [Hz]	0.1498	0.1302	0.0749
	$\mathcal{P}(f_d)$ [dBW]	-128.9	-129.5	-127.8
Second-order target-ocean peak	f_d [Hz]	0.0805	0.0434	-
	$\mathcal{P}(f_d)$ [dBW]	-133.9	-137.5	-

Table 4.6: Summary of observations of the varying bistatic angle calculations depicted in Figure 4.10. A '$-$' indicates the corresponding peak was not observable for the specified target speed.

4.3 Time-Series Simulation

In the examples of the preceding section, received power spectral densities were computed directly in Doppler frequency domain. To model the process used in forming Doppler spectra by practical radars, Gill and Walsh [62] proposed a technique whereby time series data of both ocean clutter and external noises are simulated. The series are summed together in the time domain before being taken back to the frequency domain via the Fast Fourier Transform (FFT). The resulting PSD estimates account for the finite signal duration corresponding to a spreading out of sharp peaks in Doppler frequency. Here, the returns from the target and target-ocean contributions are included with the clutter returns to predict the power spectral density that may be estimated from the signal received by a HF radar.

To obtain a time series from the power spectral density of a one-dimensional stationary Gaussian process, Gill modifies a model used by Pierson [76]. The time-series, $f(t)$, is found as

$$f(t) = \int_B e^{j\omega t} e^{j\epsilon(\omega)} \sqrt{F_s(\omega) \frac{d\omega}{2\pi}} \quad , \tag{4.32}$$

where B is the total Doppler bandwidth of the signals, $F_s(\omega)$ is the power spectral density of $f(t)$, and $\epsilon(\omega)$ is a uniformly distributed random phase between 0 and 2π. To make use of (4.32), a signal power spectral density, $\mathcal{P}_s$, is defined as the PSD of the received signal due to the sum of the first-order and second-order target-ocean scatters. Similarly, a clutter PSD, $\mathcal{P}_c$, may be defined for the returns from the ocean surface, and a noise spectral density (NSD), $\mathcal{P}_n(\omega_d)$, defined for the signal produced by the external noise discussed in Section 4.2.3. By substituting

$$F_s(\omega) = \begin{cases} \mathcal{P}_s, & \text{for the signal process} \\ \mathcal{P}_n, & \text{for the noise process} \\ \mathcal{P}_c, & \text{for the clutter process} \end{cases}, \tag{4.33}$$

$f(t)$ may be recognized as

$$f(t) = \begin{cases} s(t), & \text{for the signal process} \\ n(t), & \text{for the noise process} \\ c(t), & \text{for the clutter process} \end{cases}. \tag{4.34}$$

The power spectral densities, $\mathcal{P}_s$ and $\mathcal{P}_c$, may be found by substituting the appropriate radar cross section components into (4.19). Gill addresses the external NSD for both finite and infinite series of pulses. For a sufficiently long series of pulses, $\mathcal{P}_n(\omega_d)$ may be approximated using (4.20).

To compute an example time series, a slightly modified scenario from the example in the previous section is modelled, with the full parameters listed in Table 4.7. In determining the total signal duration available to compute the FFT, the extent of the radar cell and target velocity must be considered. For the radar range resolution, target distance, and receiving antenna beamwidth, as well as the velocity of the target listed in Table 4.7, the maximum time-on-target is approximately 100 s. Knowing this, a discretized form of (4.32) is used to generate 2048-point time series realizations of the signal, noise, and clutter processes at a sampling frequency of 21 samples per second. The time series are summed and plotted in Figure 4.11.

Parameter	Symbol	Value
Operating Frequency	f_0	3 MHz
Waveform		Pulsed Sinusoid
Peak Transmitter Power	P_t	16 kW
Pulse Width	τ_0	6 μs
Pulse Repetition Interval	T_L	500 μs
Transmitting Antenna Gain	G_t	2 dBi
Receiving Antenna Gain	G_r	19.67 dBi
Receiving Antenna Half Power Beamwidth	θ_{3dB}	3°
Median External Noise Figure	F_{am}	45 dB
Sommerfeld Attenuation Function	$F(\rho, \omega_0)$	0.312
Target Heading	θ_v	−30°
Target Speed	v	15 m/s
Wind Speed	U	8 m/s
Wind Direction	$\overline{\theta}$	45°
Bistatic Angle	ϕ_0	0° (monostatic)
Ellipse Normal Direction	θ_N	90°
Transmitter Range	ρ_{01}	25 km
Receiver Range	ρ_{02}	25 km

Table 4.7: Parameters for time-domain simulations.

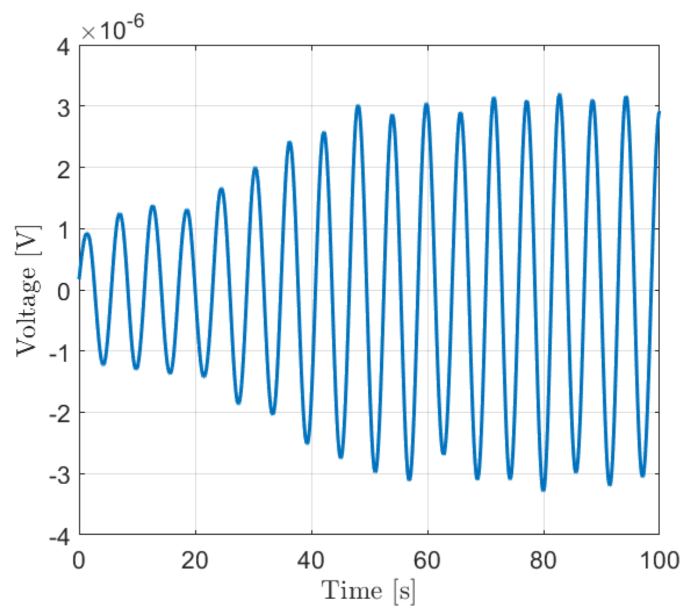

Figure 4.11: Simulated time-series data for the parameters listed in Table 4.7. The signal represents the received signal including returns from the target and ocean, as well as external noise sources.

To estimate the PSD of the total received signal shown in Figure 4.11, a 2048 sample FFT is first taken using a modified Bartlett-Hann window [77]. A periodogram estimate is then formed as the magnitude squared with a suitably scaled frequency axis and plotted in Figure 4.12. Also plotted in Figure 4.12 is the periodogram of the 'signal' comprised of only the clutter and noise components. The results show that the first-order return from the target, labeled α_{t1}, is almost entirely obscured by the positive Bragg peak, F_P, and could potentially be mis-identified as a shoulder of F_P. The second-order target-ocean peak, α_{2to}, however, is clearly distinguished from the background clutter and noise signal. Thus, this example has demonstrated how in a practical radar system, the second-order target-ocean scatter remains detectable and provides a means of detecting a ship otherwise masked by first-order clutter.

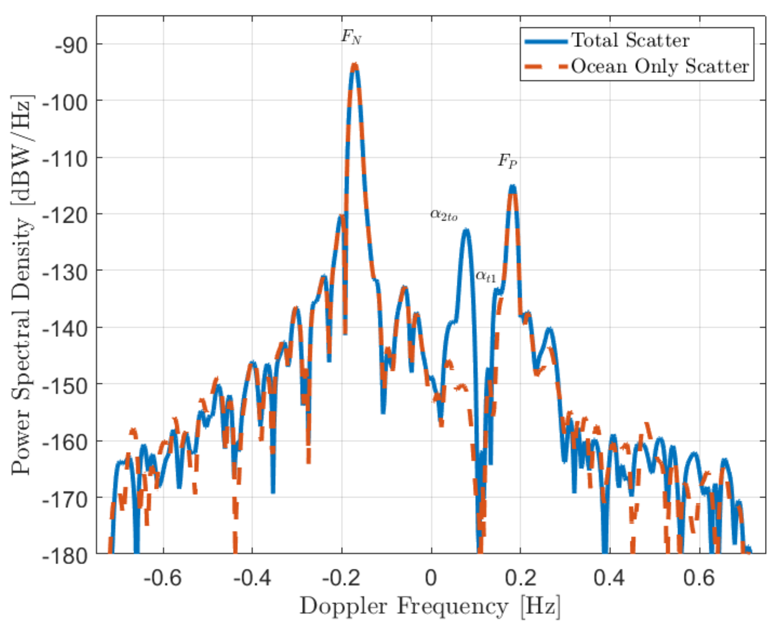

Figure 4.12: Periodogram of simulated time-series data.

4.4 Conclusion

In this chapter, the surface target radar cross section components derived in Chapter 3 were simplified for the case of a target moving with constant velocity. It was observed that the motion-related factor in the radar cross section component involving only scatters from the target reduced to a delta function constraining the response to a single Doppler frequency that is consistent with the expected bistatic Doppler shift from classical physics. The second-order target-ocean motion-related factor was reduced to a delta function whose argument included the classical bistatic Doppler shift, as well as terms related to the ocean and target displacement over a radar observation.

To demonstrate a practical application of the derived models, a surface target model corresponding to a simplified *Visby*-class corvette was introduced. In the context of the small height and slope assumptions inherent in the expressions derived in this work, constraints related to the target definition were addressed. It was concluded that the model was able to account for the target height, volume, orientation, velocity and aspect ratio. It was noted from the analysis of Walsh and Gill [21] that in neglecting higher-order slope components, the computed results were likely to underestimate radar cross sections by approximately 7 dB and larger returns may be expected in practical measurements.

The radar cross section expressions were computed for the representative surface target and included in a radar system model to predict the received signal strength under varying operating conditions. It was observed that under some conditions, the target-ocean cross section component produced an observable response when the target-only scatter was masked by sea-clutter. Thus, the second-order target-ocean scatter provides a means of target detection in clutter-limited scenarios. In a final example, the received radar signal was predicted using a time series simulation. This demonstrated that target-ocean scatter remains detectable when finite integration times that account for a practical radar range cell and target velocity are considered.

Chapter 5

Conclusions

5.1 Summary and Significant Results

The objective to develop a bistatic model of the HF radar cross section for a general surface target on the ocean that includes the effects of the ocean itself has been achieved. A model was derived by employing and extending previous analyses addressing scattering from the ocean and surface targets. The resulting cross section model was applied to the case of a marine vessel moving with constant velocity and incorporated into a system model of a representative coastal HF radar observing an ocean environment. Example computations demonstrated the utility of the model, with results indicating the expressions may be used to aid in the location and tracking of ships masked by ocean clutter in high sea states.

The model derivation initiated with an analysis of the scattered electric field from a surface target on a time-varying rough surface was presented in Chapter 2. The analysis utilized a transformation proposed by Walsh and Gill [21] for adapting expressions describing the scattered field from a rough surface to model the scattering from deterministic targets. In applying the transformation to bistatic expressions for rough surface scattering derived in [17], new expressions describing the bistatic scattered field from a surface target were obtained. To account for a second-order scatter involving both a deterministic target and the surrounding rough surface, the transformation was adapted such that it was only applied to a single scattering point. Subsequent analyses showed both an ocean-target and target-ocean field could be combined into a single electric field component using a symmetric electromagnetic coupling coefficient frequently seen in work addressing scattering from the ocean surface at HF. The bistatic electric field equations for target scatter were then simplified following a similar approach employed in [21], with one modification required to account for the new bistatic geometry. A nominal scattering location was assumed to allow for a stationary phase approximation in evaluating a convolutional integral. To validate this assumption, an alternative analysis assuming a large scatter patch was performed. This second approach is similar to that employed by other researchers in HF radar [11, 78] and produced equivalent electric field expressions.

The radar cross section models for a deterministic target embedded in a time-varying rough surface are formally derived in Chapter 3. The RCS expressions are found by first determining the power spectral density of the received scattered field through the Fourier transform of its autocorrelation function. To this point of the analysis, the models represent a general case where the target motion is left as arbitrary. The only simplifying assumption imposed is that the target displacement over successive radar acquisitions is considered small relative to the distance to either transmitter or receiver. It is observed that the resulting expressions contain similarities to those governing ocean scatter for HF radars installed on moving platforms [42,44,79], in that the motion of the target (or platform in the referenced works) is accounted for by the Fourier transform of the ensemble average of a complex exponential.

To demonstrate a practical application of the results presented in Chapter 3, the general-motion cross sections are simplified for the case of a surface target moving with constant velocity. The component of the RCS involving only target scatter was found to contain a Delta function corresponding to the classical bistatic Doppler shift. The second-order target-ocean component also contained a Delta function with an argument that included the classical bistatic Doppler shift in addition to terms related to ocean dispersion and the relative displacement of the target between radar acquisitions.

In the second part of Chapter 4 example cross sections were computed for a target profile representative of a Visby-class corvette. The cross sections were included in a system model representative of an HF radar demonstrator previously installed at Cape Race. The system model was used to predict the received signal strength including contributions from target scatter, ocean clutter, and external noise under varying conditions. The results of the example computations demonstrated the first-order target-only scatter behaved as expected in its magnitude response and Doppler shift. The most notable observation however, was that the second-order RCS contribution involving a target and ocean scatter was detectable in the presence of external noise and sea-clutter in certain configurations. This observation implies the model derived in this work may be used to aid in the location and tracking of ships masked by ocean clutter in high sea states. In a final demonstration, the system model was adapted to a time-series simulation to better represent the process used by practical radars to form Doppler spectra. For this example, a time series of a received radar signal was generated for the total duration a target remained within a radar cell. A Fourier transform was performed on the data to generate Doppler spectra. The results demonstrated that the second-order target-ocean scatter remains detectable when Doppler integration time is accounted for.

5.2 Suggestions for Future Work

In completing the research detailed in this dissertation, several areas of future developments have been identified. In undertaking the fundamental analyses that produced the RCS models of this work, the potential to extend the analyses to more general cases is apparent. Additionally, the results of example computations performed in Chapter 4 suggest a number of applications in which the models may be employed. This includes an experimental campaign to allow for a refinement of the RCS expressions. Some examples of potential future developments are discussed here.

In using the bistatic rough surface scattering expressions derived by Gill and Walsh [17,18], the analyses performed in this work inherently assume that the surface target may be considered small in both height and slope. The small height assumption considers the electrical height of the surface (i.e $k\xi << 1$), as such, the operating frequency used in the examples of this work were intentionally limited to the lower end of the HF band, where a target height of 10 m above the ocean surface was found to adhere to the Rayleigh limit of $k\xi < \frac{\pi}{5}$. Clearly for radars with operating frequencies at the upper end of the HF band, the applicability of this constraint will prevent the model's application to practical target heights. It follows that further analysis to address this limitation will increase the potential applications of the cross section models. In [43], correction terms to the small height ocean RCS were derived. One potential direction addressing the small height constraint would be to consider the applicability of these correctional terms to surface targets.

The small slope constraint considers the physical mean square slope of the surface target profile. In computing example cross sections of a tumblehome hull, it was noted that the small slope constraint represented a greater restriction on target height than the electrically small height limitation. Following [21], the small slope restriction was violated with the understanding the magnitude of the resulting RCSs will represent underestimates of the true value. Developing corrections to address this small slope constraint are likely to increase the suitability of the models to more general targets and increase the accuracy of the corresponding RCS estimates.

The surface target cross sections presented in this work correspond to electromagnetic scatters from ship hulls. It has been noted in previous works that the radar returns from small ships are dominated by scattering from vertical superstructures (e.g. masts) acting as resonant dipole or monopole scatterers [4, 80]. To produce RCS expressions for these targets including the ocean-target component found in this work, the scattering of a vertical linear conductor over a time-varying rough surface may be addressed. One method suited to this area of development is the Walsh analysis that forms the foundation of the derivations found in this dissertation. It may be expected that the target-ocean scatter from a dipole-like scatterer would appear to have similarities to the foot scatter discussed in Chapter 1 and analyzed by Gill and Walsh [9, 17, 18]. One challenge in this undertaking would be developing expressions for arbitrary and location-dependent source fields rather than the case of an elementary dipole at the origin.

As the cross sections derived in this work are relatively simple to compute, they can provide a significant benefit to future developments of signal processing techniques for the detection, tracking, and classification of surface targets in the presence of ocean clutter. This includes the ability to validate proposed signal processing algorithms without the need to undertake an expensive experimental campaign, as well as the ability to generate synthetic training data sets for use with machine learning techniques.

The example results presented in this dissertation are based on computations and simulations of the cross sections as well as a radar system model. While care was taken to account for practical considerations such as ocean clutter and the presence of external noise, an important area of future work is an experimental measurement campaign. By employing an operational HF radar and a cooperative target, the models derived in this work may be further validated and refined based on the measured results.

Bibliography

[1] W. Huang and E. W. Gill, *Ocean Remote Sensing Technologies: High frequency, marine and GNSS-based radar: High frequency, marine and GNSS-based radar*, 1st ed., ser. Radar, Sonar and Navigation. Stevenage: The Institution of Engineering and Technology, 2022.

[2] United Nations, "Law of the Sea, Part V—Exclusive Economic Zone," 2011.

[3] A. Ponsford, "Surveillance of the 200 nautical mile exclusive economic zone (EEZ) using high frequency surface wave radar (HFSWR)," *Canadian Journal of Remote Sensing*, vol. 27, no. 4, pp. 354–360, Aug. 2001. [Online]. Available: https://doi.org/10.1080/07038992.2001.10854877

[4] R. Bogle and D. Trizna, "Small boat HF radar cross sections," NAVAL RESEARCH LAB WASHINGTON DC, Tech. Rep., 07 1976.

[5] M. I. Skolnik, "An empirical formula for the radar cross section of ships at grazing incidence," *IEEE Transactions on Aerospace and Electronic Systems*, vol. AES-10, no. 2, pp. 292–292, 1974.

[6] H. Wilson and H. Leong, "An estimation and verification of vessel radar-cross-sections for HF surface wave radar," in *2003 Proceedings of the International Conference on Radar (IEEE Cat. No.03EX695)*, 2003, pp. 711–716.

[7] S. K. Podilchak, H. Leong, R. Solomon, and Y. M. M. Antar, "Radar cross-section modeling of marine vessels in practical oceanic environments for high-frequency surface-wave radar," in *2009 IEEE Radar Conference*, 2009, pp. 1–6.

[8] N. Lekic, D. Nikolic, B. Milanovic, D. Vucicevic, A. Valjarevic, and B. M. Todorovic, "Impact of radar cross section on HF radar survelance area: Simulation approach," in *2015 IEEE Radar Conference*, 2015, pp. 369–373.

[9] E. W. Gill, "The scattering of high frequency electromagnetic radiation from the ocean surface : an analysis based on a bistatic ground wave radar configuration," Ph.D. dissertation, Memorial University, 1999.

[10] D. D. CROMBIE, "Doppler spectrum of sea echo at 13.56 mc./s." *Nature*, vol. 175, no. 4459, pp. 681–682, Apr. 1955. [Online]. Available: https://doi.org/10.1038/175681a0

[11] D. Barrick, "First-order theory and analysis of MF/HF/VHF scatter from the sea," *IEEE Transactions on Antennas and Propagation*, vol. 20, no. 1, pp. 2–10, 1972.

[12] ——, "Remote sensing of sea state by radar," in *Ocean 72 - IEEE International Conference on Engineering in the Ocean Environment*, 1972, pp. 186–192.

[13] S. O. Rice, "Reflection of electromagnetic waves from slightly rough surfaces," *Communications on Pure and Applied Mathematics*, vol. 4, no. 2-3, pp. 351–378, 1951. [Online]. Available: https://onlinelibrary.wiley.com/doi/abs/10.1002/cpa.3160040206

[14] S. J. Anderson, "HF radar signatures of ship and submarine wakes," *The Journal of Engineering*, vol. 2019, no. 21, pp. 7512–7520, 2019. [Online]. Available: https://ietresearch.onlinelibrary.wiley.com/doi/abs/10.1049/joe.2019.0508

[15] J. Walsh, "On the theory of electromagnetic propagation accross a rough surface and calculations in the VHF region," Memorial University, Tech. Rep., 1980.

[16] S. K. Srivastava, "Scattering of high-frequency electromagnetic waves from an ocean surface : an alternative approach incorporating a dipole source," Ph.D. dissertation, Memorial University, 1984.

[17] E. W. Gill and J. Walsh, "Bistatic form of the electric field equations for the scattering of vertically polarized high-frequency ground wave radiation from slightly rough, good conducting surfaces," *Radio Science*, vol. 35, no. 6, pp. 1323–1335, 2000. [Online]. Available: https://agupubs.onlinelibrary.wiley.com/doi/abs/10.1029/2000RS002530

[18] ——, "High-frequency bistatic cross sections of the ocean surface," *Radio Science*, vol. 36, no. 6, pp. 1459–1475, 2001. [Online]. Available: https://agupubs.onlinelibrary.wiley.com/doi/abs/10.1029/2000RS002525

[19] J. Ryan, "The electromagnetic scattering from a vertical discontinuity with application to ice hazard detection : an operator expansion approach," Master's thesis, Memorial University, 1983.

[20] J. Walsh and R. Donnelly, "A new technique for studying propagation and scattering for mixed paths with discontinuities," *Proceedings of the Royal Society of London. A. Mathematical and Physical Sciences*, vol. 412, no. 1842, pp. 125–167, Jul. 1987. [Online]. Available: https://doi.org/10.1098/rspa.1987.0083

[21] J. Walsh and E. Gill, "An analysis of the scattering of high-frequency electromagnetic radiation from rough surfaces with application to pulse radar operating in backscatter mode," *Radio Science*, vol. 35, no. 6, pp. 1337–1359, 2000.

[22] Ansys, "Ansys HFSS." [Online]. Available: https://www.ansys.com/products/electronics/ansys-hfss

[23] D. S. SE, "CST Studio Suite 3D EM Simulation and Analysis Software." [Online]. Available: https://www.3ds.com/products-services/simulia/products/cst-studio-suite/

[24] J. Burke and A. Poggio, "Numerical electromagnetics code." [Online]. Available: https://www.nec2.org/

[25] R. Khan, B. Gamberg, D. Power, J. Walsh, B. Dawe, W. Pearson, and D. Millan, "Target detection and tracking with a high frequency ground wave radar," *IEEE Journal of Oceanic Engineering*, vol. 19, no. 4, pp. 540–548, 1994.

[26] D. Barrick, J. Headrick, R. Bogle, and D. Crombie, "Sea backscatter at HF: Interpretation and utilization of the echo," *Proceedings of the IEEE*, vol. 62, no. 6, pp. 673–680, 1974.

[27] L. Sevgi, "Target reflectivity and RCS interactions in integrated maritime surveillance systems based on surface-wave high-frequency radars," *IEEE Antennas and Propagation Magazine*, vol. 43, no. 1, pp. 36–51, 2001.

[28] D. Kouteas, "Investigation of high frequency ship radar cross section reduction by means of shaping," Master's thesis, Naval Postgraduate School, 1998.

[29] Saab AB, "Visby-class corvette," https://www.saab.com/products/visby-class-corvette, accessed: 2023-01-25.

[30] United States Navy, "Destroyers (DDG 1000)," https://www.navy.mil/Resources/Fact-Files/Display-FactFiles/Article/2391800/destroyers-ddg-1000/, 2023, accessed: 2023-10-13.

[31] Y. Demarty, L. Thirion-Lefevre, and V. Gobin, "Modelling of the electromagnetic scattering by sea surfaces at grazing incidence. application to HF surface wave radars," *Comptes Rendus Physique*, vol. 11, no. 1, pp. 87–95, 2010, propagation and remote sensing. [Online]. Available: https://www.sciencedirect.com/science/article/pii/S163107051000023X

[32] J. Rayleigh and R. Lindsay, *The Theory of Sound*, ser. Dover Books on Physics. Dover Publications, 1945, no. v. 2.

[33] D. E. Barrick, "Theory of HF and VHF propagation across the rough sea, 1, the effective surface impedance for a slightly rough highly conducting medium at grazing incidence," *Radio Science*, vol. 6, no. 5, pp. 517–526, 1971. [Online]. Available: https://agupubs.onlinelibrary.wiley.com/doi/abs/10.1029/RS006i005p00517

[34] D. Barrick, "Remote sensing of sea state by radar," in *Remote Sensing of the Troposphere*, V. Derr, Ed. Washington, D.C.: U.S. Govt., 1972, ch. 12, pp. 1–46.

[35] S. W. Thomson, "On ship waves," *Proceedings of the Institution of Mechanical Engineers*, vol. 38, no. 1, pp. 409–434, 1887. [Online]. Available: https://doi.org/10.1243/PIME_PROC_1887_038_028_02

[36] J. Walsh and S. K. Srivastava, "Rough surface propagation and scatter 1. general formulation and solution for periodic surfaces," *Radio Science*, vol. 22, no. 02, pp. 193–208, 1987.

[37] J. Walsh and R. Donnelly, "A new technique for studying propagation and scattering for mixed paths with discontinuities," *Proceedings of the Royal Society of London. A. Mathematical and Physical Sciences*, vol. 412, no. 1842, pp. 125–167, Jul. 1987. [Online]. Available: https://doi.org/10.1098/rspa.1987.0083

[38] ——, "Consolidated approach to two-body electromagnetic scattering," *Phys. Rev. A*, vol. 36, pp. 4474–4485, Nov 1987. [Online]. Available: https://link.aps.org/doi/10.1103/PhysRevA.36.4474

[39] J. Walsh, R. K. Howell, and B. Dawe, "Model development for evaluation studies of ground wave radar," Department of National Defence, Government of Canada, Tech. Rep., 1990.

[40] M. Teixeira Silva, "Generalized functions approach to the derivation of the high-frequency radar cross-section of ocean surfaces with electromagnetically-large waves," Ph.D. dissertation, Memorial University, 2021.

[41] S. Chen, E. W. Gill, and W. Huang, "A first-order HF radar cross-section model for mixed-path ionosphere–ocean propagation with an fmcw source," *IEEE Journal of Oceanic Engineering*, vol. 41, no. 4, pp. 982–992, 2016.

[42] J. Walsh, W. Huang, and E. Gill, "The first-order high frequency radar ocean surface cross section for an antenna on a floating platform," *IEEE Transactions on Antennas and Propagation*, vol. 58, no. 9, pp. 2994–3003, 2010.

[43] M. T. Silva, W. Huang, and E. W. Gill, "High-frequency radar cross section of the ocean surface with arbitrary roughness scales: Higher order corrections and general form," *IEEE Transactions on Antennas and Propagation*, vol. 69, no. 10, pp. 6723–6738, 2021.

[44] J. Walsh, W. Huang, and E. Gill, "The second-order high frequency radar ocean surface cross section for an antenna on a floating platform," *IEEE Transactions on Antennas and Propagation*, vol. 60, no. 10, pp. 4804–4813, 2012.

[45] J. Walsh, E. W. Gill, W. Huang, and S. Chen, "On the development of a high-frequency radar cross section model for mixed path ionosphere–ocean propa-

gation," *IEEE Transactions on Antennas and Propagation*, vol. 63, no. 6, pp. 2655–2664, 2015.

[46] S. Chen, E. W. Gill, and W. Huang, "A high-frequency surface wave radar ionospheric clutter model for mixed-path propagation with the second-order sea scattering," *IEEE Transactions on Antennas and Propagation*, vol. 64, no. 12, pp. 5373–5381, 2016.

[47] R. Shahidi and E. W. Gill, "Significant wave height estimation without doppler spectra," in *2018 18th International Symposium on Antenna Technology and Applied Electromagnetics (ANTEM)*, 2018, pp. 1–2.

[48] ——, "A new method for ocean spectrum extraction from high-frequency second-order doppler radar data," in *OCEANS 2016 MTS/IEEE Monterey*, 2016, pp. 1–4.

[49] M. T. Silva, E. W. Gill, and R. Shahidi, "A new nonlinear approach to extraction of ocean wave spectra from bistatic doppler hf-radar data," in *OCEANS 2017 - Aberdeen*, 2017, pp. 1–6.

[50] R. Shahidi and E. W. Gill, "An efficient and accurate solution for the extraction of non-directional ocean wave spectra from second-order high-frequency radar doppler spectra," in *OCEANS 2017 - Aberdeen*, 2017, pp. 1–6.

[51] ACOA, "Government of canada," Feb 2010. [Online]. Available: https://www.canada.ca/en/news/archive/2010/02/government-canada-invests-62-4-million-drive-growth-atlantic-canada-13-8-million-newfoundland-labrador-st-john-newfoundland-labrador.html

[52] Q. Zhou, L. Zhang, M. Li, X. Wu, X. Yue, and G. Yang, "Floating-platform high-frequency hybrid sky-surface wave radar: Simulations and experiments," *IEEE Transactions on Antennas and Propagation*, vol. 70, no. 4, pp. 3112–3117, 2022.

[53] Y. Ji, Z. Li, X. Wu, R. Qu, and Y. Wang, "First-order ocean surface echo model for shipborne HFSWR based on fusion estimation of antenna displacement," *IEEE Antennas and Wireless Propagation Letters*, vol. 22, no. 12, pp. 3082–3086, 2023.

[54] Y. Zhu, Y. Wei, and P. Tong, "First order sea clutter cross section for bistatic shipborne HFSWR," *Journal of Systems Engineering and Electronics*, vol. 28, no. 4, pp. 681–689, 2017.

[55] R. K. Donnelly, "The electromagnetic scattering from a vertical discontinuity with application to ice hazard detection : an operator expansion approach," Master's thesis, Memorial University, 1983.

[56] J. Walsh, B. Dawe, and S. Srivastava, "Remote sensing of icebergs by ground-wave doppler radar," *IEEE Journal of Oceanic Engineering*, vol. 11, no. 2, pp. 276–284, 1986.

[57] O. M. Phillips, *The dynamics of the upper ocean*, 2nd ed., ser. Cambridge monographs on mechanics and applied mathematics. Cambridge ;: Cambridge University Press, 1977.

[58] K. Hasselmann, "On the non-linear energy transfer in a gravity-wave spectrum part 1. general theory," *Journal of Fluid Mechanics*, vol. 12, no. 4, p. 481–500, 1962.

[59] R. S. Srivastava, "The contribution of multipathing effects in ground-wave radar return from the sea surface," Master's thesis, Memorial University, 1987.

[60] S. Anderson, "Counter-othr 101: low observability at hf," in *International Conference on Radar Systems (RADAR 2022)*, vol. 2022, 2022, pp. 405–410.

[61] J. M. Headrick and J. F. Thomason, "Applications of high-frequency radar," *Radio Science*, vol. 33, no. 4, pp. 1045–1054, 1998. [Online]. Available: https://agupubs.onlinelibrary.wiley.com/doi/abs/10.1029/98RS01013

[62] E. W. Gill and J. Walsh, "A combined sea clutter and noise model appropriate to the operation of high-frequency pulsed doppler radar in regions constrained by external noise," *Radio Science*, vol. 43, no. 4, 2008. [Online]. Available: https://agupubs.onlinelibrary.wiley.com/doi/abs/10.1029/2007RS003757

[63] B. Lathi and A. Sedra, *Linear Systems and Signals*, ser. Oxford series in electrical and computer engineering. Oxford University Press, 2005.

[64] N. Willis, *Bistatic Radar*, ser. Artech House radar library. Institution of Engineering and Technology, 2005.

[65] B. Kinsman, *Wind Waves: Their Generation and Propagation on the Ocean Surface*, ser. Dover Books on Chemistry and Earth Sciences. Dover Publications, 1984.

[66] Y. Ma, E. W. Gill, and W. Huang, "Bistatic high-frequency radar ocean surface cross section incorporating a dual-frequency platform motion model," *IEEE Journal of Oceanic Engineering*, vol. 43, no. 1, pp. 205–210, 2018.

[67] International Telecommunications Union, *Recommendation ITU-R P.372-14*, Std., aug 2019. [Online]. Available: https://www.itu.int/dms_pubrec/itu-r/rec/p/R-REC-P.372-14-201908-S!!PDF-E.pdf

[68] A. Ponsford, R. Dizaji, and R. McKerracher, "HF surface wave radar operation in adverse conditions," in *2003 Proceedings of the International Conference on Radar (IEEE Cat. No.03EX695)*, 2003, pp. 593–598.

[69] B. J. Dawe, "Radio wave propagation over earth : field calculations and an implementation of the roughness effect," Master's thesis, Memorial University, 1988.

[70] R. Collin, *Antennas and Radiowave Propagation*, ser. International student edition. McGraw-Hill, 1985.

[71] J. Thomason, "Development of over-the-horizon radar in the united states," in *2003 Proceedings of the International Conference on Radar (IEEE Cat. No.03EX695)*, 2003, pp. 599–601.

[72] J. Walsh, J. Zhang, and E. W. Gill, "High-frequency radar cross section of the ocean surface for an FMCW waveform," *IEEE Journal of Oceanic Engineering*, vol. 36, no. 4, pp. 615–626, 2011.

[73] H. Zhao, Y. Lai, Y. Wang, and H. Zhou, "High-frequency radar cross section of ocean surface for an fmicw source," *Journal of Marine Science and Engineering*, vol. 9, no. 4, 2021. [Online]. Available: https://www.mdpi.com/2077-1312/9/4/427

[74] B. J. Lipa and D. E. Barrick, *Analysis methods for narrow-beam high-frequency radar sea echo / Belinda J. Lipa, Donald E. Barrick*. Colorado: U.S. Dept. of Commerce, National Oceanic and Atmospheric Administration, Environmental Research Laboratories, 1982, 1982.

[75] R. Kanwal, *Generalized Functions Theory and Technique: Theory and Technique.* Birkhäuser Boston, 1998.

[76] W. J. Pierson, "Wind generated gravity waves," vol. 2, pp. 93–178, 1955. [Online]. Available: https://www.sciencedirect.com/science/article/pii/S006526870860312X

[77] Y. H. Ha and J. Pearce, "A new window and comparison to standard windows," *IEEE Transactions on Acoustics, Speech, and Signal Processing*, vol. 37, no. 2, pp. 298–301, 1989.

[78] D. Johnstone, "Second-order electromagnetic and hydrodynamic effects in high-frequency radio-wave scattering from the sea," Stanford Electron. Labs, Tech. Rep. 3615-3, 1975.

[79] Y. Ma, "Bistatic high frequency radar ocean surface cross section for an antenna on a floating platform," Ph.D. dissertation, Memorial University, 2017.

[80] D. Trizna and L. Xu, "Target classification and remote sensing of ocean current shear using a dual-use multifrequency HF radar," *IEEE Journal of Oceanic Engineering*, vol. 31, no. 4, pp. 904–918, 2006.

Appendix A

Summary of Electric Field Formation Process

To track the evolution of the three electric field components derived in Chapter 2, a flow chart depicting the general process is presented in Figure A.1. Additionally, Tables A.1 - A.3 describe the primary operation performed in each step and provide references to the relevant equations and page numbers.

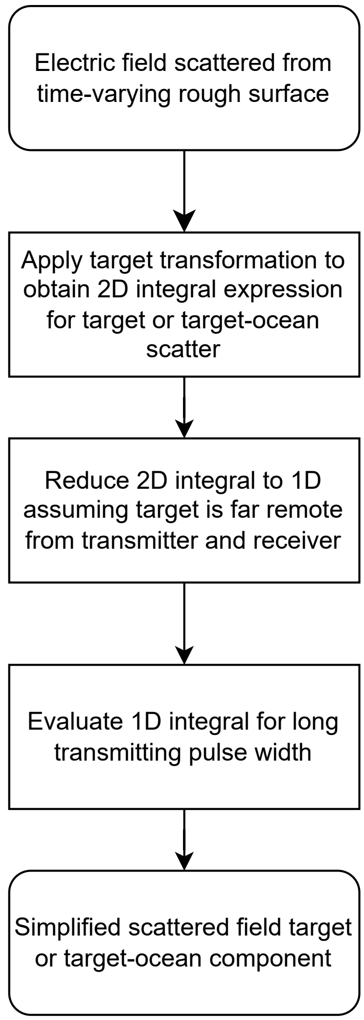

Figure A.1: Flowchart summarizing the process used in Chapter 2 for deriving scattered electric field components.

Step	Description	Symbol of Result	Equation Reference	Page Reference
0	Initial rough surface electric field expression	$(E_{0n}^{+})_1$	(2.1)	p. 43
1	Target substitution	$(E_{0n}^{+})_{1t}$	(2.3) - (2.5)	p. 44
2	Stationary phase integral		(2.7) - (2.14)	pp. 45 - 47
3	Long pulse assumption		(2.15) - (2.19)	pp. 47 - 48
4	Final target scattered electric field		(2.19)	p. 48

Table A.1: Summary of first-order target scattered electric field derivation.

Step	Description	Symbol of Result	Equation Reference	Page Reference
0	Initial rough surface electric field expression	$(E_{0n}^{+})_{2ep}$	(2.20)	p. 49
1	Target substitution	$(E_{0n}^{+})_{2t}$	(2.21) - (2.22)	p. 49
2	Stationary phase integral		(2.23) - (2.26)	pp. 50 - 51
3	Long pulse assumption		(2.27)	p. 51
4	Final target scattered electric field		(2.28)	p. 51

Table A.2: Summary of second-order target scattered electric field derivation.

Step	Description	Symbol of Result	Equation Reference	Page Reference
0	Initial rough surface electric field expression	$(E_{0n}^{+})_{2ep}$	(2.20)	p. 49
1	Target substitution	$(E_{0n}^{+})_{2to}$	(2.36)	p. 55
2	Stationary phase integral		(2.37) - (2.38)	pp. 56 - 56
3	Long pulse assumption		(2.39)	p. 57
4	Final target-ocean scattered electric field		(2.40)	p. 57

Table A.3: Summary of second-order target-ocean scattered electric field derivation.

Appendix B

Bistatic First-Order Scattered Electric Field from a Deterministic Target for a Continuous Wave Source

An alternative to the analysis detailed in Section 2.2 is presented here. In Section 2.2, the analysis began with an expression for the scattered field from a time-varying surface after a pulsed dipole transmitter is specified. The analysis here begins instead with the general case describing the scattered field from a time-invariant surface in the frequency domain. The transmitter is then assumed to be a dipole excited by a continuous wave source, and the surface region contributing to the scattered field is explicitly specified. The objective is to show both methods provide equivalent results and to justify the assumptions made in the final steps of simplifying the first-order scattered field from a deterministic surface target.

Figure B.1 depicts the geometry of a first-order scatter from a rough surface.

In [21], the normal component of the corresponding scattered electric field in the frequency domain is found to be

$$\left(E_{0n}^{+}\right)_1 \approx \frac{kC_0}{(2\pi)^2} \sum_{m,n} P_{\vec{K}_{mn}} K_{mn} \cdot \int_{y_1} \int_{x_1} \cos(\theta_{mn} - \theta_1) \frac{F(\rho_1)F(\rho_2)}{\rho_1 \rho_2} e^{j\vec{\rho}_1 \cdot \vec{K}_{mn}} e^{-jk(\rho_1+\rho_2)} dx_1 dy_1 \quad , \tag{B.1}$$

where k is the radar wavenumber, (x_1, y_1) is the scattering point location, and the surface is represented as

$$\xi(x,y) = \sum_{m,n} P_{\vec{K}_{mn}} e^{j\vec{\rho}\cdot\vec{K}_{mn}} \quad . \tag{B.2}$$

For a short transmitting dipole of length Δl, the parameter C_0 may be specified as a function of the excitation radian frequency ω,

$$C_0(\omega) = \frac{\Delta l k^2}{j\omega\epsilon_0} I(\omega), \tag{B.3}$$

where $I(\omega)$ is the current on the dipole and ϵ_0 is the permittivity of free space.

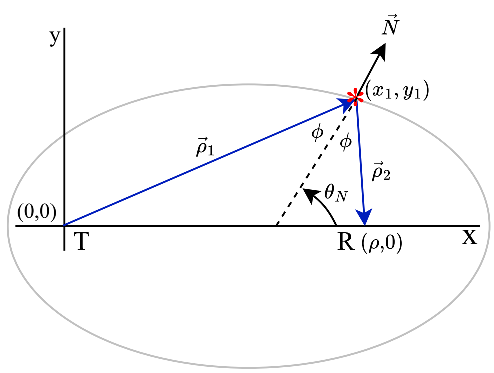

Figure B.1: First-order rough surface scatter.

Rather than finding a stationary phase approximation to (B.1) prior to finding a time-domain expression as in [21] or [18], the electric field expression will be taken immediately to the time-domain. Afterwards, a continuous wave source may be specified and the region of interest will be limited to a particular rectangular patch. Taking the inverse Fourier transform of (B.1)

$$\left(E_{0n}^{+}\right)_1(t) \approx \frac{1}{(2\pi)^2}\mathcal{F}_t^{-1}(kC_0) \overset{t}{*} \sum_{m,n} P_{\vec{K}_{mn}} K_{mn} \cdot \int_{y_1}\int_{x_1} \cos(\theta_{mn}-\theta_1)\frac{F(\rho_1,\omega_0)F(\rho_2,\omega_0)}{\rho_1\rho_2} e^{j\vec{\rho}_1\cdot\vec{K}_{mn}}\delta\left(t-\frac{\rho_1+\rho_2}{c}\right)dx_1 dy_1\ , \tag{B.4}$$

where $\mathcal{F}_t, \overset{t}{*}$ indicate a Fourier transform and convolution with respect to t respectively, and the frequency dependency of the Sommerfeld attenuation functions, $F(\ )$, has been explicitly written. Additionally, the approximate inverse Fourier transform

$$\mathcal{F}^{-1}\left[F(\rho_1,\omega)F(\rho_2,\omega)e^{jk(\rho_1+\rho_2)}\right] \approx F(\rho_1,\omega_0)F(\rho_2,\omega_0)\delta\left(t-\frac{\rho_1+\rho_2}{c}\right) \tag{B.5}$$

has been used where ω_0 is the central frequency of the excitation. This approximation is used in [21] with details discussed in [9].

On specifying a CW current source,

$$i(t) = I_0 e^{j\omega_0 t} \quad , \tag{B.6}$$

the inverse Fourier transform of kC_0 can be found following the work in [21] as

$$\begin{aligned}\mathcal{F}^{-1}(kC_0) &= j\frac{\eta_0 \Delta l}{c^2}\frac{\partial^2}{\partial t^2}\left[i(t)\right] \\ &= -j\eta_0 \Delta l I_0 k_0^2 e^{j\omega_0 t} \quad ,\end{aligned} \tag{B.7}$$

where $k_0 = \frac{\omega_0}{c}$. Substituting (B.7) into (B.4) and evaluating the convolution yields

$$\begin{aligned}\left(E_{0n}^{+}\right)_1(t) \approx & \frac{-j\eta_0 \Delta l I_0 k_0^2}{(2\pi)^2}\sum_{m,n} P_{\vec{K}_{mn}} K_{mn} e^{j\omega_0 t} \\ & \cdot \int_{y_1}\int_{x_1} \cos(\theta_{mn} - \theta_1)\frac{F(\rho_1, \omega_0)F(\rho_2, \omega_0)}{\rho_1 \rho_2} e^{j\vec{\rho}_1 \cdot \vec{K}_{mn}} e^{-jk_0(\rho_1+\rho_2)} dx_1 dy_1 \quad .\end{aligned} \tag{B.8}$$

Now, consideration will be limited to an $L \times L$ patch, centred at (x_{01}, y_{01}). First, the transformations

$$\begin{aligned}x_1 &= x_{01} + x_1' \quad \text{and} \\ y_1 &= y_{01} + y_1' \quad ,\end{aligned} \tag{B.9}$$

are introduced and used to write the distances ρ_1 and ρ_2 as

$$\begin{aligned}\rho_1 &= \sqrt{(x_{01} + x_1')^2 + (y_{01} + y_1')^2} \\ &= \rho_{01}\sqrt{1 + \frac{2x_{01}x_1' + 2y_{01}y_1'}{\rho_{01}^2} + \left(\frac{x_1' + y_1'}{\rho_{01}}\right)^2}\end{aligned} \tag{B.10}$$

and

$$\begin{aligned}\rho_2 &= \sqrt{[\rho - (x_{01} + x_1')]^2 + (y_{01} + y_1')^2} \\ &= \rho_{02}\sqrt{1 + \frac{-2(\rho - x_{01})x_1' + 2y_{01}y_1'}{\rho_{02}^2} + \left(\frac{x_1' + y_1'}{\rho_{02}}\right)^2}\end{aligned} \tag{B.11}$$

where $\rho_{01} = \sqrt{x_{01}^2 + y_{01}^2}$, and $\rho_{02} = \sqrt{(\rho - x_{01})^2 + y_{01}^2}$. If the distances from the radar transmitter and receiver to the patch are large relative to the patch extent, (i.e. ρ_1,

$\rho_2 \gg L$, (B.10) and (B.11) may be approximated as

$$\rho_1 \approx \rho_{01} + \vec{\rho}_{01} \cdot \vec{\rho}\,'_1 \tag{B.12}$$

and

$$\rho_2 \approx \rho_{02} - \vec{\rho}_{02} \cdot \vec{\rho}\,'_1 \quad , \tag{B.13}$$

where $\vec{\rho}\,'_1 = x'_1\hat{x} + y'_1\hat{y}$. Using these approximations allows (B.8) to be simplified to

$$\begin{aligned}\left(E_{0n}^{+}\right)_1(t) \approx &\frac{-j\eta_0 \Delta l I_0 k_0^2}{(2\pi)^2} \sum_{m,n} P_{\vec{K}_{mn}} K_{mn} e^{j\omega_0 t} e^{j\vec{\rho}_{01}\cdot\vec{K}_{mn}} e^{-jk_0(\rho_{01}+\rho_{02})} \\ &\cdot \int_{y'_2=\frac{L}{2}}^{\frac{L}{2}} \int_{x'_2=\frac{L}{2}}^{\frac{L}{2}} \cos(\theta_{mn}-\theta_1) \frac{F(\rho_1)F(\rho_2)}{\rho_1\rho_2} e^{j\vec{\rho}\,'_1\cdot\vec{K}_{mn}} e^{-jk_0\left[(\hat{\rho}_{01}-\hat{\rho}_{02})\cdot\vec{\rho}\,'_1\right]} dx'_1 dy'_1 \ .\end{aligned} \tag{B.14}$$

In Appendix A of [9], it is established that the ellipse normal bisects the angle between $\vec{\rho}_{01}$ and $\vec{\rho}_{02}$. Using this fact, it is easy to show that $\hat{\rho}_{01} - \hat{\rho}_{02} = 2\cos\phi_0\hat{N}$. If it is further assumed that factors in the integrand other than the exponential containing x'_1 and y'_1 are slowly varying and may be removed from the integral and replaced with their values at the centre of the patch, (B.4) can be re-written as

$$\begin{aligned}\left(E_{0n}^{+}\right)_1(t) \approx &\frac{-j\eta_0 \Delta l I_0 k_0^2}{(2\pi)^2} \sum_{m,n} P_{\vec{K}_{mn}} K_{mn} e^{j\omega_0 t} \\ &\cdot e^{j\vec{\rho}_{01}\cdot\vec{K}_{mn}} e^{-jk_0(\rho_{01}+\rho_{02})} \cos(\theta_{mn}-\theta_{01}) \frac{F(\rho_{01})F(\rho_{02})}{\rho_{01}\rho_{02}} \\ &\cdot \int_{y'_1=\frac{L}{2}}^{\frac{L}{2}} \int_{x'_1=\frac{L}{2}}^{\frac{L}{2}} e^{j\vec{\rho}\,'_1\cdot\vec{K}_{mn}} e^{-j2k_0\cos\phi_0\hat{N}\cdot\vec{\rho}\,'_1} dx'_1 dy'_1 \quad .\end{aligned} \tag{B.15}$$

The double integration in (B.15) can be carried out as

$$
\begin{aligned}
I_{x_1',y_1'} &= \int_{y_1'=\frac{L}{2}}^{\frac{L}{2}} \int_{x_1'=\frac{L}{2}}^{\frac{L}{2}} e^{j\vec{\rho}_1'\cdot\vec{K}_{mn}} e^{-j2k_0\cos\phi_0\hat{N}\cdot\vec{\rho}_1'} dx_1' dy_1' \\
&= \int_{x_1'=\frac{L}{2}}^{\frac{L}{2}} e^{jx_1'(K_{mn,x}-2k_0\cos\phi_0 N_x)} dx_1' \int_{y_1'=\frac{L}{2}}^{\frac{L}{2}} e^{jy_1'(K_{mn,y}-2k_0\cos\phi_0 N_y)} dy_1' \\
&= L\mathrm{Sa}\left[\frac{L}{2}\left(K_{mn,x} - 2k_0\cos\phi_0 N_x\right)\right] L\mathrm{Sa}\left[\frac{L}{2}\left(K_{mn,y} - 2k_0\cos\phi_0 N_y\right)\right] \ ,
\end{aligned}
\tag{B.16}
$$

where the x and y subscripts added to the magnitude quantities K_{mn} and N indicated the x and y components of their corresponding vectors. Using (B.16) in (B.15) gives

$$
\begin{aligned}
\left(E_{0n}^{+}\right)_1(t) \approx & \frac{-j\eta_0\Delta l I_0 k_0^2}{(2\pi)^2} \sum_{m,n} P_{\vec{K}_{mn}} K_{mn} e^{j\omega_0 t} \\
& e^{j\vec{\rho}_{01}\cdot\vec{K}_{mn}} e^{-jk_0(\rho_{01}+\rho_{02})} \cos(\theta_{mn}-\theta_{01}) \frac{F(\rho_{01})F(\rho_{02})}{\rho_{01}\rho_{02}} \\
& \cdot L\mathrm{Sa}\left[\frac{L}{2}\left(K_{mn,x} - 2k_0\cos\phi_0 N_x\right)\right] \\
& \cdot L\mathrm{Sa}\left[\frac{L}{2}\left(K_{mn,y} - 2k_0\cos\phi_0 N_y\right)\right] \quad ,
\end{aligned}
\tag{B.17}
$$

To use (B.17) in modelling the scattered electric field from a moving deterministic surface target, the required transformation that is equivalent to (1.67) can be identified as

$$
P_{\vec{K}_{mn}} \rightarrow e^{-j\vec{K}\cdot\vec{\rho}_t(t)} \Xi_{t0}(\vec{K}) \frac{d\vec{K}}{(2\pi)^2} \qquad . \tag{B.18}
$$

Applying this to (B.17) yields

$$
\begin{aligned}
\left(E_{0n}^{+}\right)_1(t) \approx\ & \frac{-j\eta_0 \Delta l I_0 k_0^2}{(2\pi)^4} e^{j\omega_0 t} \int_{\vec{K}} e^{-j\vec{K}\cdot\vec{\rho}_t(t)} \Xi_{t0}(\vec{K}) K \\
& \cdot e^{j\vec{\rho}_{01}\cdot\vec{K}} e^{-jk_0(\rho_{01}+\rho_{02})} \cos(\theta_K - \theta_{01}) \frac{F(\rho_{01})F(\rho_{02})}{\rho_{01}\rho_{02}} \\
& \cdot L\mathrm{Sa}\left[\frac{L}{2}\left(K_x - 2k_0 \cos\phi_0 N_x\right)\right] \\
& \cdot L\mathrm{Sa}\left[\frac{L}{2}\left(K_y - 2k_0 \cos\phi_0 N_y\right)\right] d\vec{K} \quad .
\end{aligned} \tag{B.19}
$$

If the rectangular patch is sufficiently large, the sampling functions in (B.19) may be approximated as

$$
L\mathrm{Sa}\left[\frac{L}{2}\left(K_x - 2k_0 \cos\phi_0 N_x\right)\right] \rightarrow 2\pi \cos\phi_0 \delta(K_x - 2k_0 \cos\phi_0 N_x) \tag{B.20}
$$

and

$$
L\mathrm{Sa}\left[\frac{L}{2}\left(K_x - 2k_0 \cos\phi_0 N_x\right)\right] \rightarrow 2\pi \cos\phi_0 \delta(K_y - 2k_0 \cos\phi_0 N_y) \quad . \tag{B.21}
$$

Under this condition, (B.19) simplifies to

$$
\begin{aligned}
\left(E_{0n}^{+}\right)_1(t) \approx\ & \frac{-j2\eta_0 \Delta l I_0 k_0^3 F(\rho_{01})F(\rho_{02})}{(2\pi)^2 \rho_{01}\rho_{02}} \cos^2(\phi_0) \Xi_{t0}(\vec{K}) \\
& \cdot e^{jk_0\Delta\rho_s} e^{j\vec{\rho}_{01}\cdot\vec{K}} e^{-j\vec{K}\cdot\vec{\rho}_{0t}} e^{-j\vec{K}\cdot\delta\vec{\rho}_t(t)} \quad ,
\end{aligned} \tag{B.22}
$$

where $\vec{K} = 2k_0 \cos\phi_0 \hat{N}$ as a result of the delta function constraints and the identity $\phi_0 = \theta_N - \theta_{01}$ was used from Figure B.1. Additionally the first exponential was found using the identity

$$
e^{j\omega_0 t} e^{-jk_0(\rho_{01}+\rho_{02})} = e^{jk_0\Delta\rho_s} \tag{B.23}
$$

derived in [18].

Comparing (B.22) to the first-order target scatter electric field in (2.19), they are seen to be equivalent, with the exception of a few phase terms that are constant with respect to t. In Chapter 3, radar cross sections are obtained from these expressions by finding the power spectral density as the Fourier transform of the autocorrelation function. This operation results in the elimination of constant phase terms; thus RCS expressions derived using either electric field will produce the same result.

Appendix C

Reduction to Monostatic Zero-Velocity, Target-Only Cross Sections

In Section 3.3 it was shown the first-order target-only RCS component derived in this work reduces to its monostatic, zero-velocity equivalent derived in previous work by Walsh and Gill [21]. In this appendix, the comparison is extended to the second-order where it will be shown that the expressions generated by this work are in general agreement with those reported in [21], with the exception of an additional factor that is attributed to the use of a refined electromagnetic coupling coefficient that is derived in subsequent work by Walsh in [44].

In [21], the monostatic RCS model for perfectly conducting, stationary surface targets is found to second-order as

$$\sigma_t = \frac{16k_0^4}{\pi}|\mathcal{P}|^2 \quad , \tag{C.1}$$

with $\mathcal{P}$ defined as

$$\mathcal{P} = \Xi_{t0}(2k_0, \theta_1) + \frac{1}{2(2\pi)^2} \int_{\vec{K}} \Xi_{t0}(k_0\hat{\rho}_1 + \vec{K})\Xi_{t0}(k_0\hat{\rho}_1 - \vec{K}) \frac{|\vec{K} \times \hat{\rho}_1|^2}{\sqrt{K^2 - k_0^2}} d\vec{K} \quad . \tag{C.2}$$

In Section 3.3, the target-only RCS derived in this work was shown to reduce to

$$\sigma_t = \frac{16k_0^4}{\pi} |\mathcal{P}_0(2k_0\hat{\rho}_{01})|^2 \quad , \tag{C.3}$$

where $\mathcal{P}_0(2k_0\hat{\rho}_{01})$ was found using (2.35) as

$$\begin{aligned} \mathcal{P}_0(2k_0\hat{\rho}_{01}) =& \Xi_{t0}(2k_0\hat{\rho}_{01}) + \frac{1}{(2\pi)^2} \int_{\vec{K}''} \Xi_{t0}\left(k_0\hat{\rho}_{01} + \vec{K}''\right) \Xi_{t0}\left(k_0\hat{\rho}_{01} - \vec{K}''\right) \\ & \cdot \; {}_{SE}\Gamma_P\left(k_0\hat{\rho}_{01} + \vec{K}'', k_0\hat{\rho}_{01} - \vec{K}''\right) d\vec{K}'' \; . \end{aligned} \tag{C.4}$$

To properly compare the RCS expressions the electromagnetic coupling coefficient, ${}_{SE}\Gamma_P$, in (C.4) must be expanded. The monostatic form of the electromagnetic coupling coefficient used in this work is found in [44] (where it is denoted by ${}_2C_2$) as

$${}_{SE}\Gamma_P(\vec{K}_1, \vec{K}_2) = \frac{jk_0}{2K_T^2} \frac{|\vec{K}_1 \times \vec{K}_2|^2}{k_0^2 - \vec{K}_1 \cdot \vec{K}_2} \left\{ 1 - j\frac{k_0(1+\Delta)}{\sqrt{-\vec{K}_1 \cdot \vec{K}_2} + jk_0\Delta} \right\} \quad , \tag{C.5}$$

where $\vec{K}_1$ and $\vec{K}_2$ are arbitrary surface wave vectors, $\vec{K_T} = \vec{K}_1 + \vec{K}_2$, and Δ is the surface impedance. It is easy to show that (C.5) can also be written as

$${}_{SE}\Gamma_P(\vec{K}_1, \vec{K}_2) = \frac{|\vec{K}_1 \times \vec{K}_2|^2}{2K_T^2 \left[\sqrt{-\vec{K}_1 \cdot \vec{K}_2} + jk_0\Delta\right]} \frac{k_0}{k_0 - \sqrt{\vec{K}_1 \cdot \vec{K}_2}} \; . \tag{C.6}$$

Recalling that Walsh and Gill [21] considered a perfect electric conductor ($\Delta = 0$), (C.6) reduces to

$$
\begin{aligned}
{}_{SE}\Gamma_P(\vec{K}_1,\vec{K}_2) &= \left\{ \frac{j|\vec{K}_1 \times \vec{K}_2|^2}{2K_T^2\sqrt{\vec{K}_1\cdot\vec{K}_2}} \right\} \frac{k_0}{k_0 - \sqrt{\vec{K}_1\cdot\vec{K}_2}} \\
&= \left\{ -\,{}_{SE}\Gamma''_P(\vec{K}_1,\vec{K}_2) \right\} \frac{k_0}{k_0 - \sqrt{\vec{K}_1\cdot\vec{K}_2}} \ ,
\end{aligned}
\tag{C.7}
$$

where ${}_{SE}\Gamma''_P(\vec{K}_1,\vec{K}_2)$ is the symmetric electromagnetic coupling coefficient as it is was originally derived in the technical report [39] that forms the basis of the work contained in [21]. The negative sign associated with ${}_{SE}\Gamma''_P(\vec{K}_1,\vec{K}_2)$ in (C.7) arises due to a difference in sign convention when defining the electromagnetic coupling coefficient in [39] and subsequent works [9, 44]. For the arguments of the electromagnetic coupling coefficient as it appears in (C.4), the expression in (C.7) may be shown to reduce to

$$
{}_{SE}\Gamma_P(k_0\hat{\rho}_{01} + \vec{K}'', k_0\hat{\rho}_{01} - \vec{K}'') = \frac{|\vec{K}'' \times \hat{\rho}_{01}|^2}{2\left[\sqrt{(K'')^2 - k_0^2}\right]} \frac{k_0}{k_0 - \sqrt{k_0^2 - (K'')^2}} \ , \tag{C.8}
$$

where $K_T = 2k_0$ was used as a result of the long pulse assumption used in going from (2.26) to (2.27). Substituting (C.8) into the monostatic expression for $\mathcal{P}_0(2k_0\hat{\rho}_{01})$ given in (C.4) yields

$$
\begin{aligned}
\mathcal{P}_0(2k_0\hat{\rho}_{01}) =& \Xi_{t0}(2k_0\hat{\rho}_{01}) + \frac{1}{2(2\pi)^2}\int_{\vec{K}''} \Xi_{t0}\left(k_0\hat{\rho}_{01} + \vec{K}''\right) \Xi_{t0}\left(k_0\hat{\rho}_{01} - \vec{K}''\right) \\
&\cdot \ \frac{|\vec{K}'' \times \hat{\rho}_{01}|^2}{\sqrt{(K'')^2 - k_0^2}} \frac{k_0}{k_0 - \sqrt{k_0^2 - (K'')^2}} d\vec{K}'' \ .
\end{aligned}
\tag{C.9}
$$

Comparing (C.9) and (C.2), the expressions are seen to be in agreement with the exception of an extra factor, $\frac{k_0}{k_0 - \sqrt{k_0^2 - (K'')^2}}$, in the integrand of (C.9). From (C.7) and the discussion that immediately followed, this factor arises due to the different analyses that produced the electromagnetic coupling coefficient. Gill's modified stationary phase analysis [9] includes the same additional factor where it is attributed to the fact that radiation from the first scatter may occur in any direction before the second scatter; i.e., with reference to Figure 1.3, as $\rho_{12} \to 0$, the direction of $\vec{\rho}_{12}$ is not unique. This phenomenon was not considered in [39] or [21]; however, Gill [9] notes that the value of this factor does not significantly effect the magnitude of the electromagnetic coupling coefficient when computing second-order cross sections of the ocean surface.

The comparison performed in this appendix may be made exact if the electromagnetic coupling coefficient, as it was original derived in [39] (with an additional factor of -1 to account for the differing sign conventions), is substituted into (C.4). It follows that the monostatic zero-velocity, target-only form of the cross sections derived in this work agree with those previously reported in [39], when the use of a refined electromagnetic coupling coefficient is accounted for.

Appendix D

Summary of Radar Cross Section Formation Process

To visualize the formation of the RCS of an ocean patch containing a deterministic target employed in Chapter 3, a flow chart is presented in Figure D.1.

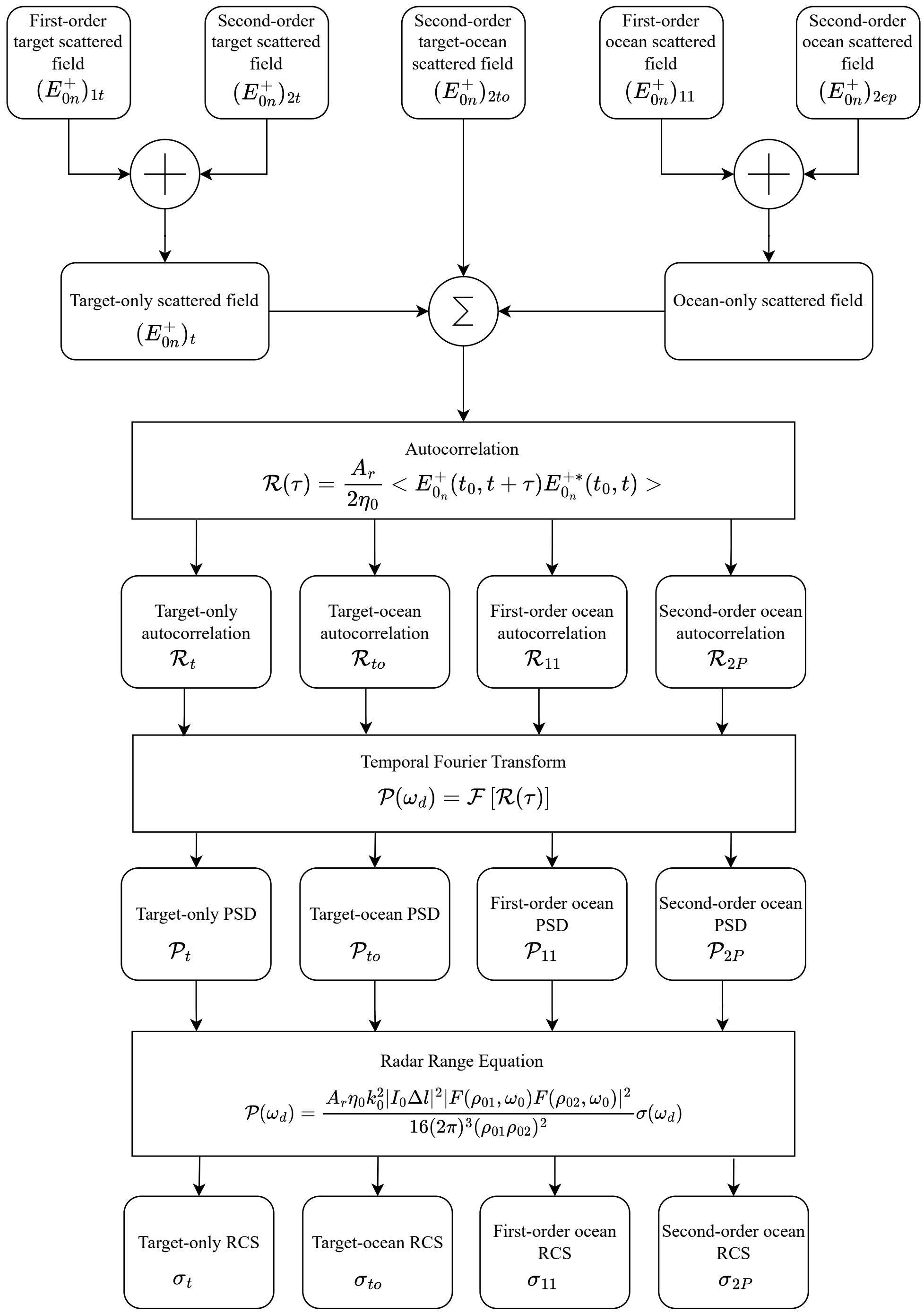

Figure D.1: Flowchart summarizing the RCS formation process employed in Chapter 3.